Graduate School ETD Form 9
(Revised 12/07)

PURDUE UNIVERSITY
GRADUATE SCHOOL
Thesis/Dissertation Acceptance

This is to certify that the thesis/dissertation prepared

By FAN XU

Entitled STUDY OF CATALYST LAYER FOR POLYMER ELECTROLYTE FUEL CELL

For the degree of MASTER OF SCIENCE IN MECHANICAL ENGINERRING

Is approved by the final examining committee:

Chair
JIAN XIE

JIE CHEN

HORIA PETRACHE

To the best of my knowledge and as understood by the student in the *Research Integrity and Copyright Disclaimer (Graduate School Form 20)*, this thesis/dissertation adheres to the provisions of Purdue University's "Policy on Integrity in Research" and the use of copyrighted material.

Approved by Major Professor(s): JIAN XIE

Approved by: JIE CHEN 6/29/2010
Head of the Graduate Program Date

Graduate School Form 20
(Revised 1/10)

PURDUE UNIVERSITY
GRADUATE SCHOOL

Research Integrity and Copyright Disclaimer

Title of Thesis/Dissertation:
STUDY OF CATALYST LAYER FOR POLYMER ELECTROLYTE FUEL CELL

For the degree of MASTER OF SCIENCE IN MECHANICAL ENGINERRING

I certify that in the preparation of this thesis, I have observed the provisions of *Purdue University Teaching, Research, and Outreach Policy on Research Misconduct (VIII.3.1)*, October 1, 2008.*

Further, I certify that this work is free of plagiarism and all materials appearing in this thesis/dissertation have been properly quoted and attributed.

I certify that all copyrighted material incorporated into this thesis/dissertation is in compliance with the United States' copyright law and that I have received written permission from the copyright owners for my use of their work, which is beyond the scope of the law. I agree to indemnify and save harmless Purdue University from any and all claims that may be asserted or that may arise from any copyright violation.

FAN XU
Printed Name and Signature of Candidate

7/2/2010
Date (month/day/year)

*Located at http://www.purdue.edu/policies/pages/teach_res_outreach/viii_3_1.html

STUDY OF CATALYST LAYER FOR POLYMER ELECTROLYTE FUEL CELL

A Thesis
Submitted to the Faculty
of
Purdue University
by
Fan Xu

In Partial Fulfillment of the
Requirements for the Degree
of
Master of Science in Mechanical Engineering

August 2010
Purdue University
Indianapolis, Indiana

ACKNOWLEDGEMENTS

This thesis is dedicated to my family and to Ms. Fei He.

I would like to specifically honor my research advisor, Dr. Jian Xie at IUPUI for giving me the opportunity to work with him and for his unwavering support on this project. This support has extended far beyond issues of mundane technical discussion and has helped me understand the meaning of happiness of research, and the need for gratitude and importance of relationships. I would like to express my gratitude to his sincerity, dignity and dedication towards work.

This work in many ways represents a collaborative effort and would not have been possible to be completed without the assistance of Dr. Horia Petrache, Dr. Bruce. D. Ray, Mr. Matt Justice in the Physics Department, IUPUI, Dr. Derek Ho, Dr. Liu Yun from the National Institute of Standards and Technology (NIST), Dr. Jan Ilavsky from Argonne National Laboratory, Dr. HongFang Sun, Mr. HangYu Zhang from Purdue University, West Lafayette, undergraduate students: Mr. Jose Muniz, Mr. Noma Ogbeifun, Mr. Seth Simonson, Mr. Derek Vleck, and Mr. Daric Fitzwater of IUPUI.

I would like to especially thank Dr. MeiXian Wang for his help and support. I was delighted to have him as my colaborator. I am grateful to him for sharing his knowledge and for his suggestions and hard work during my research.

I would like to individually express my gratitude and deep respect for Pastor John and his wife Ann for helping me during the times I felt defeated. I need to express my

thanks to my best American friend Seth Simonson for helping me a lot in lab building and for introducing me to his family. Seth, your family is awesome!

I would also like to thank the IUPUI Mechanical Engineering Department. Thanks to Dr. Jie Chen and Dr. Horia Petrache for being on my committee and providing many useful suggestions and critiques which were incorporated into the final draft. I would like to thank my research group comprised of Ms. Chan Xiao, Mr. Qi Liu, and Mr. Hao He for their help throughout the project. I hope that we can continue to work together to make more achievement in the future.

Finally, I would like to thank Ms. Fei He for her support and understanding during the last two years. There has been a great deal of love, encouragement and understanding which are deeply appreciated.

TABLE OF CONTENTS

Page

LIST OF TABLES

LIST OF FIGURES

Figure Page

Figure Page

ABSTRACT

Xu, Fan. M.S.M.E., Purdue University, August 2010. Study of Catalyst Layer for Polymer Electrolyte Fuel Cell. Major Professor: Jian Xie.

There are three parts in this work centered on the catalyst layer of Polymer Electrolyte Fuel Cell (PEFC) in this thesis. The first part is for making best MEA structure. One of the major aims of this investigation is to understand the micro-structural organization of ionomer particles and Pt/C aggregates dispersed in a catalyst ink. The dispersion of Nafion® ionomer particles and Pt/C catalyst aggregates in liquid media was studied using ultra small angle x-ray scattering (USAXS) and cryogenic TEM technologies. A systematic approach was taken to study the dispersion of each component (i.e. ionomer particles and Pt/C aggregates) first, then the combination, last the catalyst ink. A multiple curve fitting was used to extract the particle size, size distribution and geometry from scattering data. The results suggests that the particle size, size distribution and geometry of each system are not uniform, rather, vary significantly. The results also indicate that interaction among components (i.e. ionomer particles and Pt/C aggregates) exists. The cryogenic TEM, by which the size and geometry of particles in a liquid can be directly observed, was used to validate the scattering results, which shows the excellent agreement. Based on this study, a methodology of analyzing dispersion of Pt/C particles, Nafion® particles in a catalyst ink has been developed and can serve as a powerful tool for making a desired catalyst ink which is a critical step for making rational designed MEA.

The carbon corrosion process is the second part of the thesis. The carbon corrosion process of low–surface-area Pt/XC72 and high-surface-area Pt/BP2000 was investigated

using an developed accelerated durability testing (ADT) method under simulated fuel cell conditions (a Rotating Disk Electrode (RDE) approach). Compared with the complex MEA system, this innovated approach using RDE can simply focus on carbon corrosion process and avoid the use of MEA in which many degradation/corrosion processes simultaneously occur. It was observed that different carbon corrosion processes resulted in different performance (electrochemical active surface area, mass activity and double layer capacity) decay of catalysts. The corrosion process was studied using TEM. It was found that in the case of Pt/XC72, major corrosion occurred at the center of the Pt/XC72 particle, with some minor corrosion on the surface of the carbon particle removing some amorphous carbon black filaments, while in the case of Pt/BP2000, the corrosion started on the surface. The understanding of carbon corrosion process provides the guidance for making high corrosion resistance catalysts to increase the durability performance of PEFC.

Based on the second work, XC72 carbon blacks were etched using steam under different time and used as a new high corrosion resistance catalysts support for the oxygen reduction reaction. TEM results show that the center part of the XC72 particle was more easily etched away. XRD results show that the 002 and 10 peaks of the XC72 based samples are initially sharp, but then broaden during the corrosion process. TEM results of Pt particles show that the steam etching can improve dispersion uniformity of Pt nanoparticles on the surface of carbon support and reduce the Pt particles size. Electrochemical characterization results show that the mass activity of etched carbon black for 1 hour was 1.3 and 34 times greater than that of the carbon blacks etched for 3h and that of carbon blacks non-ecthed. ECSA of the carbon blacks was also significantly increased after etching. MEA test showed after 45 hours testing, the performance MEA with steam etching 1 hour XC72 based catalyst decreases much less than the MEA with commercial catalyst. Clearly, steam etching is a simple and efficient method to increase the performance and durability of the fuel cells catalysts.

1. BACKGROUND

1.1 Objectives

The three goals of this research are: (1) to develop a novel and systematic approach to study the dispersion of the Pt/C and Nafion® particles in catalyst inks and the geometry and size of Pt/C and Nafion® particles in the dispersion, (2) to investigate the catalyst especially the carbon corrosion process in an simulated PEFC condition using the RDE technique, and (3) based on the corrosion process, to develop a new high corrosion resistance carbon support for PEFC.

1.2 Polymer Electrolyte Fuel Cell (PEFC) Overview

In the past ten years significant emphasis has been placed on the development of cleaner new sources of energy around the world. Hydrogen fuel cell is one of the most promising candidates. Therefore, a lot of investments have been made in the research of hydrogen fuel cells. The capabilities of fuel cell technology have been demonstrated in numerous ways in recent years, yet the challenges of introducing mass produced fuel cells at the consumer level still remain.

A fuel cell is an electrochemical device that is able to continuously and directly convert the chemical energy of externally supplied fuel and oxidant to electrical energy. Fuel cells are customarily classified according to the electrolyte employed. The five most common technologies are polymer electrolyte fuel cells (PEFCs), alkaline fuel cells (AFCs), phosphoric acid fuel cells (PAFCs), molten carbonate fuel cells (MCFCs) and solid oxide fuel cells (SOFCs). However, the advantages of low operating temperatures and compact structure, and high efficiency, make PEFCs rapidly outpacing others.

Unlike most other types of fuel cells, PEFCs use a solid electrolyte, which is based on a polymer backbone with side-chains possessing acid-based groups. The numerous advantages, such as easier sealing, less expensive to manufacture, less problem about corrosion, longer lifetime compared to many of the other electrolytes, of this family of electrolytes make the PEFC particularly attractive for smaller-scale terrestrial applications such as transportation, home-based distributed power, and portable power applications. The distinguishing features of PEFCs include relatively low-temperature (under 90 ^{o}C) operation, high power density, a compact system, high efficiency and ease in handling liquid fuel.

The hope among scientists and engineers is that PEFCs will be a viable technology for power production in commercial applications, residential housing, transportation, and portable electronics; effectively replacing a broad range of power sources spanning from the internal combustion engine to the alkaline battery.

1.2.1 Polymer Electrolyte Fuel Cell (PEFC) Operation

This section will detail the basic electrochemistry which occurs within proton exchange membrane fuel cells, focusing exclusively on the electrodes and the membrane. The fuel cells of interest in this work are referred to as polymer electrolyte (PE) fuel cells because the membrane separating the electrode does just that, it facilitates the transfer of protons from the anode to the cathode due to its acidic nature.

The fuel and oxidant are supplied to the device from external sources. The device can thus be operated until the fuel (or oxidant) supply is exhausted. As can be seen in Figure1.1, at the anode, hydrogen is transported to the catalyst sites where it reacts to yield protons and electrons. Active catalyst sites must be in contact with the reactant gas, an electron conductor (typically carbon black) and a proton conductor (electrolyte) for the reaction to take place. The electrons produced travel into the electron conductor and through an external circuit which terminates at the cathode. The protons produced when the hydrogen molecules are split travel into the proton conductor, through the electrolyte

membrane, and to an active catalyst site in the cathode. The anode reaction can be seen in equation 1.1 below and in Figure 1.1 on the next page.

$$2H_2 \rightarrow 4H^+ + 4e^- \qquad \text{Eq. 1.1}$$

The reactive chemical component at the cathode of a PEFC is oxygen. At the cathode, diatomic oxygen is reduced on the catalyst surface where it combines with the electrons that have departed the anode and traveled the external circuit and with the protons which have departed the anode and traveled through the polymer electrolyte

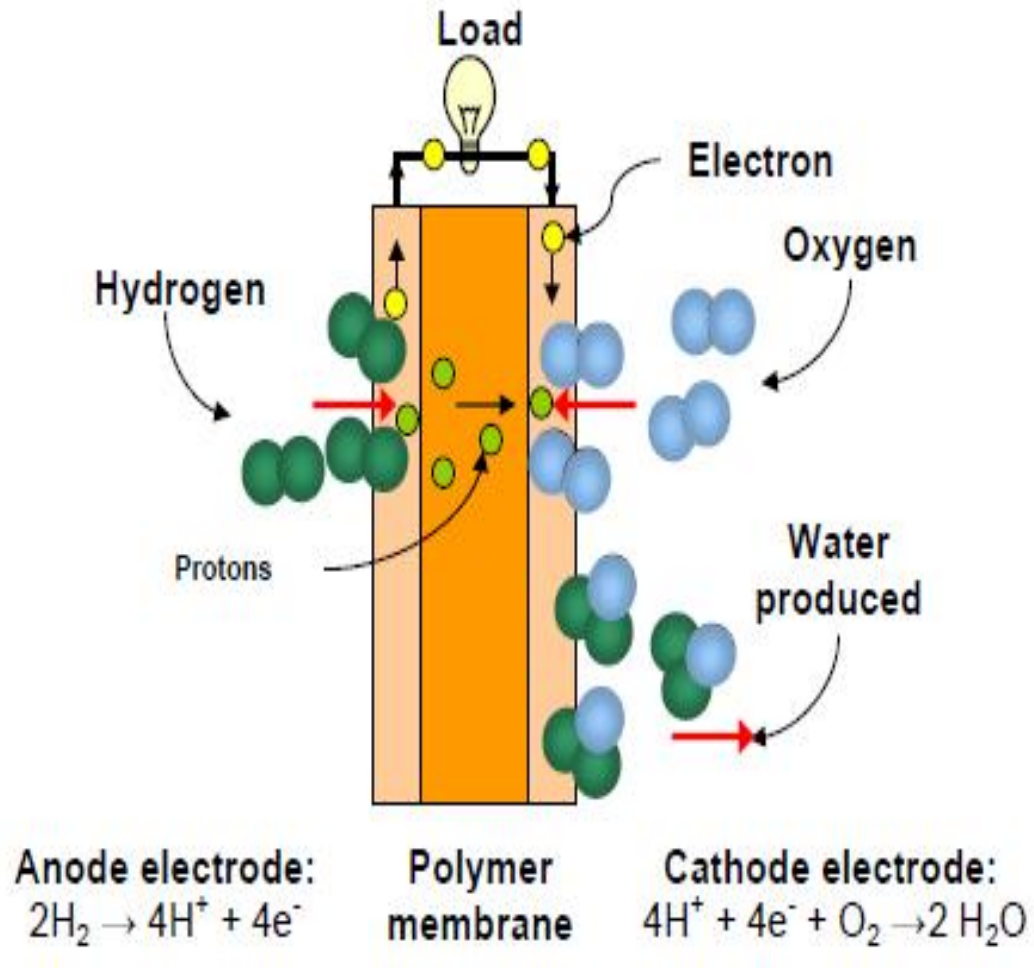

Figure 1.1 Schematic of PEFC electrode reactions.

membrane. Diatomic oxygen molecules are required for this reaction at half the rate at which the diatomic hydrogen molecules are split into protons, and electrons, and the resulting product is water. The cathode reaction is detailed in Equation 1.2.

$$O_2 + 4H^+ + 4e^- \rightarrow 2H_2O \qquad \text{Eq. 1.2}$$

Overall, PEFC yields the following reaction:

$$2H_2 + O_2 \rightarrow 2H_2O \qquad \text{Eq. 1.3}$$

1.2.2 Polymer Electrolyte Membrane (PE) Fuel Cell Components

There are relatively few components that make up a single PEFC. Each of the following components the catalyst layers, the polymer membrane, the gas diffusion layer, and the collector plates, are discussed briefly in this section.

Figure 1.2 illustrates the assembly of a single PEFC. In this work, the membrane with catalyst layers on each side is referred to as the membrane electrode assembly (MEA). It is important to note that in other works, MEA is sometimes used to mean the entirety of the membrane, catalyst layers, and gas diffusion layers. The MEAs have similar sandwich-like structures.

As depicted in Figure 1.2, the outer layers of the sandwich are GDLs. The membrane is in the middle, with catalysts between the GDL and membrane. The anode, the negative side of the fuel cell, conducts the electrons freed from the hydrogen oxidation so that they can be used in an external circuit. The cathode, the positive side of the fuel cell, conducts the electrons back from the external circuit to the catalyst, where they can recombine with the hydrogen ions and oxygen to form water. The PEM, a specially treated material, conducts only positively charged ions and blocks electrons.

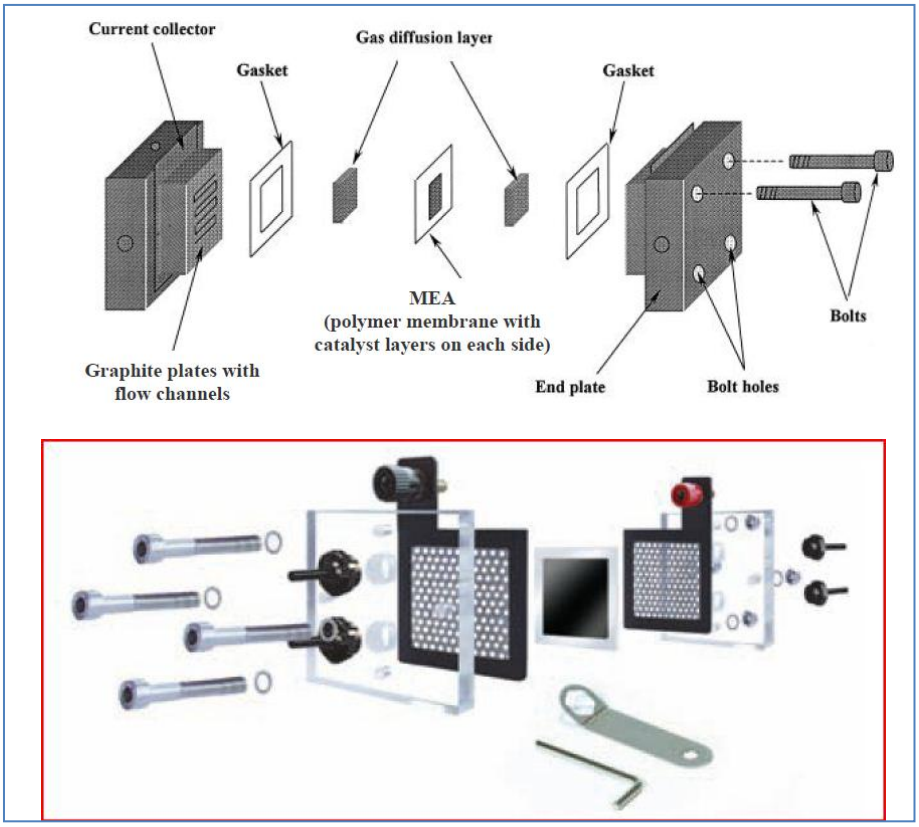

Figure 1.2 Single PEFC components and assembly

The proton exchange membrane. The main function of the membrane in PEFCs is to transport protons from the anode to the cathode; membrane polymers have sulfonic groups, which facilitate the transport of protons. The other functions include keeping the fuel and oxidant separated, which prevents mixing of the two gases and withstanding harsh conditions, including active catalysts, high temperatures or temperature fluctuations, strong oxidants, and reactive radicals. The membrane could just be detected by hydrogen crossover method. And the crossing current could tell whether the membrane is damaged or no.

The performance and cost of PEFCs are limited mainly by the MEA. The MEA structure, which consists of two porous catalyst layers bonded onto the Nafion® membrane electrolyte, is schematically shown in Figure 1.3[1].

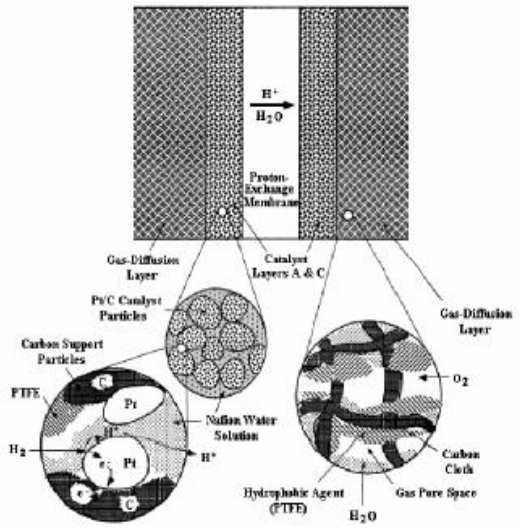

Figure 1.3 Diagram of a typical MEA structure

The composite catalyst layer is consisting of recast Nafion® ionomer (shown as threads) and the precious Pt metal catalyst nano particle (shown as black dots) sitting on the surface of carbon aggregates (shown as sphere). The Nafion® ionomer functions as a binder as well as the necessary proton transport pathways. Platinum has been considered to be the best catalyst for both the anode hydrogen oxidation and the cathode oxygen reduction. Usually, the platinum catalyst is formed into small particles (dia. ~ 7 nm) on a surface of somewhat larger particles that act as a supporter, known as carbon powder (dia. ~ 70 nm). A widely used carbon-based powder is Vulcan XC72® (by Cobalt). This way the platinum is highly divided and spread out, so that a very high portion of the surface area will be in contact with the reactant, resulting in a great reduction of the catalyst loading with an increase in power. In the early days of PEFC development, the catalyst was used at the loading of 28 mg/cm^2 of platinum. In recent years the usage has been reduced to around 0.2 mg/cm^2 with an increase in power.

The gas diffusion layer (GDL) in a PEFC serves a variety of purposes. This layer must be porous to allow the hydrogen or oxygen to diffuse to the catalyst layers.

Additionally, the GDL must be well suited to transport the water produced at the cathode reactions sites outward from the reaction sites to avoid what is called electrode flooding. Flooding simply refers to the fact that if too much water is surrounding the catalyst site, then it is more difficult for gases to diffuse to the catalyst site due to the presence of the water. The GDL must also be electrically conductive since the electrons produced at the anode must travel through the GDL to the external circuit and around to the cathode to complete the reaction. Resistance to corrosion is also an issue of concern since the GDL resides in a moist and acidic environment. Due to the requirements of permeability, electrical conductivity, and corrosion resistance, the GDL is typically constructed of flexible carbon fiber based woven fabric, or stiff carbon fiber based paper.

The final components required for a single PEFC are the collector plates. The collector plates are typically pressed against the gas diffusion layer to collect electrons from the anode GDL and transport them into the external circuit or to conduct electrons from the external circuit into the cathode GDL to complete the circuit. Additionally, the collector plates typically have a flow field machined into them to evenly distribute the reactant gas uniformly over the surface of the GDL.

1.3 Organization

This thesis is organized into four chapters prepared to promote a logical flow of information. The first chapter is an introduction to the thesis providing the motivation behind the research, an overview of the accomplishments, background information and objectives of this research.

Chapter 2 provides experimental information. An explanation of the steps of experiment is provided. From Chapter 3 to 5, all the results of the research containing study of catalyst ink by scattering experiment, corrosion process investigation and development of high corrosion resistance catalyst for PEFC are presented and discussed. In addition, some values are graphed to show correlation. Lastly, Chapter 6 offers conclusions and suggestions for further study.

2. STUDY OF CATALYST INK DISPERSION USING ULTRA SMALL ANGLE X-RAY AND CRYOGENIC TEM

2.1 Introduction

2.1.1 MEA Fabrication

Currently, PEFCs are still not affordable because of the high cost and performance [1].The membrane electrode assembly (MEA) is the key core part of PEFCs, which limit the performance and cost of PEMFC, and hence, to make fuel cell technology commercially successful, the most important thing is to develop a high-performance, low-cost, and durable MEA, researches attempts to investigate the approaches haves been focused on catalysts, membranes novel high-performance materials and improving the engineering aspects of cell design [2 - 5].

A typical MEA is a composite in which a polymer electrolyte membrane is sandwiched by two porous catalyst layers as schematically showing in Figure 1.1. The catalyst layer consists of a network of recast Nafion® ionomer that holds carbon aggregates together. The precious metal catalyst nanoparticles are attached on the surface of carbon aggregates. In order to achieve the maximum performance, the catalyst layer of carbon aggregates. In order to achieve the maximum performance, the catalyst layer needs to have (i) the maximum interface of Nafion®/catalyst for anode and cathode gas reactions, (ii) appropriate pore structure to allow gas diffusion and water dissipation, and (iii) the optimized Nafion® networks which could bind carbon aggregates together to have structural integrity of catalyst layer and to provide a proton conduction path, which could increase the proton conductivity of catalyst layer. Numerous new techniques for the fabrication of catalyst layer/MEA have been

explored, such as doctor-blade spreading, electro-phoretic deposition (EPD), sputtering, electro-spraying, and rolling [6 - 9].

The MEAs were fabricated at Los Alamos National Laboratory (LANL) using the "thin decal" process [10 - 11]. As shown in Figure 2.1 [12], in this process, catalyst inks (a Pt/C catalyst powder is dispersed in solvents (i.e. water or organic solvents, e.g. glycerol) along with the ionomer suspension (generally, a 5 wt.% Nafion® solution) to form a uniform suspension) painted onto Teflon-coated fiberglass substrates (the decal) and heat-treated, followed by hot pressing (The decals were then hot-pressed onto both sides of a Nafion® N212 membrane for 5 minutes at 205 ℃) to form an MEA, Finally, the decals were peeled off, leaving the MEA, which was boiled for 2 hours in H_2SO_4 to convert the Nafion® to its proton-conducting form.

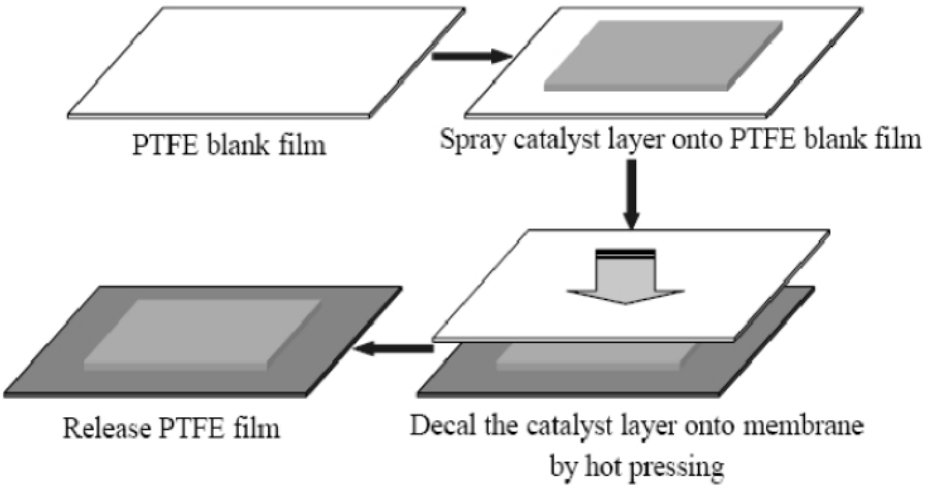

Figure 2.1 Process flow diagram of thin film decal transfer technology

The dispersion of the Pt/C aggregates and the ionomer inside a solvent is the first step for making a good structure of the catalyst layer. There are three kinds of catalyst inks, hydrophobic ink, hydrophilic solution and colloid ink, and Pt ion solution ink and Pt foil [13]. Hydrophilic solution and colloid ink are employed in "thin decal" method. In order to have an appropriate ink system, the Pt/C catalyst powder must be well

dispersed, and it must form small-sized aggregates (on 100 nm scale) while the ionomer must form small diameter strips or rods so they can bind the Pt/C aggregates. All the nano-scaled catalyst particles should come into contact with the other components uniformly to form a porous and rigid solid catalyst layer/MEA, which will permit a good performance. Therefore, to verify whether a formulated catalyst ink disperses the Pt/C aggregates and the ionomer particles well is of importance. The current approach is to use inks with different making protocols to make MEAs, and then to measure the MEA fuel cell performance to verify the ink "formulation". Mitsuharu et al. [14] investigated the effect of solvents, ethylene glycol and propylene glycol, in catalyst ink on catalyst layer structures, by measuring a laser displacement sensor (LDS), in polymer electrolyte membrane fuel cells (PEMFCs) and resulting cell performances. The LDS showed that the thicknesses of catalyst layers fabricated from catalyst ink containing propylene glycol were 1.4 times larger than those fabricated from a catalyst ink containing ethylene glycol due to their high porosity. Catalyst layers fabricated from catalyst ink containing ethylene glycol showed higher cell voltage than those fabricated from catalyst ink containing propylene glycol due to their lower ohmic losses. These results suggested that the solvent in catalyst ink play an important role in forming pore structures of catalyst layers. However, how the solvent affects the interaction of the carbon and Nafion® ionomer to change the geometry and dimension the "ink particles" to change the structure of catalyst layer and performance could never known in this approach.

Therefore, developing an effective way to determine the detailed organization structures (particle size and geometry) of the catalyst/carbon aggregates and the Nafion® ionomer in catalyst inks to verify the "optimized" ink formulation could provide the guidance for rational design of a high-performance catalyst layer/MEA.

2.1.2 Catalyst Ink Dispersion Investigation Review

Some researches [15 - 21] have been conducted to investigate the micro-structure of Nafion® solutions by Dynamic light scattering (DLS) [15 - 16],

Small angle neutron scattering (SANS), small angle X-ray scattering (SAXS) (with Nafion® concentration ranging from 5 to 20 wt%) and electron spin resonance (ESR) (with Nafion® concentration ranging from 1 to 22 wt%) experiments. Two different sizes of Nafion® aggregates were found in both solutions (10 mg/ml Nafion®/ethanol/water and 5.3 mg/ml Nafion®/ water) by DLS, the aggregates were attributed to the electrostatic attraction through the side chain sulfuric ion pairs and the hydrophobic interaction of fluorocarbon backbone. Most literatures [17 - 18] use compact cylinder model to fit the SAXS and SANS results, it was found that the solvent polymer contact is at the surface of the micelle, rather than the open coil model, in which the solvent-polymer contact is maintained all along the chain. G. Gebel [21 - 22] et al. indicated from the SAXS results that the size of Nafion® ionomer is d = 2.5 nm, L = 17 nm. Two aggregation processes were observed in Su-Jen Lee [21] et al.'s experiment by membrane osmometer, viscoelasticity analyzer, and dynamic light scattering. The author attributed the primary aggregation process, which forms smaller sizes (10^3 nm) rod-like aggregation particles, to the hydrophobic interaction of fluorocarbon backbone. The ionic aggregation of primary aggregation particles, which arise from the electrostatic attraction of Nafion® side chain $–SO_3^-$ ion pairs, would causes the secondary aggregation process, which forms larger aggregation particles (10^4 nm).

However, there is no literature so far reporting the detailed organization structures (particle size and geometry) of catalyst ink. The large challenges in catalyst ink research arise from the strong absorption of visible and UV light by the ink. It was indicated by the previous experiments that the dynamic light scattering technology only response to the very much diluted ink, which could lead to a deviation from the original dispersion. My goal is to develop an effective and easy method to determine the organization structure of each component in a catalyst ink. Neutron and x-ray scattering (ultra small angle Neutron/ X-Ray Scattering technologies) could overcome this problem to determine the size and geometry of Nafion® ionomer particles and Pt/C aggregates in liquid media because they have a high energy incident beam, so the

absorption of the beam by the Pt/C aggregates in a catalyst ink can be effectively reduced. Therefore the ink system would be successfully studied.

2.2 Experimental Section

2.2.1 Ultra-Small Angle X-Ray Scattering Principle and Theory

The working principle of scattering techniques is schematically shown in Figure 2.2. The incident beam comes out from the monochromator, and when it hits the sample, the scattered beam will be collected by the detector. There is relationship between the scattered beam pattern and the size and geometry of the particles such that the size and geometry of the particles can be determined by the scattered pattern. The astray incident beam can also reach the detector, which provides false information on the particles. Therefore, the incident beam needs to be perfectly collimated to eliminate interference. This can be achieved by having the incident beam go through two perfectly aligned pinholes. Depending on the incident beam, scattering techniques can be neutron scattering, x-ray scattering, and light scattering.

Ultra-Small Angle X-ray Scattering (USAXS) is a small-angle scattering (SAS) technique where the elastic scattering of X-rays (wavelength 0.1 - 0.2 nm) by a sample which has inhomogeneities in the nm-range, is recorded at very low angles (typically 0.1 - 10°). This angular range contains information about the shape and size of macromolecules, characteristic distances of partially ordered materials, pore sizes, and other data. SAXS is capable of delivering structural information of macromolecules between 5 and 25 nm, and of repeat distances in partially ordered systems of up to 150 nm. USAXS (ultra-small angle X-ray scattering) can resolve even larger dimensions, about 6200 nm. USAXS is used for the determination of the microscale or nanoscale structure of particle systems in terms of such parameters as averaged particle sizes, shapes, distribution, and surface-to-volume ratio. The USAXS in ANL, showed in Figure 2.2, has angular and energy resolutions of the order of 10^{-4}, accurate and

repeatable X-ray energy tenability over its operational energy range from 8 to 18 keV, and a dynamic intensity range of 108 to 109, depending on the configuration. It further offers quantitative primary calibration of X-ray scattering cross sections, a scattering vector range from 0.0001 to 1 $Å^{-1}$, and stability and reliability over extended running periods.

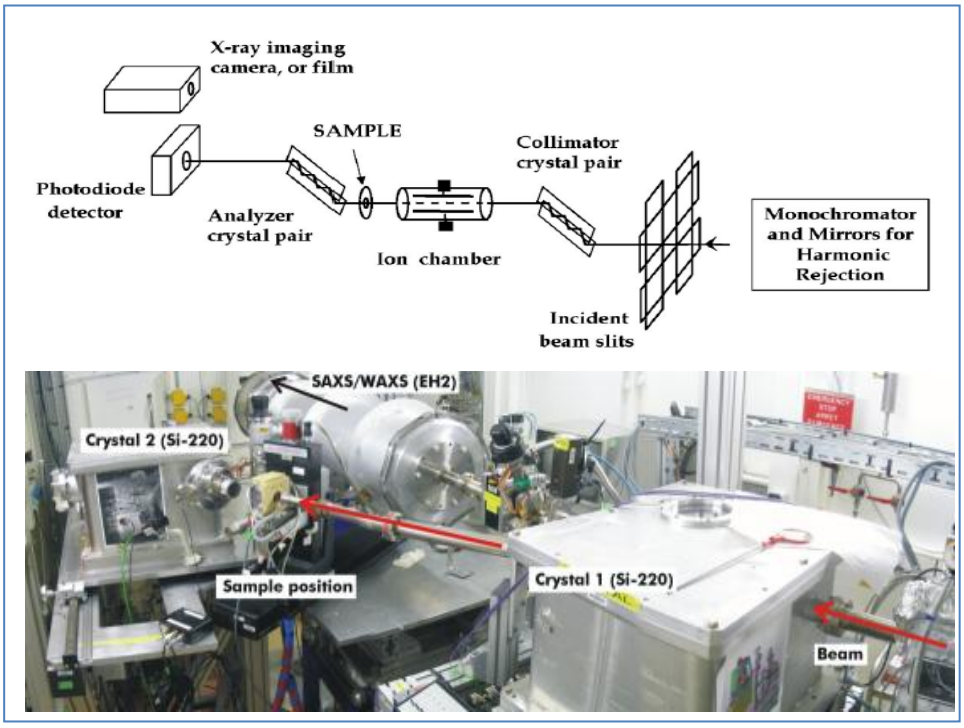

Figure 2.2 Schematic of working principle of Ultra Small Angle X-Ray Scattering (USAXS)

At very small angles, the shape of the scattering in the so-called Guinier region can be used to give us an idea of the radius of gyration of any distinct structures that are on this type of length scale. As for the fitting, the slope could be obtained as shown in Figure 2.2. Following Guinier's law for small q values, the observed intensity can be approximated as:

$$I(q) = I_0 \exp(-q^2 R^2/3) \qquad \text{Eq. 2.1}$$

As for small θ, $q = 4\pi\theta/\lambda$, 2θ is the angle between the incident X-ray beam and the detector measuring the scattered intensity, and λ is the wavelength of the X-rays. R is the radius of gyration for the scattering process, which depends on the geometrical shape.

If the particles are spherical objects, then the parameters follow Eq. 2.2 and 2.3:

$$\ln(I) = \ln(I_0) - q^2R^2/3 \qquad \text{Eq. 2.2}$$

$$r^2 = 5/3\ R^2 \qquad \text{Eq. 2.3}$$

If the particles are flat or needles objects, they will follow Eq. 2.4 and 2.5:

$$\ln(q^2I) = \ln(I_0) - q^2R^2/3 \qquad \text{Eq. 2.4}$$

$$\ln(qI) = \ln(I_0) - q^2R^2/3 \qquad \text{Eq. 2.5}$$

Preliminary work has been carried out for Nafion®/Pt/Carbon dispersion using light scattering for determining the size and geometry of particles in catalyst inks. The results show that the Nafion® ionomer particle size is in the range of 20 - 230 nm, and the Pt/C aggregates are in the range of 390 - 4600 nm. However, due to the strong absorption of Pt/C in the visible light region, the results given by light scattering for the Nafion® and Pt/C dispersion are subject to questioning, especially when the loadings of the Pt/C are high. In addition, the use of light scattering requires the sample dilution which could lead a deviation from the original dispersion.

$$I(q) = Bq^{-4}\text{, where } B = 2\pi N(\Delta\rho)2S \qquad \text{Eq. 2.6,}$$

The scattering data are well described by the global unified fit analysis. Local Porod and Guinier scattering regimes are identified from the analysis as will be described. Large scattering angles and thus high values of the momentum transfer

vector, q, reflect small size, d, through bragg's law, $d = 2\pi /q$, at a high q, the scattered intensity, *I*(q), decays following a power law (porod's law). Here S is the average surface area of a particle and N is the number density of primary particles in the measured scattering volume, respectively, while $\Delta\rho$ is the difference in electrom density between the particles and the background of the solvent.

A power law is observed, and this first power law (Porod) regime is followed at lower q by a knee like decay (Guinier) regime, this knee like decay in intensity reflects the structural size of primary particles. This scattering for these knees like regimes follows Guinier's law,

$$I(q) = G_i \exp\{-q^2 R_{gi}^{2/3}\}w, \text{ where } G_i = N_i(\Delta\rho)2V_i^2 \qquad \text{Eq. 2.7}$$

where N_i is the number density and V_i is the volume of a primary particle in the first (i = 1) Guinier regime. And the number density and volume of an agglomerate in the second (i = 2) Guinier regime, furthermore, from Eq. 2.8 the radius of gyration of the primary articles, R_{g1} and the radius of gyration of the agglomerates R_{g2} can be derived.

The slope of the power law decay between the two Guinier knees is directly related to the mass fractal structure of the ramified agglomerates by:

$$I(q) = B^2 q - Dt \qquad \text{Eq. 2.8}$$

where D_f is the mass fractal dimension and B_2 is a power law pre-factor,

$$B_2 = (G_2 Df/R_{g2}^{Dr})\, \Gamma Df/2 \qquad \text{Eq. 2.9}$$

where G_2 is a constant defined by Eq 2.7 and Γ is the gamma function.

$$dV/S = 6Q/\pi B_1 \qquad \text{Eq. 2.10}$$

where the Porod invariant, Q, is the integral. Several choices to describe the primary particle diameter are possible such as dsphere from R_{g1} as described above, or using various integrals of the scattering intensity versus q, leading to the cord length.

In the present work, the primary particle diameter is derived from Eq. 2.11 which is presented below:

$$Q = \int_0^\infty q^2 I(q)\, dq = 2\pi^2 N(\Delta\rho)^2 V \qquad \text{Eq. 2.11}$$

2.2.2 Ultra-Small Angle X-Ray Scattering Sample Preparation

Catalyst inks were prepared by mixing the carbon-supported catalyst (20% Pt/C, ETEK) with 5% Nafion® solution (Ion Power Inc., New Castle, Delaware), 1.0 M tetrabutylammonium hydroxide (TBAOH) (Fisher Scientific, NJ) and glycerol (Fisher Scientific, NJ). The sample information was listed in Table 2.1.

Table 2.1 Sample preparation for USAXS

sample	Nafion® (g)	Glycerol/d8-G* (g)	TBAOH (g)	Pt/C(g)
Nafion®	1	0	0	0
Nafion®+G*	1	1	0	0
Nafion®+G*+T**	1.034	1.034	0.052	0
28% G*+Pt/C	0	2.74	0	0.35
28% Nafion®+T**+Pt/C	2.185	0	0.11	0.28
28% Nafion® ink***	1.034	1.034	0.052	0.13

* G: glycerol;
**T: tetrabutylammonium hydroxide (TBAOH);
***ink: Pt/C aggregates+Nafion®+TBAOH+glycerol;

Ultra Small-Angle X-ray scattering (USAXS) measurements were conducted by the versatile ultra-small-angle X-ray scattering (USAXS) instrument at the Advanced Photon Source (APS) at Argonne National Laboratory. The USAXS has angular and energy resolutions of the order of 10^{-4}, accurate and repeatable X-ray energy tunability over its operational energy range from 8 to 18 keV, a dynamic intensity range of 108 to 109, and a scattering vector range from 0.0001 to 1 $Å^{-1}$. The samples were filled into a capillary (Φ = 2.5 μm) using a 1 μL micro-pipette (Figure 2.3) and attached to a porous stain steel piece as shown in Figure 2.3.

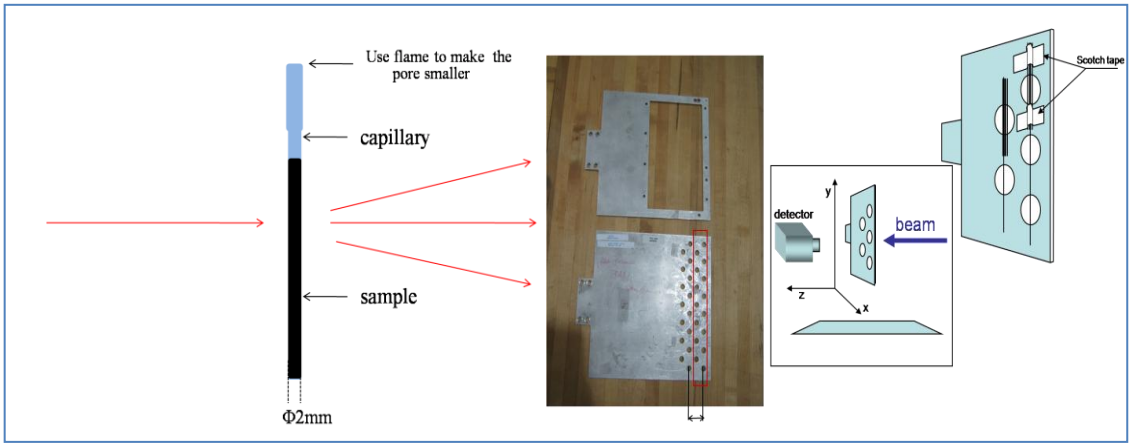

Figure 2.3 Sample container for USAXS

2.2.3 Cryogenic Temperature Transmission Electron Microscopy Sample Preparation

Considering that light microscopes have limited image resolution that is imposed by the wavelength of visible light, transmission electron microscopy (TEM) is the only technique that provides nanometer-scale resolution real-space images of three-dimensional objects. The application of TEM to direct visualization of colloidal fluid nanostructures requires rapid vitrification of the samples, and so the technique is referred to as cryogenic TEM or Cryo-TEM. Cryo-TEM is now accepted as the most useful tool for direct imaging self-aggregation in liquid systems, which can visualize objects as small as 1 nm. A wide range of systems of low- and high-molecular weight solutes, synthetic and biological, has been studied by the technique. Most of the

Cryo-TEM work reported to date has involved water-rich, especially water-continuous systems. A few exceptions include work on some micro-emulsions and on silicone resin-in-oil solutions. It is seldom used in material science.

All the samples studied by USAXS were studied by Cryo-TEM (FEI/Philips CM-10 bio-twin, Purdue, West Lafayette) except for Nafion®+Glycerol and Nafion®+Glycerol+TBAOH. About 3.5 μL of sample was placed on to copper grid (400 mesh, SPR) coated with holey carbon film. The excess sample was blotted off with filter paper. Then the grid was immediately plunged into liquid ethane cooled by liquid N_2. The holders are shown in Figure 2.4. The sample grid was loaded into the microscope with a Gatan side-entry cryoholder. Low dose images were collected using CM200 or CM300 cryomicroscope with a field emission gun operating at 200 kV or 300 kV respectively. The sample grid was loaded into the microscope with a Gatan side-entry cryoholder. Low dose images were collected using CM200 or CM300 cryomicroscope with a field emission gun operating at 200 kV or 300 kV respectively.

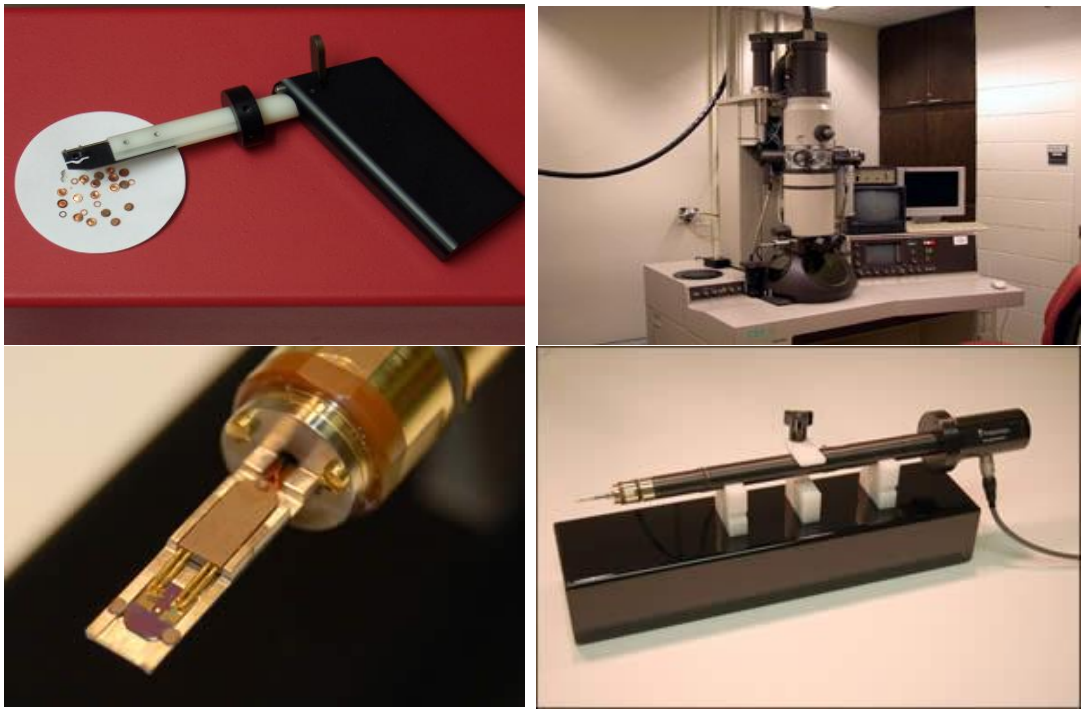

Figure 2.4 Cryo-TEM ultra-rapid sample freezing system

2.3 Results and Discussion

2.3.1 USAXS Data Fitting by Igor Pro

The USAXS data were analyzed by Igor Pro, which developed by Dr. Jan Ilavsky in Argonne National lab. Because the ink system is complex and unknown, global unified function was employed to fit the data. Figure 2.5 shows the general steps of fitting.

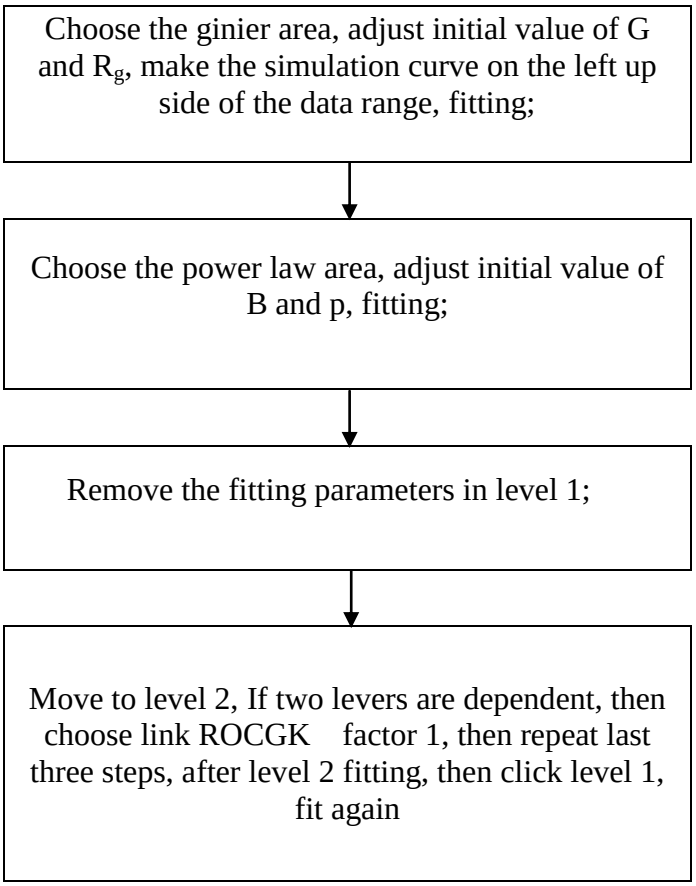

Figure 2.5 Steps to apply the unified global fitting

2.3.2 Particle Geometry and Size in Catalyst Ink by USAXS and Cryo-TEM

The size and micro-geometry of all samples were derived from the USAXS data. To further validate the USAXS data, all samples were analyzed using cryogenic TEM. A liquid sample is fast freezing to lock the original structure of particles in liquid media.

This frozen sample then is analyzed using Cryo-TEM. The combination of USAXS and Cryo-TEM measurements reveals the relationship between the aggregate structures.

The typical scattering data obtained from USAXS measurements of 5% Nafion® solution is shown in Figure 2.6. There is a decrease of intensity at low q and a peak at media q, which is ascribed to the long-range crystalline domains of a lamellar structure of ionomer in the matrix. The signal of high q region was too weak for reliable data evaluation and was not considered in the following evaluation. Scattering data (black circles) were fit using the global unified function (red solid line). A power-law of -2 (slope) (green dashed line, Porod fit, Figure 2.6) is observed for the primary particles, which reflects soft agglomerated primary particles consistent with the TEM insert. This power-law (Porod) regime is followed at lower q (~0.07 $Å^{-1}$) by a knee-like decay (Guinier) regime (dotted line, Guinier fit). This knee-like decay in intensity reflects the structural size of primary particles. As for Figure 3.6, the fitting result yields that R_g = ~3 nm, ETA (average inter-particle distance) is around 141 Å, which is bit large for 30 Å particles, so it would be assumed that these particles are repulsive to each other. The fitting results agree with the TEM insert.

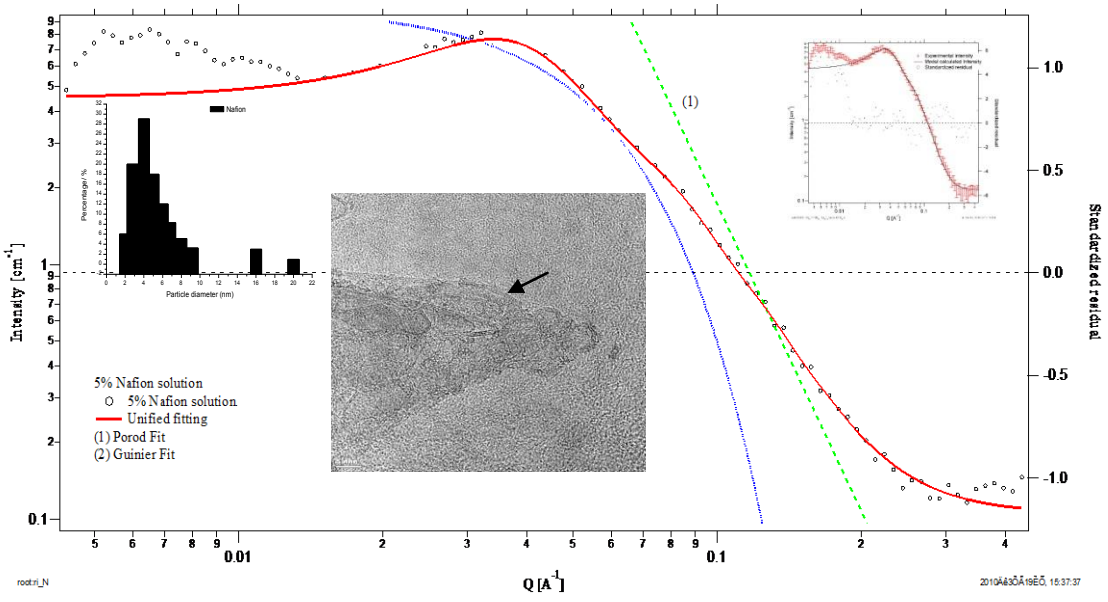

Figure 2.6 An USAXS and Cryo-TEM image of 5% Nafion® Solution (Power Ion)

A TEM image of 0.1%Nafion® solution (the 5% Nafion® solution was diluted by isopropyl and water (4 : 1) to 0.1%) was inserted in Figure 2.6, the TEM image shows that the Nafion® ionomer in isopropyl is rod-like (as arrow pointed) with the 20 ~ 30 nm in length and 2 ~ 3 nm in diameter, which is very close to the value reported by Gebel et al. [20] for Nafion® ionomer in diluted solution (cylinder, d = 2.5 nm, L = 17 nm). Based on the geometry information from TEM image, another fitting employing unified rod model was carried out, resulting in d = 2.4 $\pm$ 0.2 nm, L = 21.4 $\pm$ 1.4 nm long rod. This fitting curve was also inserted in Figure 2.6.

The USAXS patterns of three different samples, Nafion® ionmmer, Nafion® ionomer+Glycerol and Nafion® ionomer+TBAOH+Glycerol, are presented in Figure 2.7. Since glycerol only serves as solvent and does not change the chemical structure of Nafion® ionomer, therefore, the local scattering regimes of Nafion® ionomer and Nafion® ionomer+Glycerol almost overlapped in the region of q = 0.1 - 1 $Å^{-1}$. The fitting by unified rod model showed that the porod slopes are -2.06 and -1.4, d = 2.4 $\pm$ 0.2 and 2.8 $\pm$ 0.2, L = 21.4 $\pm$ 1.4 and 14 $\pm$ 1.4 nm for Nafion® ionomer and Nafion® ionomer+Glycerol respectively. When TBAOH was added into the system of Nafion® ionomer+Glycerol, the high q part (first power-law slope was -2) of the scattering curve is almost the same as those of systems of Nafion® ionmer and Nafion® ionmer+Glycerol. However, remarkable differences appeared in the medial and lower q regions that the peak in the media q (from 0.01 to 0.1 $Å^{-1}$) disappeared. In low q part (from 0.0001 to 0.01 $Å^{-1}$), the second Porod regime with a slope -2.6 followed a second Guinier regime showed up, which suggested bigger particle in the system. This may be caused by TBA^+ (whose radium is much larger than H^+) replacing H^+ of the Nafion® ionomer, which makes the particle size of Nafion® ionomer became bigger. The fitting results obtained by global unified function are showed in Table 2.2 that there are particles with diameter at 33.3 ~ 48.7 nm.

The Pt/C system was also investigated by USAXS and Cryo-TEM to get the information of geometry and particle size of catalyst powder in dispersion. The catalyst system is more complex than the Nafion® ionomer system in terms of size and geometry.

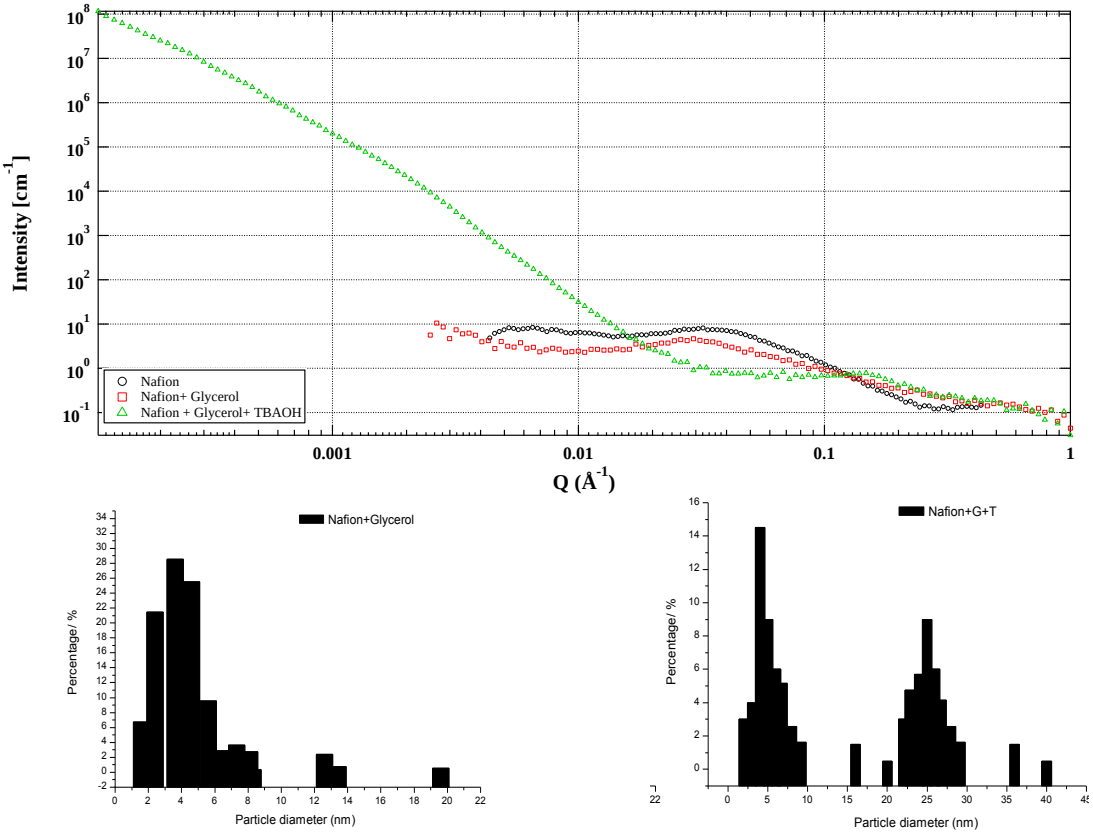

Figure 2.7 Comparison of Nafion® ionomer in different solvents. USAXS plots of 5% Nafion® solution (triangles), Nafion®+Glycerol (squares) and Nafion®+Glycerol+TBAOH (circles)

Four levels have been employed in the global unified function fitting for scattering data of Pt/C system due to the variation of the slopes in the whole region. The corresponding geometries of particles from the Cryo-TEM images are inserted in the different levels. As could be seen from Figure 2.8 (Pt/C+Nafion®), in high q regime, from 1 to 0.1 Å^{-1}, was assigned to be the first level, which started with the first porod fit followed with the first Guinier fit. The fitting results showed power-law slope $P_1 = 1.5$, $R_{g1} = 1.95 \pm 0.2$ nm, which is consistent with the Nafion® ionomer size shown in the

TEM inserted. The second level fitting was carried out from 0.01 to 0.1 $Å^{-1}$, resulting in R_{g2} = 33 ± 1.4 nm, power-law slope P_2 = 2.7. A corresponding diameter $d_{sphere} = 2(5/3)^{0.5}R_{g2}$ = 85 nm can be calculated assuming monodisperse spherical particles. According to TEM image, the radium/diameter of single carbon particle, which has a sphere-like geometry, was close to 35/70 ± 2.5/5 nm, which is very close to USAXS second level fitting results. In medial q part, from 0.001 to 0.01 $Å^{-1}$, the third level could result in the particle size about R_{g3} = 102.7 ± 5 nm, power-law slope P_3 = 3.4 which indicated aggregated particles in the system. The aggregated particle could be observed in Cryo-TEM image inserted in Figure 2.8 that three to four sphere carbons aggregated to form a big rod-like particle, whose radium is about 30 ± 2 nm and length is about 150 ± 10 nm. It would be obtained from the fourth level (from 0.0001 to 0.001A) that R_{g4} = 292.3 ± 5 nm and power-law slope P_4 = 4. The corresponding Cryo-TEM image could be seen in level 4 of Figure 2.8, an "L" like agglomerated particle with a length around 200 nm was found in the system. Therefore, Pt/C with Nafion® solution was a complex multi-particle system with different particle sizes and geometry, the primary particle size distribution was obtained from the USAXS by Igor software after normalization.

Nafion® ionomer particle growth depends on TBAOH as showed before. The Pt/Carbon black+Nafion®+TBAOH system was also investigated. The USAXS result was showed in Figure 2.9. With the same data process, the fitting results showed that R_{g1} = 1.8 ± 0.2 nm with a power-law slope P_1 = 1.21 in the first fitting level. According to previous sample, it could be concluded that this fitting level could be contributed by Nafion® sample, also this fitting level could be mainly attributed to Nafion® ionomer and Pt, because the particle size of Pt is about 3 ~ 4 nm, which is close to the fitting value we obtained in this level. The second fitting level gave R_{g2} = 32 ± 2 nm with the power-law slope P_2 = 2.74. Based on $R_{g2,}$ a corresponding diameter $d_{sphere} = 2(5/3)^{0.5}R_{g2}$ = 82.9 nm can be calculated assuming mono-disperse spherical particles, which could be confirmed by the Cryo-TEM inserted in the high Q part of Figure 2.9.

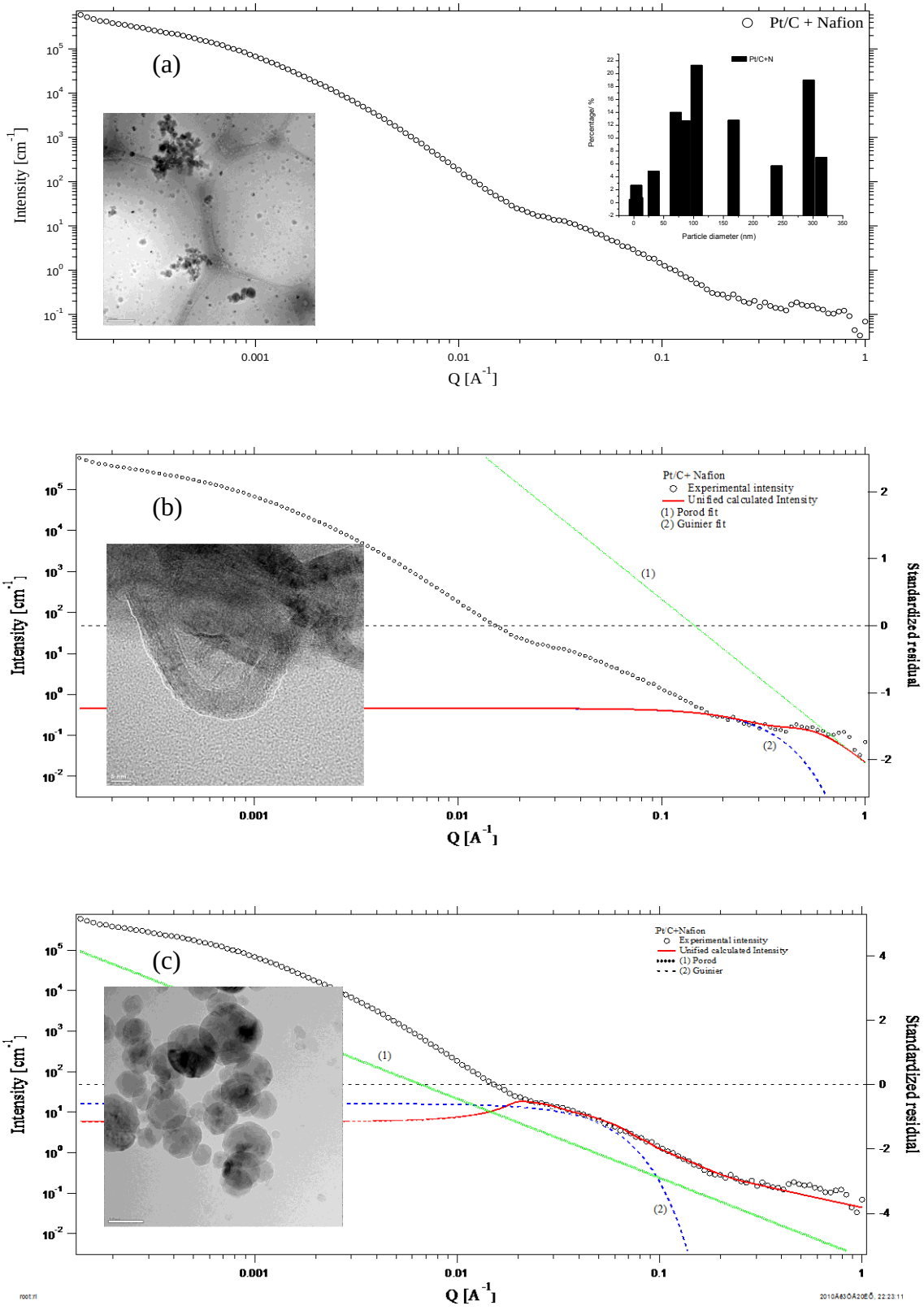

Figure 2.8 (a) – (e) USAXS plots and Cryo-TEM images of 28% Pt/C+Nafion® solution

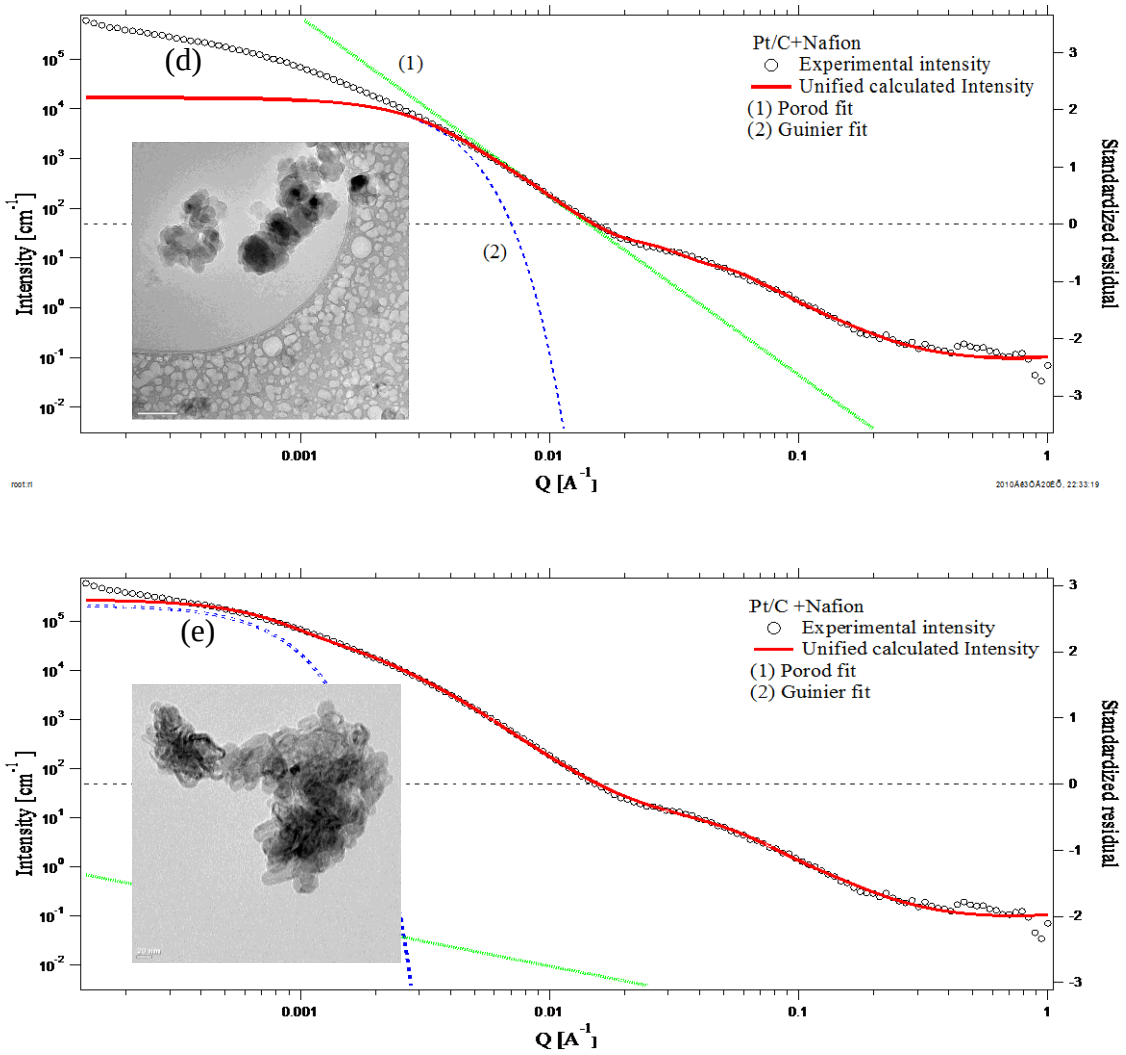

Figure 2.8 Continued

There is sphere-like single carbon black with a diameter about 80 nm. From 0.001 to 0.01 Å^{-1}, another fitting level was applied, R_{g3} = 201.7 ± 5 nm and power-law slope P_3 = 2.63 could be obtained by the third fitting level, an aggregated rob like particle with a length around 100 to 250 nm was found in Cryo-TEM image in Figure 3.9. The fourth fitting level was employed to fit the low Q part, the fitting results showed R_{g4} > 300nm, power-law slope P_4 = 2.77. In Cryo-TEM image, a bigger size agglomerated particle formed in this sample, which is a 420nm island-like particle. The particle size distribution was shown in Figure 2.9. Compared with Pt/C+Nafion® system, the primary particle size

is about 100 nm, which is also mono sphere carbon particles. Based on the size distribution data, the mean particle size could be obtained as 158 ± 5 nm. The increased particle size might be caused by the TBAOH effect.

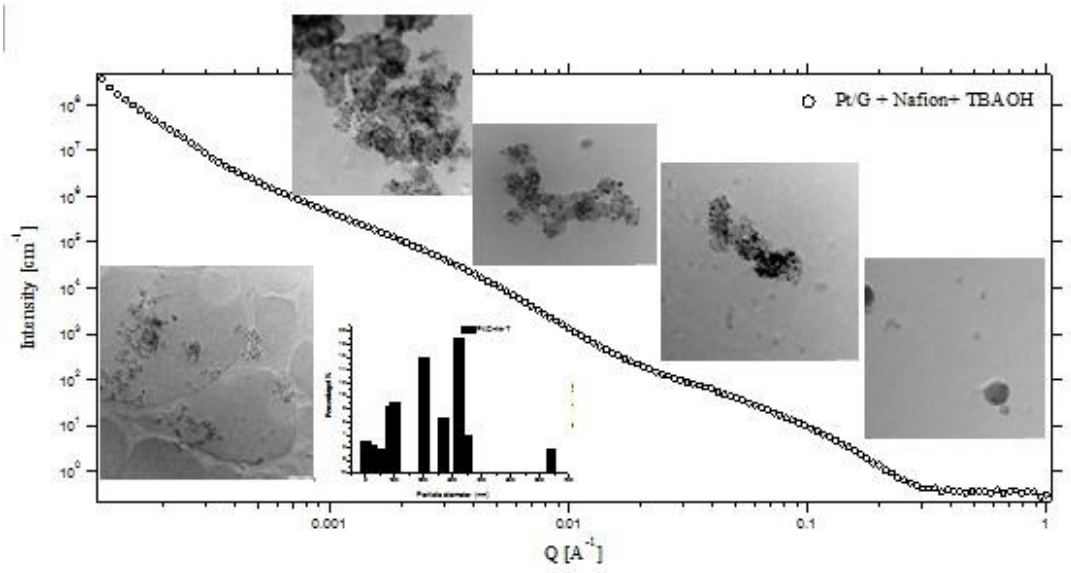

Figure 2.9 USAXS plots of 28% Pt/C+Nafion®+TBAOH solution and Cryo-TEM images of different particles in the sample with the size distribution

The solvent could greatly affect the geometry and particle size of Pt/C. The effect of glycerol on Pt/C aggregates (Figure 2.10.) was also studied. Using the global unified function fitting, the fitting results showed that in the first fitting level, R_{g1} is 9.7 ± 1 nm and the power-law slope P_1 is 2, which could be attributed to mono dispersed spherical particles, a corresponding diameter $d_{sphere} = 2(5/3)^{0.5}R_{g1} = 23.4$ nm can be calculated. The Cryo-TEM image inserted in high Q part in Figure 3.10 revealed the information from sphere single carbon black (diameter = 20 nm). As could be seen from the 400 nm scale TEM image, the percentage of this particle size increase compared to Pt/C+Nafion® system. A more detail information could be obtained from the particle size distribution which showed that the percentage of particles with 20 nm diameter increase from 0.8% (Pt/C+Nafion®) to 6.78% (Pt/C+Glycerol). This could be caused by the glycerol dispersion effect. The second fitting level gave $R_{g2} = 31$ ± 5 nm with the power-law

slope $P_2 = 2.93$. The d_{sphere} based on this particle would be 70 nm. As could be seen from Cryo-TEM image in Figure 2.10, bigger sphere carbon particles with the diameter around 50 to 80 nm were found. The aggregation could not be totally avoided. In the third level fitting, it could be obtained that $R_{g3} = 260 \pm 10$ nm with a Porod slope $P_3 = 4.32$. This could be attributed to rod-like particles (aggregated by Pt/C particles) as could be seen from inserted TEM images. From the overview TEM (400 nm scale) image, compared with Pt/C+Nafion® system, the primary particle size was much smaller (around 60 nm). The particle size distribution was shown in Figure 2.10. A mean size was 85.7 nm.

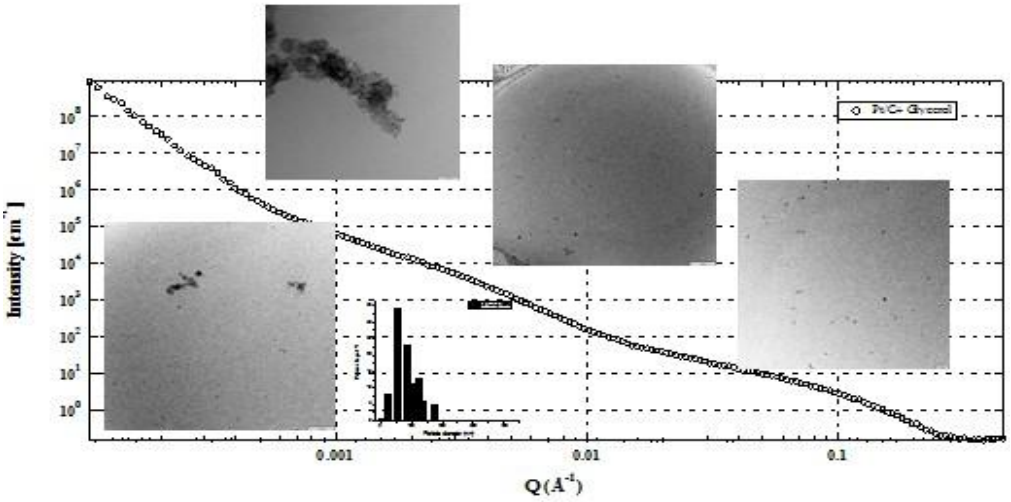

Figure 2.10 USAXS plots of 28% Pt/C+Glycerol solution and
Cryo-TEM images of different particles in the sample with the size distribution

As for the system of Pt/C+Nafion® ionomer+Glycerol, the scattering data and Cryo-TEM images are shown in Figure 2.11. With the same fitting protocol, the fitting results showed that $R_{g1} = 1.6 \pm 0.2$ nm with power-law slope $P_1 = 1.5$ in the first fitting level, which could be attributed to Nafion® ionomer particle. From 0.01 to 0.1 $Å^{-1}$, the second fitting level was employed to get $R_{g2} = 27 \pm 2$ nm with a $P_2 = 3.31$. Assuming this level was domained by monodisperse spherical particles, a corresponding diameter $d_{sphere} = 2(5/3)^{0.5}R_{g2} = 72 \pm 5$ nm can be calculated. The same as before, a sphere like carbon particle was observed in Cryo-TEM image inserted. The percentage of this

particle size is smaller than that of Pt/C+Glycerol system, while bigger than Pt/C+Nafion® system from particle size distribution. The percentages of the particles with ~30 nm radium were about 41% for Pt/C+Glycerol system, 17.4% for Pt/C+Nafion® system, and 24% for Pt/C+Nafion®+Glycerol system respectively, which indicated that the glycerol could greatly improve Pt/C and Nafion® ionomer particle dispersion, and the Nafion® ionomer could cover/bind the carbon black particles to form a bigger particle. Another level fitting was used to fit the lower q region. A power-law slope $P_3 = 3.38$ and $R_{g3} = 159.7 \pm 10$ nm were obtained. From the corresponding Cryo-TEM image, this level could be attributed to rod-like carbon particles. There are about 20 sphere carbon particles (r = ~ 15 nm) aggregated to form a rod like particle (length = 400 nm, width = ~90 nm). The lowest region was fitted to get $R_{g4} = 290 \pm 10$ nm with a power-law slope $P_4 = 2.68$, which is consistent with the agglomerated particle in TEM image. As could be seen from the TEM image, it was found that the carbon rod connected together to form a net like particle, the length could reach about 500 nm, even higher. The particle size distribution was inserted in Figure 2.11. The mean size for Pt/C+Nafion®+Glycerol system was 106.7 nm. The primary particle for this system was 80 nm, according to TEM image, carbon sphere particle composed by one or two mono carbon particles is the domain particle in this system.

Based on the results above, it could be deduced that the catalyst ink system include mono particles (Pt, Carbon, Nafion® ionomer), aggregated particles (Pt/Carbon aggregated particle, carbon/carbon aggregated particle, Nafion®/carbon aggregated particle) and agglomerated particle system. The USAXS data and TEM images of the 28% ink (Pt/C+Nafion®+TBAOH+Glycerol) were listed in Figure 2.12. There are four fitting levels were used for this sample too. The first fitting level showed the contribution from Nafion® ionomer particles with the radius = 1.64 ± 0.2 nm and a power-law slope $P_1 = 3$, which is a little higher than before, which might be caused by the geometry of Nafion® ionomer, however, it is still hard to see the Nafion® ionomer structure in the Cryo-TEM image. The mean size for Pt/C+Nafion®+Glycerol system was 106.7 nm. The primary

particle for this system was 80 nm, according to TEM image, carbon sphere particle composed by one or two mono carbon particles is the domain particle in this system.

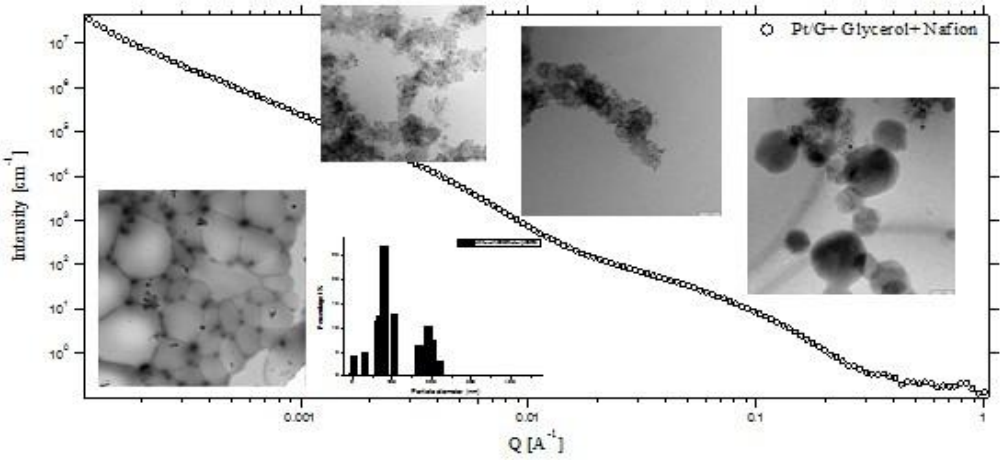

Figure 2.11 USAXS plots of 28% Pt/C+Glycerol+Nafion® solution and Cryo-TEM images of different particles in the sample with the size distribution

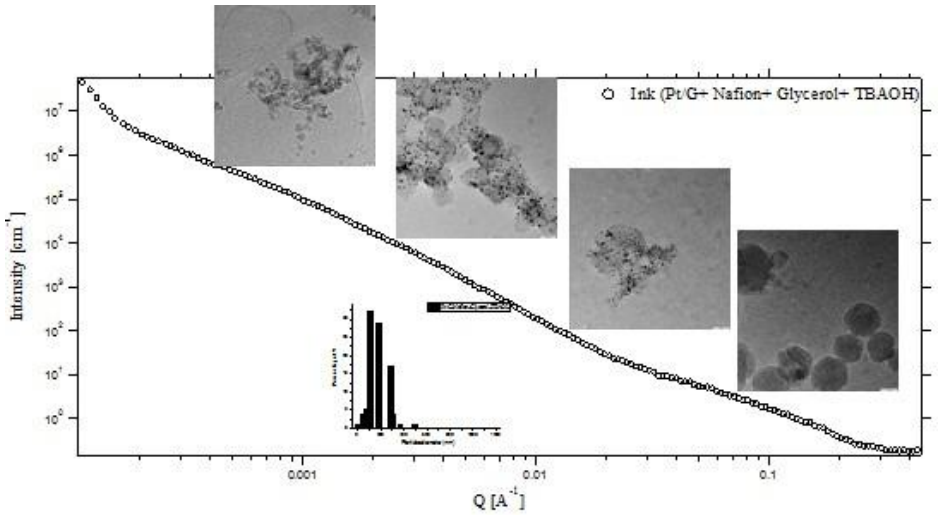

Figure 2.12 USAXS plots of 28% catalyst ink solution and Cryo-TEM images of different particles in the sample with the size distribution

Table 2.2 Summary of geometry and particle size of the fitting results of X-ray measurements

sample	USAXS
Nafion®	Rod L: 21.4 ± 1.4 nm R: 2.4 ± 0.2 nm
Nafion®+G	Rod L: 14 ± 1.4 nm R: 2.8 ± 0.2 nm
Nafion®+G*+T**	Rod: L= 33.3 ~ 48.7 nm
28% Nafion®+Pt/C	Rod: Radius = 1.95 ± 0.2 nm Sphere: Radius = 32 ± 2 nm Sphere: Radius = 33 ± 1.4 nm Rod: Length = 102.7 ± 5 nm Radius = 30 ± 2 nm L like agglomerated particle: Length = 200 ± 10 nm primary particle diameter = 70 ~ 100 nm mean size = 124 ± 5 nm
28% Nafion®+T**+Pt/C	Rod: Radius = 1.8 ± 0.2 nm Sphere: Radius = 32 ± 2 nm Rod: Radius = 1.8 ± 0.2 nm Sphere: Radius = 32 ± 2 nm Rod: Length = 201.7±5nm, Radius = 32 ± 2 nm Agglomerated Particle(island-like) length > 300 nm primary particle size = ~100 nm Mean size = 158 ± 5 nm

Table 2.2 Continued

28% Pt/C+G	Sphere: Radius = 23.4 nm Sphere: Radius = 31 ± 5 nm Rod: length = 260 ± 10 nm Radius = 30 nm primary particle size = ~60 nm mean size = 85.7 nm
28% Pt/C+N+G	Rod: Radius = 1.6 ± 0.2 nm Sphere: Radius = 27 ± 2 nm Rod: Length = 159.7 ±10 nm Radius = 15 nm Rod: Length = 400 ± 10 nm Width = 90 nm primary particle = 80 nm mean size = 106.7 nm
28% Nafion® ink***	Rod: Length = 250 ± 10 nm Sphere: Radius = 23.7±2.5 nm Rod: Length > 290 ± 10 nm primary particle = 100 ~ 200 nm mean size = 176 nm

* G: glycerol;
**T: tetrabutylammonium hydroxide (TBAOH);
***ink: Pt/C aggregates+Nafion®+TBAOH+Glycerol;

Another work is carried out to investigate the detail geometry structure of Nafion® ionomer in catalyst ink. The particle size R_{g2} = 23.7 ± 2.5 nm with a power-law slope P_2 = 3.3 was obtained from the second level fitting. From the results above, a corresponding diameter $d_{sphere} = 2(5/3)^{0.5}R_{g2}$ = 61 ± 5 nm can be calculated by monodisperse spherical particle model, the single carbon sphere particle with radium equal to about 25 nm could be found in inserted TEM image. In the follow TEM image,

there are some aggregated carbon particles (200 nm width and 250 nm length) composed about 21 single carbon particles (r = 12.5 nm), which is consistent with the third level fitting results that R_{g3} = 169.8 $\pm$ 10 nm with power-law slope P_3 = 3.19. From the fourth fitting level, big particle with R_{g4} = 290 $\pm$ 10 nm (power-law slope P_4 = 4) was found.

2.4 Conclusion

The USAXS has been successfully used to study the micro-structural organization of ionomer particles and Pt/C aggregates dispersed in liquid media. Careful and sophisticated data analysis, namely, multiple curve fittings, is required to interpret/extract the correct results from the scattering data. The cryogenic TEM analysis helps to validate the USAXS results, by which the size and geometry of ionomer particles and Pt/C aggregates dispersed in liquid medial was directly observed. The USAXS can distinguish between agglomerated and nonagglomerated catalyst and Nafion® ionomer particles. A detailed quantitative comparison was carried out among the average primary particle diameters from different compositions of catalyst inks for the primary particles of USAXS measurements. TEM was employed to investigate the geometry and particle sizes information. An excellent agreement between these two techniques was obtained. The USAXS data showed that the agglomerate size of catalyst and Nafion® ionomer particle size change significantly with different compositions of the ink, suggesting that interactions between each components exists. The TEM image shows that the catalyst ink was composed by Nafion® ionomer with rod-like particles (d = 3 nm, L = 20 nm), single sphere carbon black particle (d = 30 ~ 70 nm), and rod-like aggregated carbon black particles (R = 150 nm) and some much bigger aggregated particles (R > 200 nm). This work also demonstrated that the size and geometry of a non-uniformed system can also be studied by the USAXS. Further work on the interaction of each component is underway and will be reported in the near future.

3. CARBON CORROSION PROCESS FOR POLYMER ELECTROLYTE FUEL CELLS USING A ROTATING DISK ELECTRODE TECHNIQUE

3.1 Introduction

Automobile manufacturers and fuel cell developers have produced PEMFCs for many years, but recent significant technological advances have left two major remaining challenges to widespread fuel cell use: cost and lifetime, which are interrelated. For example, adding more catalyst to a fuel cell increases catalyst lifetime but increases fuel cell cost. Similarly, increasing a fuel cell membrane's thickness increases its lifetime but also increases its cost by adding material and lowering specific performance. Thus, a complex balance exists between the cost and lifetime of a PEFC. However, since PEFCs currently are not cost competitive for most applications and still do not have sufficient durability, measures to increase fuel cell lifetime that also add expense are not an option. To improve the durability of PEFCs, researchers are studying the factors that determine a PEFC's lifetime, so that the lifetime can be increased without increasing cost or losing performance.

The important properties of a catalyst layer, such as electronic/protonic conductivity, porosity, active reaction area, as well as catalytic activity, are mainly determined by the fabrication method and the properties of the components.

Studies have shown that several factors can reduce the useful life of a PEFC, including platinum-particle dissolution and sintering, carbon-support corrosion, and membrane thinning [1 – 3]. Lifetime can also be reduced by efforts to maximize the initial performance of a fuel cell component. For example, decreasing the equivalent weight of the polymer electrolyte typically increases the membrane's proton conductivity

but also increases its water uptake and gas permeability and degrades its mechanical properties. The conditions under which a fuel cell operates or to which it is exposed can also affect its performance and lifetime. Important operating conditions include impurities in the fuel or oxidant streams, the fuel cell's temperature, its voltage and current, the pressures of the fuel and oxidant streams, and whether it operates continuously or transiently as occurs during start-up and shutdown. The intent of this part is to review the current understanding of hydrogen fueled PEFC degradation.

Within a PEFC, the individual components are exposed to an aggressive combination of strong oxidizing conditions, liquid water, strongly acidic conditions, high temperature, high electrochemical potentials, reactive intermediate of reaction products, a chemically reducing atmosphere at the anode, high electric current, and large potential gradients. In recent years, researchers have realized the importance of understanding the roles of these various conditions in the degradation process and to reduce their effects.

3.1.1 Electro-Catalyst Degradation

In order for the fuel cell to retain the advantages of this optimized structure, it must be resistant to changes in morphology and surface properties. However, there can be significant changes to catalyst structure and properties with operation and electro-catalyst stability may be a determining factor in the useful lifetime of polymer electrolyte fuel cell (PEFC) systems. In this part, we will focus on the review of Pt/C degradation. There are two main mechanisms for Pt degradation. One is platinum dissolution, the other one is platinum growth.

There is a growing body of literature suggesting that platinum dissolution is a major factor limiting the lifetime of polymer electrolyte fuel cells, especially under varying load conditions and at the high potentials of the cathode, though considerably more information is needed in order to fully characterize the mechanisms of oxide formation, platinum dissolution, and redeposition. Xie et al. [25 - 26] studied the durability of PEFC under high humidified condition. Yasuda et al. [27 - 28] studied

electrochemically cycled MEAs using TEM and cyclic voltammetry. The Yasuda's work presented strong evidence for platinum dissolution, diffusion of the dissolved platinum into the membrane, and reduction of the dissolved platinum as particles in the membrane near the membrane-cathode interface by dissolved hydrogen.

Polymer Electrolyte Fuel Cell (PEFC) performance loss under steady-state and cycling conditions has been attributed in part to a loss of electrochemically active surface area (ECSA) of the high-surface-area carbon supported platinum electrocatalyst [29]. There is growing evidence that platinum dissolution plays a major role in the ECSA loss, especially of the cathode catalyst, where high potentials are encountered [30 - 31]. This dissolved platinum can then either deposit on existing platinum particles to form larger particles [31 - 32] or diffuse into electrochemically inaccessible portions of the membrane-electrode assembly (i.e. sites not fulfilling the requirements of gas, electron, and proton access) [31].

There are three primary Pt particle coarsening mechanisms that are believed to be important for PEFCs: (1) Ostwald ripening occurs when small particles dissolve, diffuse, and redeposit onto larger particles, resulting in reduced Pt particle surface area via a minimization in surface energy; (2) re-precipitation occurs when Pt dissolves into the ionomer phase within the cathode and then precipitates out again as newly formed Pt particles; (3) particle coalescence occurs when Pt particles are in close proximity and sinter together to form a larger particle.

In studies of single cell durability testing performed by Borup et al. [22, 33], cathode catalyst particle sizes grew from about 1.9 to 3.5 nm during the drive cycle experiments over 1200 hours of testing. It was found that this extent of growth was much greater than that observed during the steady-state testing, where the particles grew to 2.6 nm at 900 hours and 3.1 nm at 3500 hours. Extremely rapid cathode particle growth was observed in accelerated durability cycling tests (ADT) when cells were cycled to voltages above 1V [33]. During ADT measurements, it was found that catalyst coarsening rates

increase linearly with temperature. Ferreira et al. used a glancing angle X-ray powder diffraction technique to probe the changes in the Pt particle size of the cathode and the anode without removing them from the ionomer membrane [31]. It was found that extensive particle size growth (from 2.3 to 10.5 nm) was seen for the fuel cell cycled cathodes, Xie et al. [25 - 26] found there is a increase of anode Pt particles (1 ~ 6 nm to 3 ~ 15 nm at 500 h) during the degradation experiment.

3.1.2 Degradation of Nafion® Ionomer in Catalyst Layer

The Nafion® ionomer network in catalyst layer functions not only as a binder, but also as the necessary proton transport pathway. Therefore, the degradation of Nafion® ionomer network not only decreases the proton conductivity of catalyst layer, but also enhance the dissolution of Pt particles, even causes the crush of catalyst layer structure. While a significant amount of work has focused on the degradation of Nafion® membrane, little has been done regarding the degradation of ionomer in the catalyst layer.

3.1.3 Corrosion of Catalyst Support

The lifetime issues of the electrodes, which include stability of materials as well as of structure, are discussed for the different phases of which the electrodes are composed. Carbon corrosion results in the degradation of the catalyst layer, which not only causes a decrease of the electrochemically active surface area (ECSA) [34] and an increase in the total resistance because of the loss of structural integrity [32], but also has an effect on the Pt particle growth [35] and causes an increased mass transfer loss due to the increased hydrophilicity within the catalyst layer [36 - 38].

On a commercial carbon support surface (Vulcan XC72 carbon black), the carbon oxidation occurs at 65 ℃, and a potential of > 0.8 V (*vs.* RHE) was reported by Xie et al. [39] and Jarvi et al. [40]. In the work of Borup et al. [22] and Mathias et al. [41] it was observed that at 1.2 V, a commercial Pt/C catalyst lost 15% of its weight after 20 hours testing. Carbon support is stable at steady-state conditions; however, severe carbon

corrosion will occur during startup/shutdown cycles and fuel starvation because a high potential spike (about 1.2 to 1.5 V) is established during the startup/shutdown period as well as in the fuel starvation regions [42 - 44]. PEFCs in automotive applications undergo an estimated 30,000 startup/shutdown cycles over the lifespan of a vehicle [45], which will negatively cause carbon corrosion to affect durability and lifespan. Borup et al. indicated that carbon corrosion during start–stop cycles worsened in low humidity [33, 49]. Dowlapalli [39] and Roen et al. [47] showed that the existence of Pt nanoparticles on the surface of carbon accelerated the corrosion of the carbon support.

The corrosion of carbon supports in PEFCs has been investigated by several groups [48 - 52]. In MEA, the most common methods for carbon corrosion testing include load on–load off cycles [38], simulated drive cycles [33], OCV conditions [31] and high voltage cycles [31] (0.9 V to 1.5 V versus RDE) under H_2/N_2 and H_2/air. It was found by Ferrier et al. [31] that a 46% loss of ECSA was measured at 0.2 A cm^{-2} (0.75 V) after 2,000 hours. While in OCV (0.95 V) conditions, a 75% loss was observed over the same period. However, after 10,000 cycles between 0.87 and 1.2 V in just 100 hours, 69% of the ECSA was lost. Carbon corrosion in the catalyst layer of the PEFC can be monitored by determining the amount of CO_2 gas emitted from a running cell by GC and NMR [53 - 55]. SEM can also be employed to observe the carbon corrosion of the catalyst layer [44]. Hyun et al. [57] employed low-angle annular-dark-field (LAADF) STEM tomography to examine the three-dimensional morphology and structure of corroded carbon/Pt systems. Some researchers observed that the catalyst layer becomes thinner after carbon corrosion [58 - 59]. Li et al. [56] observed a 50% cathode catalyst layer thickness loss in a highly corroded region after 220 potential cycles (0.6 to 1.0 V). Shi et al. [60] showed the carbon corrosion from the C/F atomic ratio by EDX. However, it is difficult to decouple the carbon corrosion in MEAs from the experimental data due to the complexity of the PEFC degradation, because in fuel cells, there are different degradation processes occurring at the same time (degradation of Pt and alloy catalyst nanoparticles, ionomer degradation, membrane degradation, and carbon corrosion). In addition, it is difficult to decouple the carbon corrosion in MEAs from the experimental and the study of carbon

corrosion using an MEA configuration takes a long period of time to complete. Colon-Mercado et al. [61] developed an accelerated durability test in a simulated fuel cell system to investigate carbon corrosion in a three-electrode system using an RDE.

However, little work has been reported on the corrosion process, or on the fine structure of carbon black support corrosion in PEFCs. In a previous publication, it was shown that higher degradation of the carbon support was observed at higher potentials. For this reason, in this work, I concentrated the efforts on studying the durability of the carbon support from 0.85 to 1.4 V (vs. NHE), where the major damage is expected to occur during fuel cell operations. This chapter presents an investigation of carbon corrosion using an accelerated degradation test under the conditions similar to those in fuel cells using a Rotating Disk Electrode (RDE). In MEA configuration, it is difficult to decouple the different degradation process such as Nafion® ionomer degradation, Pt degradation and membrane degradation. A steam etching method was also employed to confirm the carbon corrosion processes of the two carbon supports (XC72 CB and BP2000). The corrosion process can provide a powerful guide for the development of high resistance carbon support, which can greatly increase the durability of PEFC.

3.2 Experimental Section

3.2.1 Electrochemical Measurement Principle and Theory

The rotating disk electrode method (RDE) has been widely used for electrochemical analysis and evaluation, as it can ensure an electrode reaction under well-described hydrodynamic conditions. Recently, with the development of PEFCs, it has been widely used to screen the activity of some electrocatalysts towards fuel cell reactions, such as oxygen reduction [62 - 64], hydrogen oxidation [65], methanol oxidation [66], and CO tolerance [67] in simulated fuel cell environments. Thin-film RDE [68] and porous RDE [64] are the types commonly used in the study of PEFCs. For a thin-film RDE, the glass carbon disk is usually covered by two layers. One is the inner layer of the catalyst and the

other is the Nafion® outer layer. In this case, the reactant (O_2 or H_2) first diffuses through a Nafion® film and then reacts at the catalyst surface. This situation is comparable to the simulated "thin-film" model of fuel cell electrodes.

Equations [69] used for RDEs are as follows:

$$1/I = 1/I_k + 1/I_{lev} \qquad \text{Eq. 31}$$

(the Koutecky-Levich equation) where I is the disk current density, I_k is the kinetic current density, and I_{lev} is the Levich current density. I_k can be expressed as Equation 3.2:

$$I_k = nFAK_{O2}\, C_{O2}\, \Gamma_{catalyst} \qquad \text{Eq. 3.2}$$

where n is the overall electron transfer number, A is the electrode area, C_{O2} is the concentration of dissolved O_2, and catalyst Γ is the surface concentration of the catalyst, or the catalyst loading. I_{lev} can be expressed as Equation 3.3:

$$I_{lev} = 0.201nFAD_{O2}C_{O2}v^{-1}w^{0.5} \qquad \text{Eq. 3.3}$$

where D_{O2} is the diffusion coefficient of O_2, v is the kinematic viscosity of the electrolyte solution, and ω is the rotation rate represented by rpm.

The advantage of this method is that the steady state is achieved rather quickly. The mass transfer to the electrode surface is faster than in case of stationary electrodes where mass transfer is determined solely by diffusion. Consequently, the influence of mass transfer to the electron-transfer kinetics is in general smaller than in case of stationary electrodes. The RDE system is a convective electrode system for which both the hydrodynamic equations and the convective diffusion equations have been solved for steady state conditions. In my research, only one layer was employed, there is no ionomer.

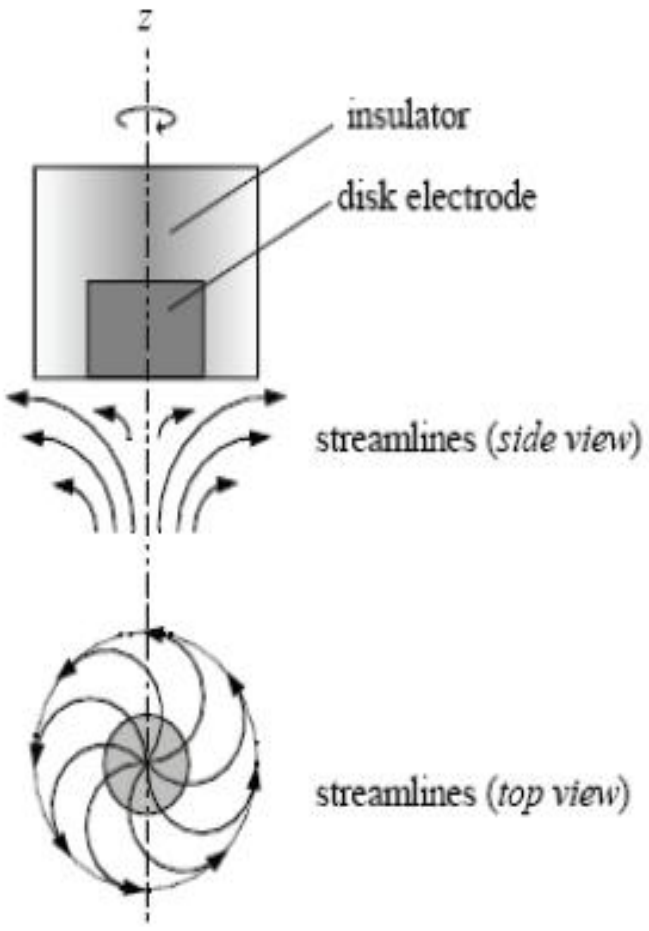

Figure 3.1 Scheme of a rotating disk electrode (RDE) setup with streamlines (top view and side view) in the electrolyte

Cyclic voltammetry (CV) is one of the most widely used electrochemical techniques for acquiring qualitative information about electrochemical reactions. Measurement using cyclic voltammetry can rapidly provide considerable information about the thermodynamics of redox processes and the kinetics of heterogeneous electron-transfer reactions, as well as coupled chemical adsorption and reactions. Cyclic voltammetry is often the first experiment performed in an electroanalytical study. In particular, it can quickly reveal the locations of the redox potentials of the electroactive species. CV is also used to measure the electrochemical surface area (ECSA, m^2/g catalyst) of electrocatalysts (e.g. Pt/C catalyst) in a three-electrode system with a catalyst coated glass carbon disk electrode as a working electrode. A typical CV curve on Pt/C is shown in

Figure 3.2. Peaks 1 and 2 correspond to hydrogen electroadsorption on Pt(100) and Pt (111) crystal surfaces, respectively. The H_2 electroadsorption can be expressed as Equation 3.4

$$Pt + H^+ + e^- \rightarrow Pt\text{-}H_{ads} \qquad \text{Eq. 3.4}$$

Peaks 3 and 4 correspond to H_2 electro-desorption on Pt(111) and Pt(100) crystal surfaces, respectively, and can be expressed as:

$$Pt\text{-}H_{ads} \rightarrow Pt + H^+ \qquad \text{Eq. 3.5}$$

Peak 5 represents the oxidation of the Pt surface; this process can be expressed as follows:

$$Pt + H\text{–}O\text{–}H \rightarrow Pt\text{–}O$$
$$Pt\text{–}O\text{–}H + H\text{–}O\text{–}H \rightarrow Pt\text{–}(O\text{–}H)_2 + H^+ + e^-$$
$$Pt\text{–}(O\text{–}H)_2 \rightarrow Pt\text{–}O + H\text{–}O\text{–}H \qquad \text{Eq. 3.6}$$

Peak 6 represents the reduction of Pt oxide, which can be expressed as Eq. 3.7:

$$Pt\text{–}O + 2H^+ + 2e^- \rightarrow Pt + H\text{–}O \qquad \text{Eq. 3.7}$$

The ECSA (m^2/g Pt) can be calculated according to Eq. 3.8:

$$ECSA = Q_H / L_{Pt}Q_f 10^{-4} \qquad \text{Eq. 3.8}$$

where Q_H is the Coulombic charge with a unit of mC, and the value is usually calculated as the average value between the amounts of charge exchanged during the electroadsorption (Q') and electrodesorption (Q'') of H_2 on Pt sites; L_{Pt} is the Pt loading on the studied electrode, with a unit of g; Q_f is the required Coulombic charge to desorb

the hydrogen when a clean Pt surface is covered by a monolayer of hydrogen, and its value is 0.21 mC/cm^2_{Pt}.

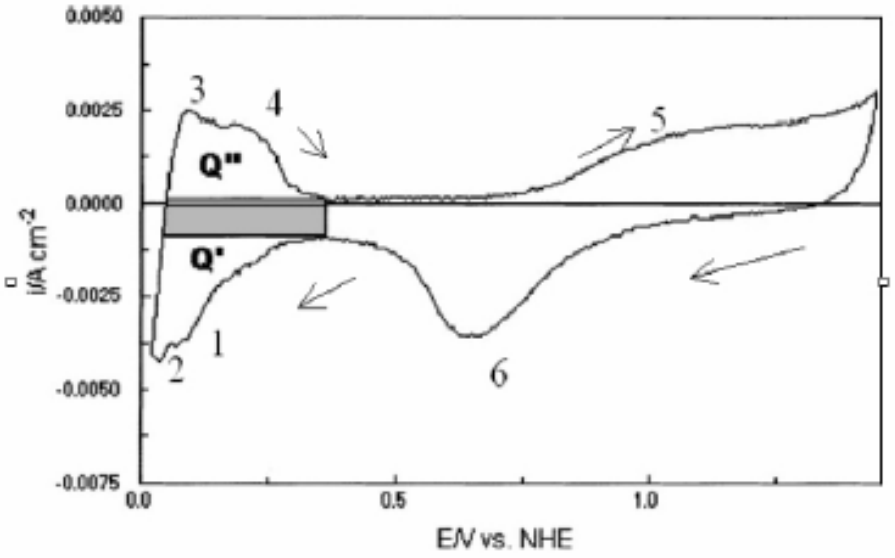

Figure 3.2 Typical CV curve on Pt/C catalyst.

3.2.2 Preparation of the Catalyst by Hydrogen Reduction Method

Two catalyst supports were used: a low-surface-area (254 m^2/g) carbon black Vulcan XC72 and a high-surface-area (1500 m^2/g) Black Pearl BP2000, both from Cabot (Billerica, MA).

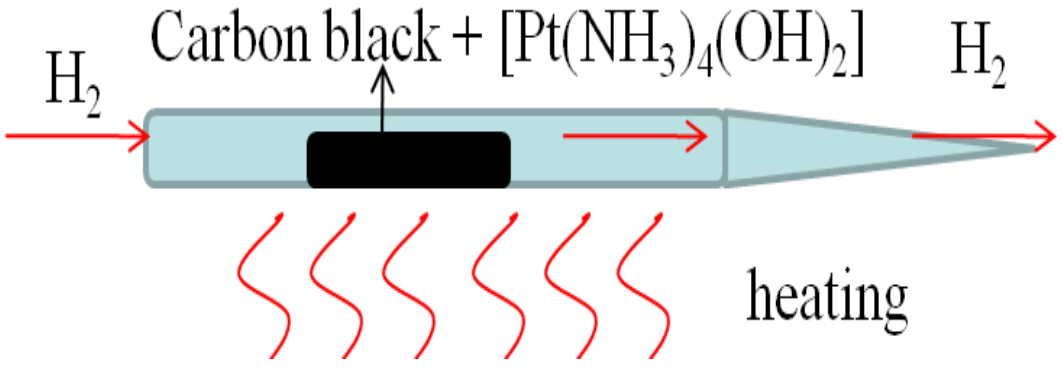

Figure 3.3 Hydrogen reduction system

Both of the carbon blacks were immersed in a 10 g $\cdot L^{-1}$ platinum precursor $[Pt(NH_3)_4(OH)_2]$ salt solution (Fisher Scientific, NJ). The mixture of the carbon blacks and the platinum precursor was dried in the oven at 110 °C. Reduction of the adsorbed platinum precursor to a metallic form was carried out by treatment with hydrogen gas (research grade, 99.999% purity: Praxair) at elevated temperatures. Reduction of the adsorbed platinum precursor to a metallic form was carried out by treatment. Generally, the preferable temperature of the reducing reaction is in the approximate range of < 200 °C. For the exact amount of Pt on carbon, the TGA was used to determine the Pt loading for 20% Pt/XC72 and 20% Pt/BP2000. The system is shown in Figure 3.3.

3.2.3 Electrochemical Experiments.

A glassy carbon rotating disk electrode (GCRDE) (shown in Figure 3.4) was used as the working electrode (0.196 cm^2, Pine Instruments, Inc., Raleigh, North Carolina).

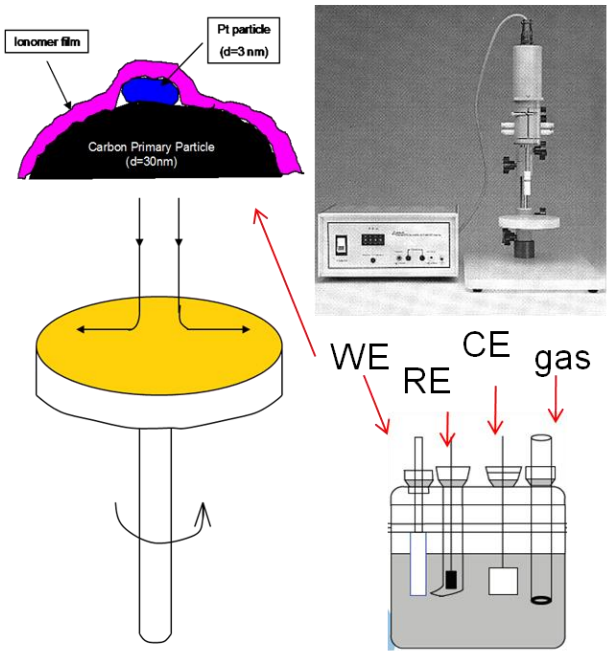

Figure 3.4 Thin film electrodes and three-electrode rotating disk electrode system.
(Working electrode: thin film glassy carbon electrode,
Reference electrode: Ag/AgCl, Counter electrode: Pt wire)

The GCRDE was polished with a 0.3 μm followed by a 0.05 μm alumina suspension to give it a mirrored finish. Sonication was used to suspend 35 mg of Pt/VXC72 (Billerica, MA) (or Pt/BP2000 (Billerica, MA)) catalyst in a solution of 200 μL 5 wt. % Nafion®, 3 mL isopropyl (70%, Fisher Scientific, NJ), and 2 mL DI water (Millipore pure water systematic Milli RO60) for 5 mins. A total of 10 μL of the Pt suspension (loading: 0.35 mgPt/cm^2) was pipetted onto the glassy carbon and was dried at room temperature overnight. Electrochemical measurements were carried out using three compartments, a catalyst/GC as a working electrode, a Pt wire (0.5 mm OD x 152 mm L, 99.95%) as a counter electrode, and an Ag/AgCl (Pine Instruments, Inc) as a reference electrode. Electrochemical measurements were recorded using a PARSTAT 2273 advanced electrochemical system (Princeton Applied Research, Oak Ridge, Tennessee). All potentials cited in this article were normalized with respect to the normal hydrogen electrode potential (NHE).

All experiments were performed at room temperature. After preparation of the catalyst on the glassy carbon, the catalyst was electrochemically cleaned by potential cycling between 0.05 and 1.2 V at 1 V/s for 200 cycles in a N_2 (research grade, 99.999% purity: Praxair) saturated 0.1 M $HClO_4$ electrolyte (60%: Fisher Scientific, NJ). To perform the ADT, a cyclic voltammogram was used with a scan rate of 20 mV/s between 0.85 and 1.4 V. The area under the desorption peak of underpotentially deposited hydrogen in a cyclic voltammogram (CV) (scan rate of 20 mV/s between 0.05 and 1.2 V) was used to evaluate the ECSA of the Pt catalyst on the electrode. Polarization curves for the oxygen reduction reaction (ORR) on the RDE were recorded by scanning the potential from 0.05 to 1 V at 20 mV/s in oxygen saturated (research grade, 99.999% purity: Praxair) 0.1 M $HClO_4$ and rotating the RDE at 1600 rpm. The procedure of the ADT was carried out by *1*) running 1800 consecutive ADT cycles and measuring the ECSA and the polarization curve before and after the ADT; and *2*) taking the ECSA and polarization curve measurements every 300 cycles during the ADT until 1500 cycles were finished. All mass and specific activities were calculated at a current of 0.75 V vs NHE, given the known mass and area of Pt.

3.2.4 Steam Etching Experiment

XC72 and BP2000 were employed. XC72 and BP2000 were employed. A tube furnace (with gas inlet and exit) was designed to be used for the steam etching process. The aggregates of these carbon black powders were milled before etching experiments. The milled carbon black powders were placed into the tube furnace and then were purged with nitrogen while the temperature was increased through programmed heating at a heating rate 5 °C/min. The steam was introduced into the furnace when the furnace reached the desired temperatures and the steam continued flowing through the furnace for a certain length of time. The flow rate of the steam (vapor) was 0.5 cm^3/min and the flow rate was the same in all experiments. The steam etching experiments lasted for 3 hours at 800 ℃.

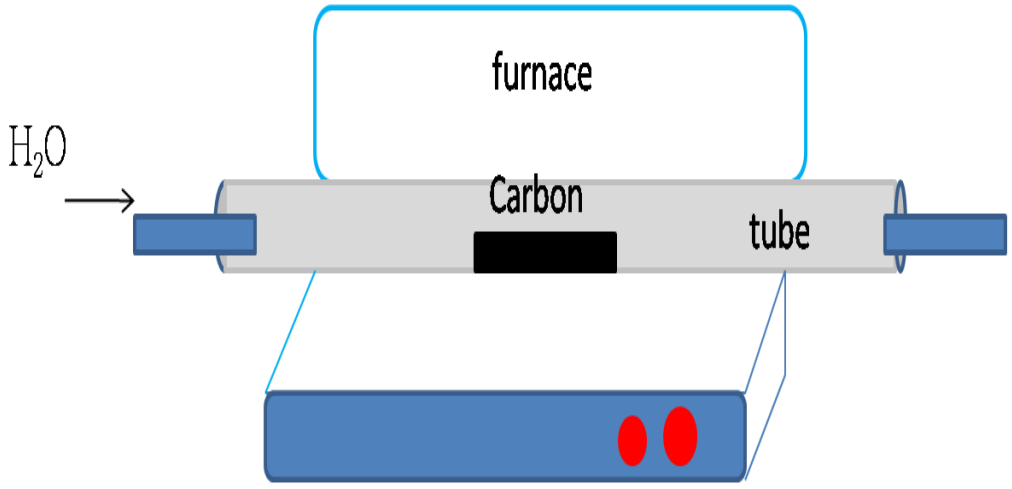

Figure 3.5 Scheme of steam etching experiment

3.2.5 Characterization of Steam Etched Carbon Blacks.

After the 1800 consecutive ADT and steam etching experiments, the catalyst was collected for the morphology examination using a Hitachi S - 4800 scanning electron microscope (SEM) and a Philip Tecnai 20 transmission electron microscope (TEM). Image J 1.42 software was used to determine the average particle size and the size distribution; about 200 particles were analyzed.

3.3 Results and Discussion

3.3.1 Activity Degradation for the ORR

The principal objective of this study in this chapter was to investigate the carbon black corrosion process for PEFCs using a Rotating Disk Electrode (RDE) approach under simulated PEFC conditions, and to provide a model system for studying the catalyst support corrosion mechanism for PEFCs.

The typical CV and polarization curve results, before and after consecutive ADT (1800 cycles), respectively, are shown in Figure 3.6(a) and 3.6(b) for Pt/XC72, and in Figure 3.6(c) and 3.6(d) for Pt/BP2000. Assuming the hydrogen adsorption–desorption process was on a polycrystalline Pt surface, the ECSA was determined by integrating the H_{up} peak. The pair of peaks observed between 0.05 V and 0.30 V (*vs.* NHE) corresponded to the desorption–adsorption of hydrogen on the Pt surface. With ADT cycling, a reduction on the H_{up} peak was observed for both catalysts, indicating an increase in Pt particle size due to Pt nanoparticle agglomeration [70]. After 1800 consecutive cycles, the ECSA loss of Pt/XC72 was 64.2%, which was less than that of the Pt/BP2000, 80.4% (Table 3.1). An interesting phenomenon can be seen in Figure 3.6(c): a redox couple appeared at 0.55 V and 0.60 V in the voltammogram of the Pt/BP2000 catalyst after 1800 cycles. This redox couple corresponds to the redox couple of quinone/hydroquinone, a carbon corrosion product, $C + O_2 \rightarrow$ quinone [71]. However, as seen in Figure 3.6(a), such a redox couple was not obvious in the voltammogram of the Pt/XC72 after cycling. It seems that this redox couple was hidden in the broad peaks between 0.40 - 0.80 V, which may suggest a different carbon corrosion mechanism for XC72 than for BP2000.

The polarization curves for Pt/XC72, (b), and Pt/BP2000, (d), at room temperature in 0.1 M $HClO_4$ saturated with O_2 using a GCRDE at 1600 rpms are presented in Figure 3.6. At high potentials (between 0.96 and 0.80 V versus NHE), the ORR was under the kinetic control. This region was followed by a mixing control region of charge transfer

and mass transfer. As can be seen in Figure 3.6, the difference between the Tafel slopes of before and after 1800 ADT cycles for both Pt/XC72 and Pt/BP2000 were very small, suggesting that the change of catalytic activity of both catalysts was minimal. In other words, the degradation of catalyst Pt nanoparticles during the ADT cycling was not the dominating process. As found in Table 3.1, the mass activity of the catalysts after cycling became worse. The mass activity (current density at 0.75 V versus NHE) loss of Pt/XC72 and Pt/BP2000 was 75.6% and 84.6%, respectively, which is very similar to the losses in ECSA for both catalysts (mainly attributed to Pt nanoparticle agglomeration). Therefore, it can be concluded that Pt/BP2000 is less stable than Pt/XC72 under equivalent conditions, which might be due to the higher surface area of the BP2000 [34] (1450 m^2/g vs. the 250 m^2/g of XC72). It is clearly shown in Figure 3.6(b) and Figure 3.6(d), that the polarization curves of each catalyst before and after cycling were parallel with each other, suggesting that the Tafel slopes of the catalysts do not change much, and hence, the catalytic activity is similar. However, each polarization curve after cycling shifted downward at the same current density, indicating that a huge potential drop occurred for each catalyst after cycling. This potential drop was almost constant in the whole potential range of the polarization curve, suggesting that this potential drop must have been caused mainly by the increased electron resistance between the carbon particles. If this potential drop were caused by the mass transport (hydrophilic groups generated from carbon corrosion will increase the flooding at a high current density range), then a lower potential drop at a high potential range would be expected, which is not seen here. In an MEA configuration, the carbon corrosion will cause the increased hydrophilicity within the pores of a catalyst layer due to the produced hydrophilic groups (i.e. ketone and pheonyl groups) [32, 39, 71] from the carbon corrosion, hence these pores are filled with water, and gas reactant transport is severely hindered and the steep decrease of the current density is seen as cell voltage goes down (i.e < 0.60 V), namely “flooding” . If this potential drop were caused by the mass transport (hydrophilic groups generated from carbon, it is what we designed slopes of the catalysts do not change much. However, in the RDE configuration the thin catalyst layer on the glassy carbon electrode is completely immersed in the liquid electrolyte. Hence, there is no gaseous reactant transport issue,

and consequently, no flooding should be observed. Therefore, the huge voltage drop for each catalyst after cycling must have been caused mainly by the carbon corrosion.

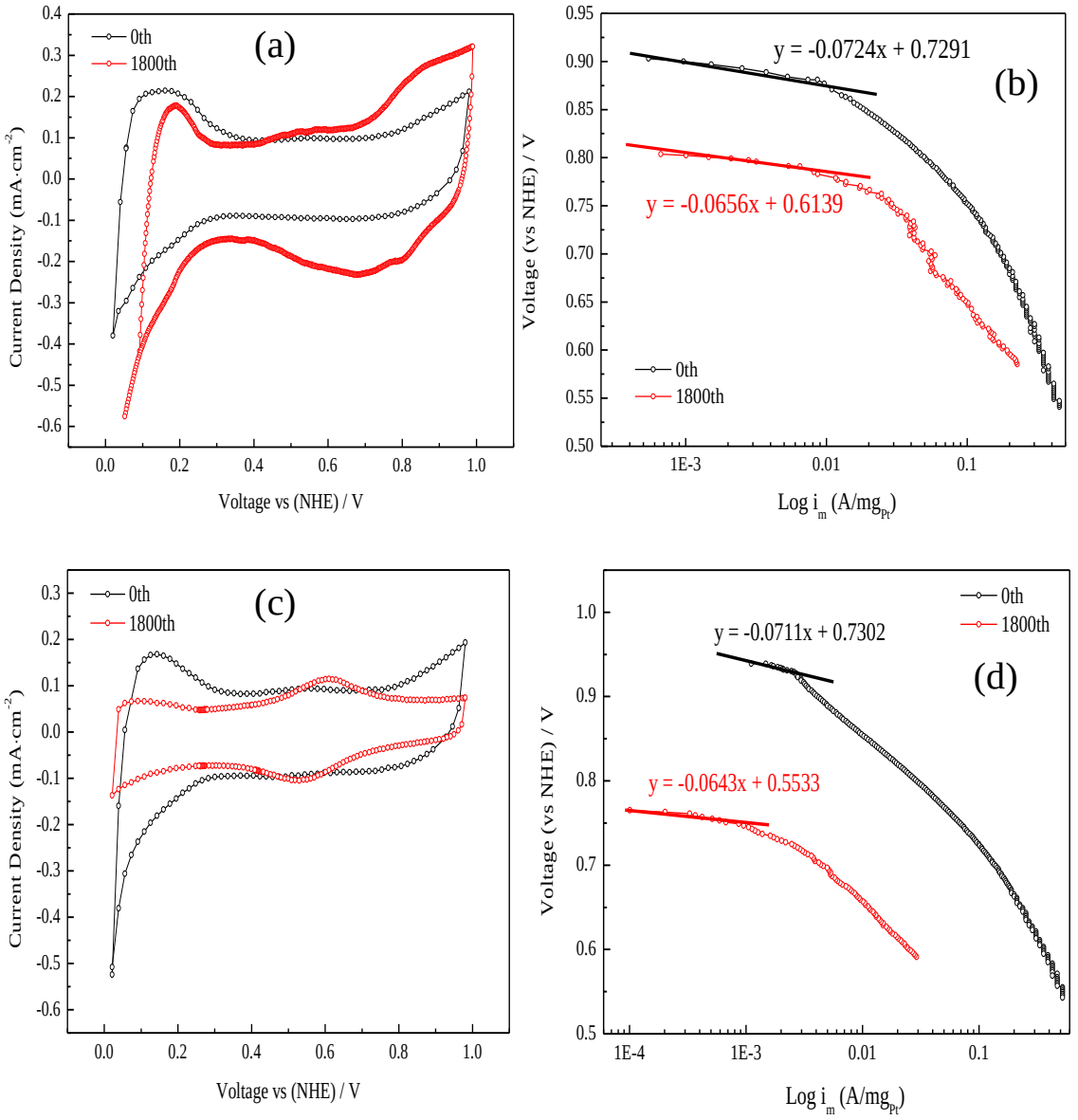

Figure 3.6 Voltammograms and polarization curve for different Pt-based carbon supports before and after 1800 ADT cycling (a) and (b) Pt/XC72, (c) and (d) Pt/BP2000

To measure the performance of the catalyst during the ADT cycling, the catalysts were exposed to extremely corrosive conditions. The Pt nanoparticles on the carbon

surface experienced an extensive particle agglomeration process through the surface migration of catalyst nanoparticles under the potential cycling in the solution. The carbon corrosion facilitated the surface particle migration by weakening or even breaking the interaction/bonds between the Pt nanoparticles and the carbon supports. The carbon corrosion also caused the detachment of the Pt nanoparticles from the carbon support, which may have formed agglomerates or been washed away in the water, particularly when the current density was high. Thus, the carbon corrosion contributed a great deal to the catalyst performance loss. By cycling the catalyst in acidic media, the corrosion of the carbon support could have also resulted in a significant loss of catalyst performance. For the platinum catalyst, Pt nanoparticles on different carbon supports (XC72 and BP2000) were oxidized into ions and migrated/dissolved into the electrolytes under high potentials (i.e. > 0.85V) [72]. Then the dissolved Pt ions were redeposited on the surface of the larger particles, a phenomenon known as Ostwald ripening [73]. As for the carbon corrosion, it could have not only increased the resistance of the catalyst layer (carbon support serves as the electron conductor in catalyst layer), but also could have partly enhanced the aggregation of the Pt particles (the interaction between carbon support and Pt will decrease if the carbon is corroded), and thus caused the migration and dissolution of the Pt particles. Therefore, the ECSA and mass activity loss can be attributed to the increase in the Pt particle size [32] and the carbon support corrosion.

Table 3.1 ECSA and kinetically controlled ORR currents at 0.75V vs. NHE for the Pt-based different carbon supports before and after 1800 consecutive ADT cycling

At 0.75 V		i_m (A/g)	ECSA (m^2_{Pt}/g_{Pt})
Pt/XC72	0th	98.7	89.7
	1800th	24.1	32.1
	Loss (%)	75.6%	64.2%
Pt/BP2000	0th	68.7	54
	1800th	10.58	10.6
	Loss (%)	84.6%	80.4%

3.3.2 Electrochemical and Physical Characterization of the Electrode Surface Area as a Function of Time

In order to further investigate the corrosion resistance of Pt/XC72 and Pt/BP2000, CV and polarization curve testing were carried out every 300th cycle during a 1500 ADT (0.85 V to 1.40 V, scan rate 20 mV/s) until catalyst failure. The CV curves as a function of the cycle number obtained for Pt/XC72, (a), and Pt/BP2000, (c), during ADT cycles are shown in Figure 3.7. Before the ADT, a 200-cycle scan with a scan rate of 1 V/s between 0.05-1.20 V was taken to achieve a full saturation of the active material (thin Nafion® layer covering the catalyst layers) with the electrolyte, similar to the "Break-in" of an MEA. After this process, in both the Pt/XC72 and the Pt/BP2000, it was observed that the electrochemically active surface area decrease started with the cycling number, according to the hydrogen adsorption–desorption potential, in the region between 0.05 and 0.30 V (*vs.* NHE), which is caused by the increase of Pt particle size and carbon corrosion. (The pair of peaks at 0.55 V (*vs.* NHE) corresponding to carbon oxidation [71] became more and more obvious after the 600th cycle. This phenomenon can be attributed to the carbon corrosion in the ADT process). For further analysis, the ECSA change trend as a function of the cycling number of Pt/XC72 and Pt/BP2000 is presented in Figure 3.7(b) and (d). Through careful observation, it was found that the decrease rate of ECSA for the Pt/XC72 was slower than that of the Pt/BP2000, especially before the first 600 cycles. In the case of Pt/XC72, for 1500 ADT cycles, the ECSA decrease rate was 0.037 $m^2_{Pt}/(g_{Pt}$ cycle), however for the first 600 cycles, the rate was 0.0125 $m^2_{Pt}/(g_{Pt}$ cycle). In the case of Pt/BP2000, the ECSA decrease rates were 0.0275 $m^2_{Pt}/(g_{Pt}$ cycle) and 0.0325 $m^2_{Pt}/(g_{Pt}$ cycle) for the 1500 and the first 600 cycles, respectively. This phenomenon not only indicates that the Pt particle migration and sintering occur at a higher rate in the BP2000 as compared to the XC72 but also indicates that the corrosion resistance of Pt/XC72 is higher than that of Pt/BP2000, especially in the initial period.

Double Layer Capacity (DLC) was also obtained by integrating the CV curve from 0.32 V to 0.38 V (*vs.* NHE) for both Pt/XC72 and Pt/BP2000. Double layer capacity is directly propositional to the carbon surface area. In order to compare the exact change of the DLC of the catalyst layer and the electrolyte, the CV curve was also measured on a

fresh glassy carbon electrode (without any catalysts) after it went through the exact same ADT process. All the values shown in the right axis of Figure 3.7(b), Pt/XC72, and Figure 3.7(d), Pt/BP2000, have had the DLC values subtracted from those of the fresh glassy carbon electrode, which served as the background. In the case of Pt/XC72, the DLC initially increased, then maintained the same level from the 300th to the 900th cycle, and then decreased after the 900th cycle.

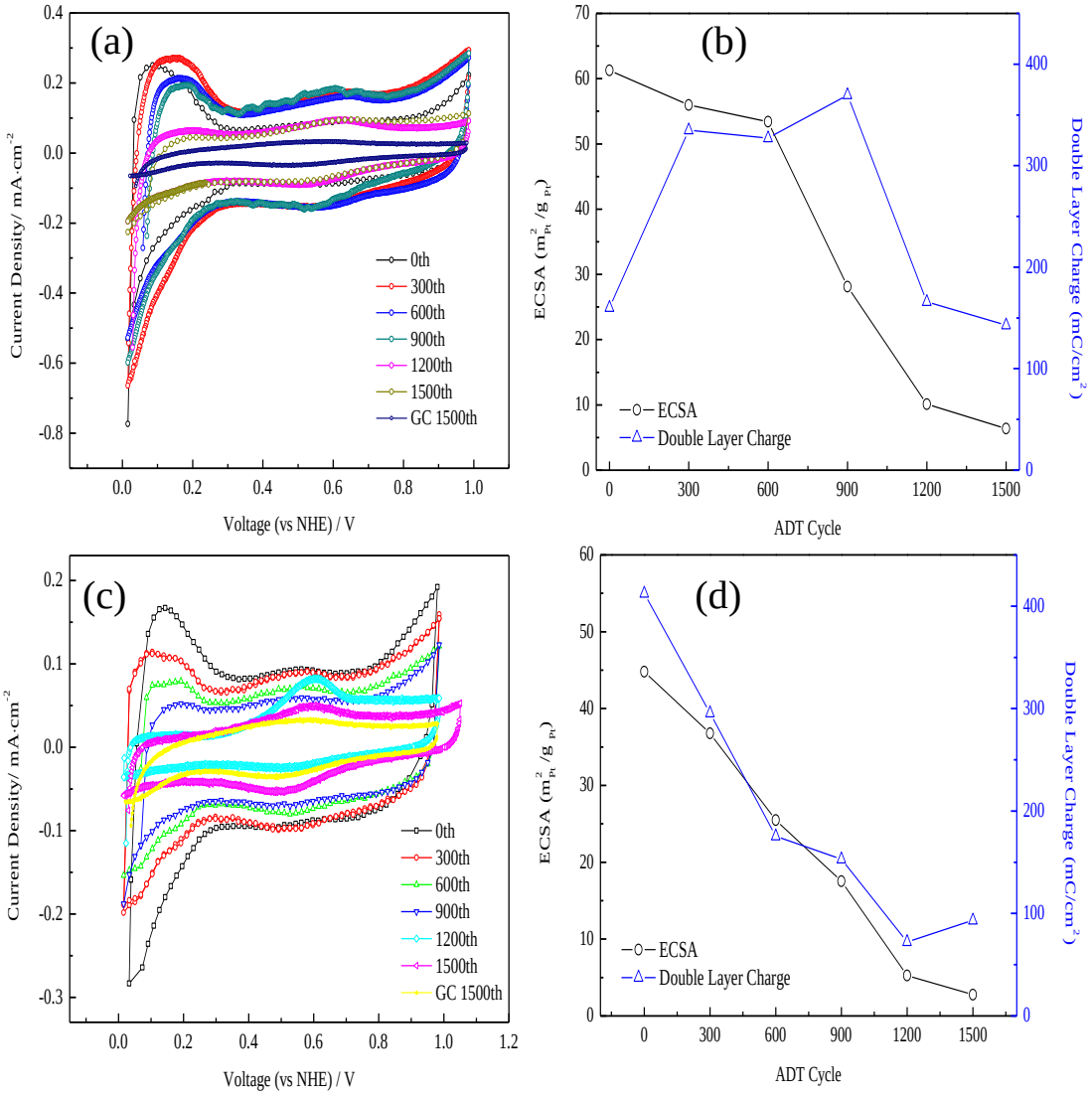

Figure 3.7 Voltammograms, Electrochemical surface area (ECSA) and Double Layer Charging (DLC) as a function of cycling after every consecutive 300 cycles for (a) and (b) Pt/XC72, (c) and (d) Pt/BP2000

However, in the case of Pt/BP2000, the DLC showed a different trend with an increase in the number of cycles, it decreased at a much higher rate (0.23 mC/cm^2 cycle) compared to that of the Pt/XC72 (0.15 mC/cm^2 cycle), especially between the 300^{th} and the 900^{th} cycles (0.05 mC/cm^2 cycle for Pt/XC72 and 0.26 mC/cm^2 cycle for Pt/BP2000). The increase of DLC in Pt/XC72 suggests that the carbon corrosion may take place starting from the center of the carbon particles, which results in more surface area; further corrosion causes the loss of the carbon particles from the catalyst layer, which results in the loss of electric contact with the bulk, indicated by the decrease of the DLC after 1200 cycles. On the other hand, the decrease of the DLC for the Pt/BP2000 shows a linear relationship with the cycle number, suggesting a continuous loss of surface area for the BP2000 carbon particles during cycling. The different trends of the DLC of Pt/XC72 and Pt/BP2000 with regard to cycle number indicate the different carbon surface area changes during the carbon corrosion process, and in turn, different carbon corrosion mechanisms.

To further illustrate the carbon corrosion of the two catalysts, the polarization curves after different cycle numbers are shown in Figure 3.8. The different potential ranges of the polarization curves correspond to different control steps: OCV - 0.85 V is the kinetic control, 0.85 - 0.65 V is the ohmic control range (i.e. mixing control of both kinetic and mass transport), and a potential below 0.65 V is in the mass transport control range. To observe the effects of potential cycling on the performance, the ORR mass activity current density at 0.85 V (kinetic performance), 0.75 V (ohmic performance), 0.65 V (mass transport performance) (*vs.* NHE) as a function of cycle number, respectively, are presented in Figure 3.8. The mass activity loss with the cycle number for Pt/XC72, 3.8(a) and 3.8(b), and Pt/BP2000, 3.8(c) and 3.8(d), obtained at room temperature in 0.1M $HClO_4$ saturated with O_2 using a GCRDE at 1600 rpm are presented in Figure 3.8. The current density decay rates at 0.85, 0.75, and 0.6 V were 0.02, 0.08, and 0.13 ($A\ g^{-1}\ cycle^{-1}$) for Pt/XC72; 0.018, 0.07, and 0.125 ($A\ g^{-1}\ cycle^{-1}$) for Pt/BP2000. These values indicate a strong correlation between Pt particle agglomeration, carbon corrosion, and the value of the mass activity current density decay. It can be easily seen that, for both Pt/XC72 and Pt/BP2000, the kinetic performance degradation (due to the catalytic

activity change) indicated by the mass activity current density at 0.85 V (*vs.* NHE) was much smaller than the mass transport performance degradation, indicated by the mass activity current density at 0.65 V (*vs.* NHE) (0.02 and 0.018 *vs.* 0.13 and 0.125 A g^{-1} $cycle^{-1}$). The mass transport performance is determined by the morphology and hydrophilicity of the carbon particle surface, and consequently, by the carbon corrosion during the ADT cycle. The higher degradations of the mass transport performance in Figure 3.8(b) & 3.8(d) suggest that carbon corrosion plays a much bigger role than catalyst degradation on affecting the performance during the ADT cycling. The trends of mass activity loss are very similar to those of the ECSA shown in Figure 3.7(b) and 3.7(d). As can also be seen in Figure 3.8(b) and Figure 3.8(d), the initial decay was much faster for the Pt/BP2000 catalyst than for the Pt/XC72 (at the 900^{th} cycle, a 62% mass activity loss for Pt/XC72, and a 97.6% loss for Pt/BP2000), which confirms the conclusion, again, that Pt/BP2000 corrodes more easily than Pt/XC72.

From the study of the TEM images of the two catalysts (Figure 3.9 and Figure 3.10), different corrosion processes for different carbon supports were suggested. The TEM images and the Pt particle size distribution of Pt/XC72 before and after 1800 consecutive cycles were shown in Figure 3.9(a) - Figure 3.9(c) respectively. As can be seen in Figure 3.9(a) and 3.9(b), the micrograph of the homemade Pt/XC72 sample before and after 1800 consecutive ADT cycles shows that the change in morphology and size of the XC72 sphere was almost negligible, comparing the fresh Pt/XC72 (Figure 3.9(a)) with the cycled Pt/XC72 (Figure 3.9(b)). However, it can be clearly seen that the center of the carbon black it can be clearly seen that the center of the carbon black it can be clearly seen that the center of the carbon black particle became brighter (as shown by the arrow pointing in Figure 3.9(b)) than the rest of the particle. Comparing that with the micrograph of a fresh Pt/XC72 in Figure 3.9(a), it appears that a hole began to emerge after 1800 consecutive cycles, indicating that the center of the Pt/XC72 corrodes more easily. This corrosion process resulted in the slow decrease of the ECSA and the mass activity before 900 cycles because the corrosion in the center may have had little effect on the Pt nanoparticles, which sat on the carbon surface at the very beginning.

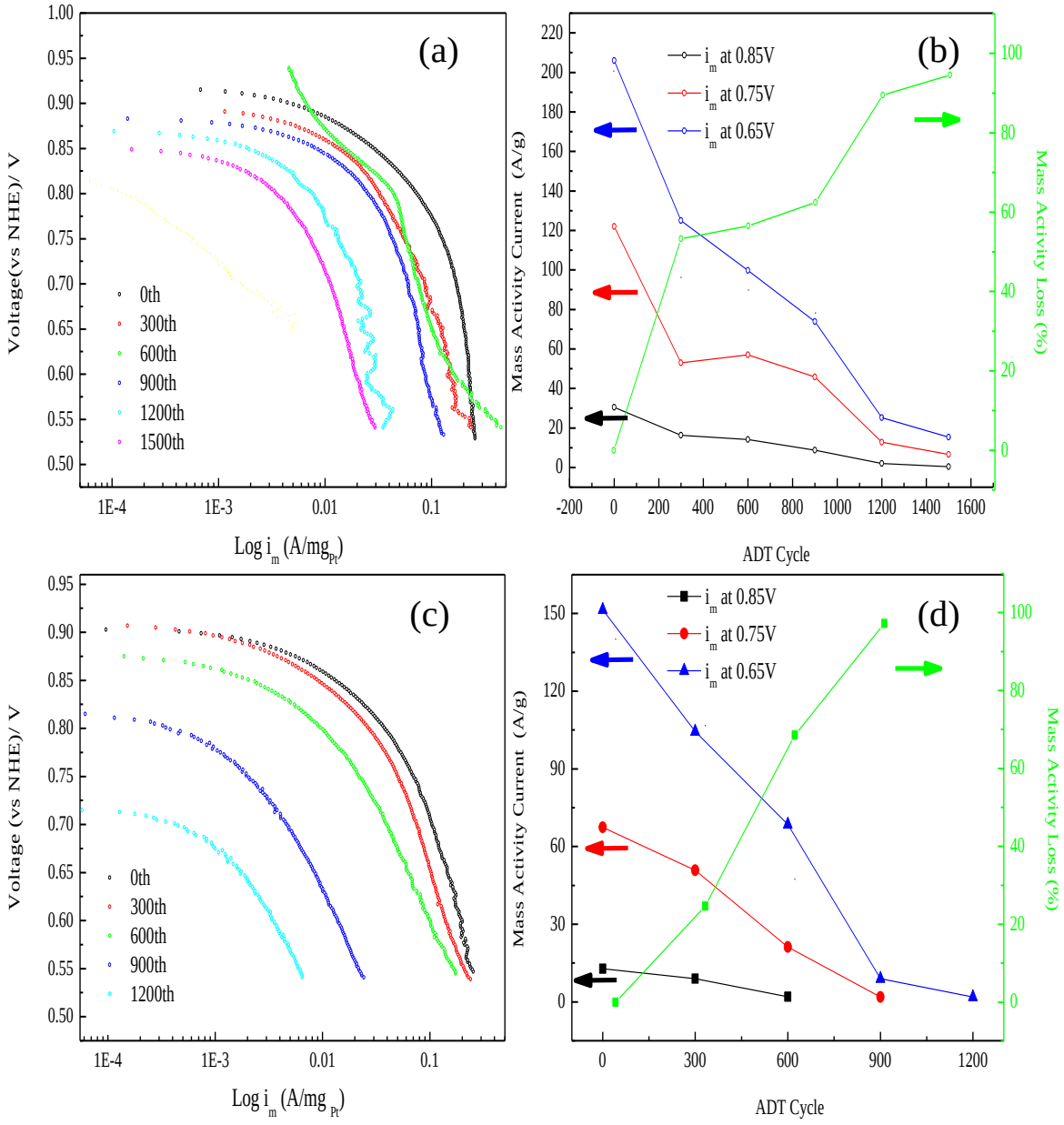

Figure 3.8 Polarization curves, mass activity current densities at 0.85, 0.75, and 0.65V (vs. NHE) and mass activity current density losses as a function of cycle after every consecutive 300 cycles for the (a) and (b) Pt/XC72, (c) and (d) Pt/BP2000

The particle size distribution of the platinum nanoparticles is shown in Figure 3.9(c) and is based on more than 200 particles analyzed using the software Image J. The mean particle size was obtained by using a weighted average based on the distribution data. It

was found that the Pt particle size increased from 3.32 to 4.27 nm (mean particles size) after 1800 continuous ADT cycles in the RDE system, accounting for a 28% loss in Pt surface area. The observed increase in the Pt particle size is probably due to the particle migration mechanism [74], which is explained by the migration and aggregation of platinum particles to form larger particles. H ́ector et al. [75] reported that the Pt catalyst average particle size after 1100 consecutive ADT cycles (from -0.03 to 1.24 V versus NHE in 0.3 M H_2SO_4 purged with N_2 at room temperature at a sweep rate of 5 mV s^{-1}) increased from 2.86 nm to 6.92 nm.

The TEM micrographs of Pt/BP 2000 are shown in Figure 3.10(a) and 3.10(b). It can be clearly seen that the corrosion feature of Pt/BP 2000 was different from that of the Pt/XC72 samples. Compared with the fresh Pt/BP2000 (Figure 3.10(a)), it can be seen that there were fewer spheres like the carbon particles because the boundary of the BP2000 became relatively obscure after 1800 cycles. Compared with Pt/XC72, it can be concluded that the carbon corrosion on Pt/BP2000 prefers to occur on the surface; therefore, it will facilitate the aggregation of Pt particles (a 1.56 nm increase for Pt/BP2000, but a 0.95 nm increase for Pt/XC72) by weakening or even breaking the interaction/bones between the Pt and the carbon surface and causing the migration and dissolution of the Pt particles. This is the reason why the ECSA, the mass activity, and the reason why the ECSA, the mass activity, and the DLC of Pt/BP2000 decreased more rapidly from the very beginning than those of the Pt/XC72. The particle size distribution of the Pt/BP2000 catalyst (Figure 3.10(c)) showed an increase of mean particle size from 3.7 nm to 5.26 nm, accounting for about a 39.6% Pt loss. After 1800 cycles, the increase in the particle size of the Pt catalysts was much bigger than that of the Pt/XC72, which is consistent with the decay of the ECSA and the mass activity results from both catalysts. Therefore, it could be convinced that the corrosion resistance of Pt/XC72 is much higher than Pt/BP2000, which just agrees with the results from ECSA changes from RDE experiment. It could be convinced that the corrosion resistance of Pt/XC72 is much higher than Pt/BP2000. It could be convinced that the corrosion resistance of Pt/XC72 is much higher than Pt/BP2000.

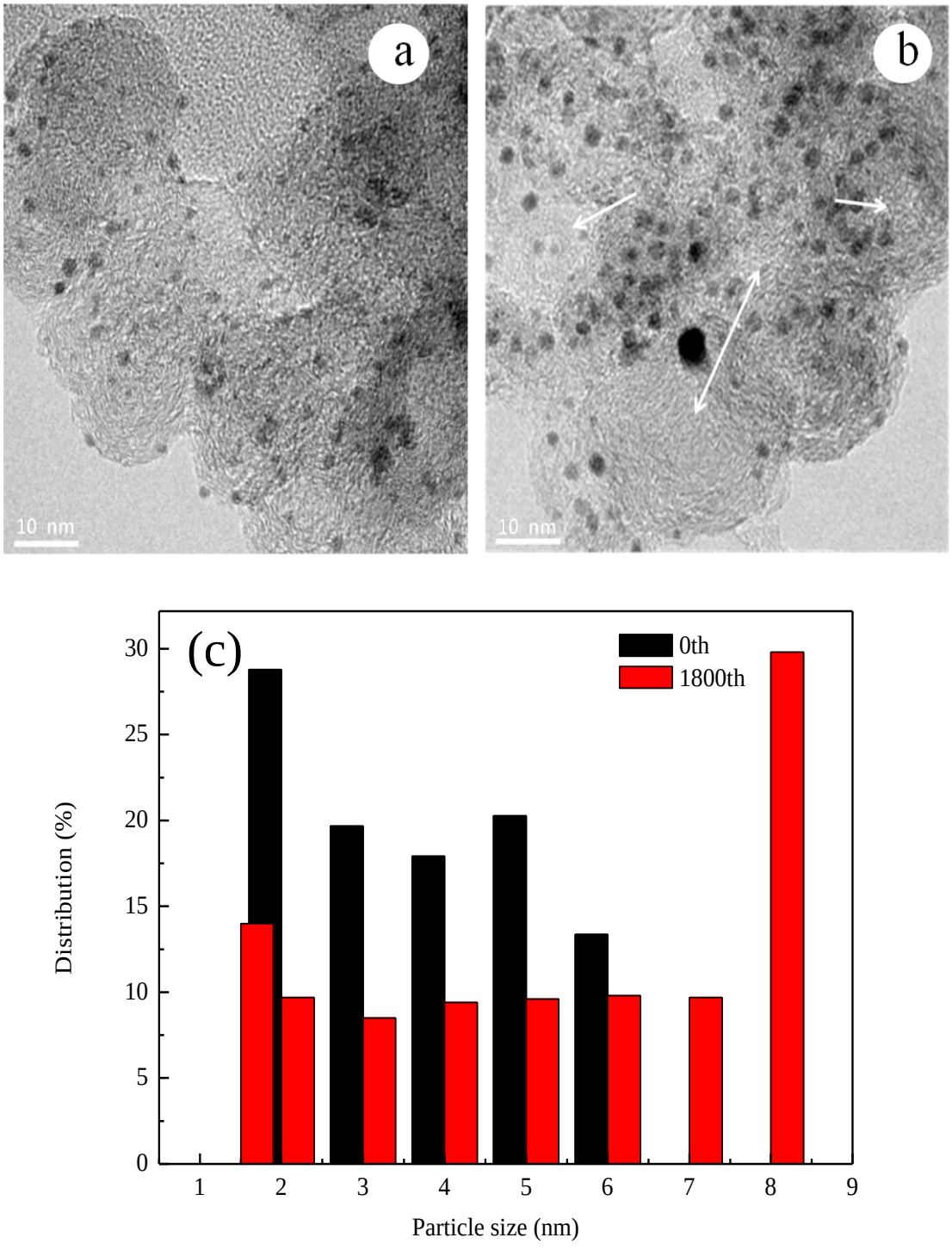

Figure 3.9 (a) and (b) TEM images of Pt/XC72 before and after consecutive ADT cycling, and (c) Pt particle size distribution before and after ADT

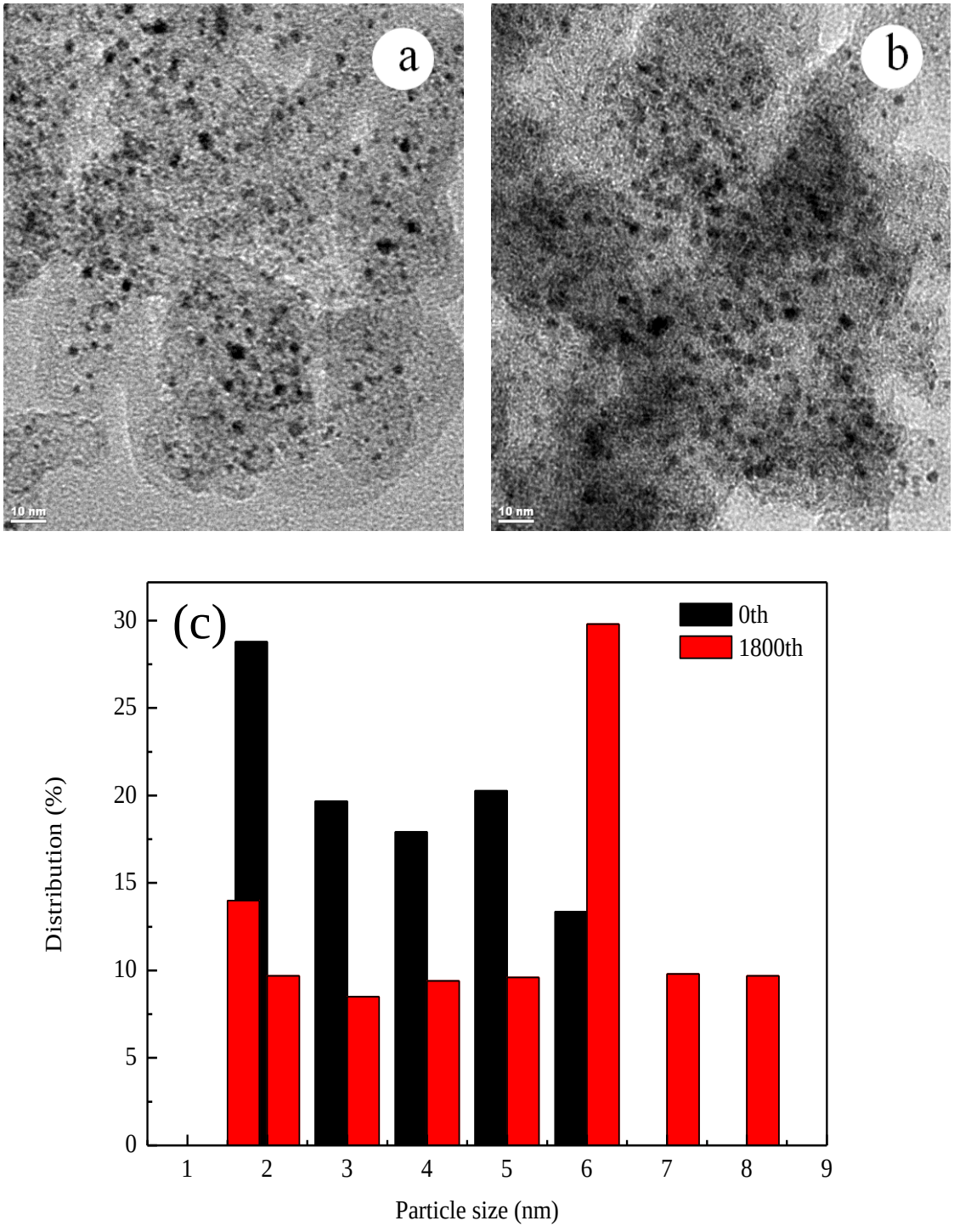

Figure 3.10 (a) and (b) TEM images of Pt/BP2000 before and after consecutive ADT cycling, and (c) Pt particle size distribution before and after ADT

3.3.3 Steam Etching Results

Investigation of the different carbon support corrosion processes in a membrane electrode assembly (MEA) of PEFCs is difficult because several parallel degradation processes are occurring (degradation of Pt and alloy catalyst nanoparticles, ionomer degradation, membrane degradation, and carbon corrosion). Detailed morphology changes of carbon supports with Pt nanoparticles are difficult to analyze due to the complexity of the PEFC degradation. The steam etching approach was used in our study because there is always a water film either inside the Nafion ionomer network or directly on the carbon surface during PEFC operation. The carbon blacks that come into contact with high temperature steam are then subjected to accelerated corrosion, which reveals the morphologic changes. This will help to illustrate the effects of different carbon supports on the corrosion behavior.

A steam etching experiment of XC72 and BP2000 was carried out to help confirm and understand these carbon black corrosion processes concluded from the RDE experiment.

The weight loss and the calculated full width at half maximum of the diffraction peak of carbon black samples are summarized in Table 3.2. For both XC72 and BP2000, the weight loss increases with the steam etching temperatures and times. Compared with XC72 samples, the BP2000 carbon blacks show a larger weight loss than the XC72 samples at the same temperature and etching time. The weight loss of the XC1000-3 is 67.12%, while the weight loss BP1000-1 is 100%. In the experimental observation, all BP2000 samples were completely gone after 1 hour of steam etching at 1000 ℃. The weight loss of carbon blacks after steam etching is a direct indication of carbon black corrosion: the higher the weight loss, the greater the corrosion. The difference in the weight loss of XC72 and BP2000 suggests that these two carbon blacks may have different corrosion processes, which could be associated with their chemical and morphologic structure (i.e. degree of graphitization, particle size, surface area, and pore structure, etc.). The major difference between XC72 and BP2000 is their surface area,

254 m^2/g *vs*. 1500 m^2/g (XC72 *vs.* BP2000). Since the steam etching is a surface reaction, it can be hypothesized that the higher weight loss of BP2000 samples in comparison with the XC72 samples under the same etching conditions is attributed to the higher surface area of BP2000.

Table 3.2 Weight loss and crystal properties of the samples

Sample	Temperature (℃)	Time (h)	Weight loss (%)	[a]Average particle size (nm)	[b]β_{002}	[c]β_{10}
XC-72				48.50	6.45	5.39
XC800-1	800	1	15.52	49.21	4.21	3.65
XC800-3	800	3	28.43	49.43	5.01	2.86
XC1000-1	1000	1	28.9	49.59	5.41	4.97
XC1000-3	1000	3	67.12	48.71	9.76	6.77
BP2000				32.20	9.01	4.42
BP800-1	800	1	32.54	19.75	11.36	5.74
BP800-3	800	3	54.82	18.38	15.23	
BP1000-1	1000	1	100			

a: Average particle size of five carbon black particles in TEM micrograph.
b, c: The full width at half maximum of the diffraction peak.

TEM micrographs of XC72 samples are shown in Figure 3.11. A fresh XC72 carbon black particle is shown in Figure 3.11(a) and (b). The characteristic feature of the XC72 particle is that the graphite layer planes are concentrically parallel to each other toward the center, which is similar to the pattern of a fingerprint. Close examination of Figure 3.11(b) reveals that the graphite layer plane is concentrically parallel but in a more disorderly arrangement. This feature matches the carbon black microstructure model proposed by Heckman et al. Figure 3.11(e) is the micrograph of XC72 carbon black sample after three hours of etching. It can be clearly seen that the center of the carbon black particle became brighter (as the arrow points to in Figure 3.11(e)) than the rest of particle, consistent with the interpretation that the particle center has experienced greater

mass loss than the rest of the particle. Comparing that with the micrograph of a fresh XC72 in Figure 3.11(a) and 3.11(b), it appears that a hole begins to emerge after steam etching for three hours. It can be seen in Figure 3.11(f), which is a higher magnification micrograph of Figure 3.11(e) that the center of the XC72 particle was significantly corroded, and the carbon layer planes are more disorderly when compared with Figure 3.11(b). In addition, in Figure 3.11(f), some carbon layer planes on the outermost surface of the carbon black sphere became cracked. However, through a comparison of micrograph Figure 3.11(a), (c), and (e), it can be clearly seen that the carbon black particle size remains the same after steam etching, even for three hours at 1000 ^{o}C.

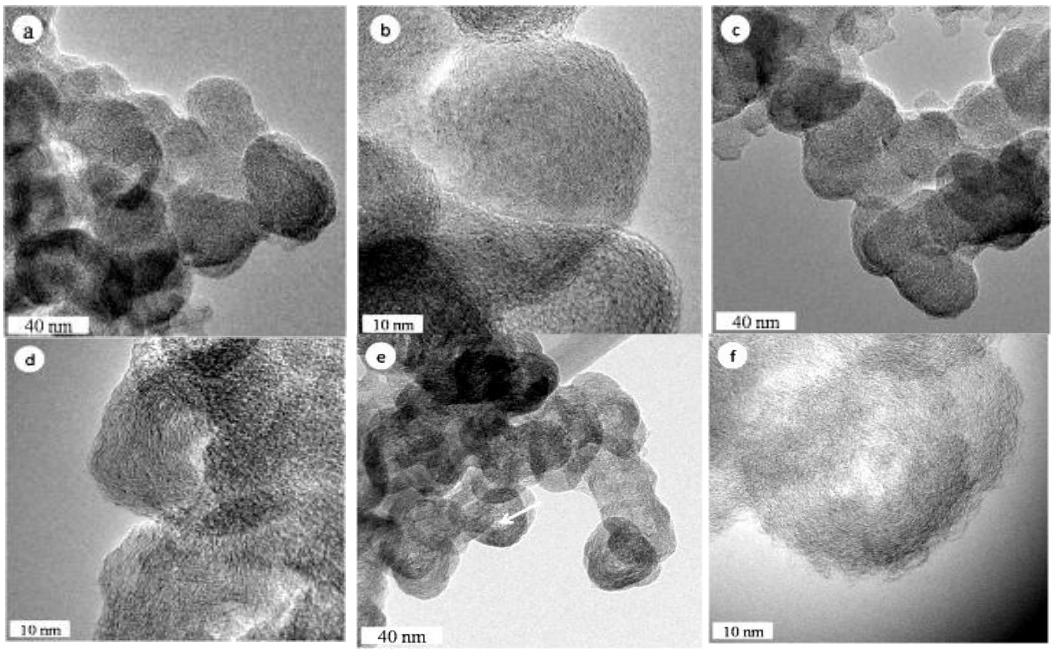

Figure 3.11 TEM micrographs of the steam etched samples. (a) and (b):XC72, (c) and (d):XC721000-1, (e) and (f):XC721000-3, (b), (d) and (e) are the higher magnification micrographs of (a), (c) and (d)

The micrographs of XC72 etched for 1 hour are shown in Figure 3.11(c) and (e), It can be seen that no significant morphologic changes occur in comparison with XC72 etched for 3 hours under 1000 ^{o}C, but the surface becomes some smooth after etching. However, from the Table 3.3, it can be seen that the weight loss after 1 hour of etching is

28.9%. Combining the TEM micrographs and the weight loss in table 3.2, it is clear that that major corrosion occurred at the center of the XC72 particle with some minor corrosion on the surface of the carbon particle to remove some amorphous structured carbon blacks filaments, which will be explained in detail by the XRD spectra.

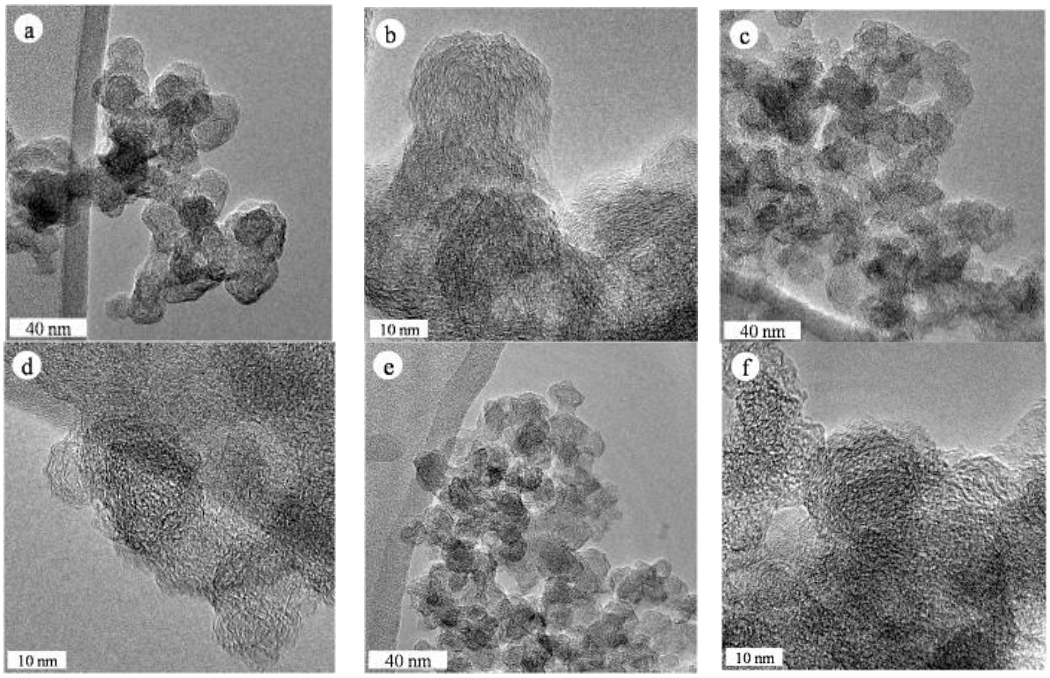

Figure 3.12 TEM micrographs of steam etched samples.
(a) and (b) BP2000, (c) and (d) BP800-1, (e) and (f) BP800-3

The TEM micrographs of BP2000 are shown in Figure 3.12. It can be clearly seen that the corrosion feature of BP2000 is different from that of the XC72 samples. The significant difference between the fresh XC72 and BP2000 is that the BP2000 graphite layer planes are not as concentrically parallel to each other toward the center as the XC72 counterpart. The disorderly portion found in a BP2000 particle is far more prevalent than that in an XC72 particle (compare Figure 3.11(a) and (b) with Figure 3.12(a) and (b)). No bright features are apparent in the center of the BP2000 particles after etching for 3 hours at 800 °C (in Figure 3.12), although the weight loss of the BP800-3 is 54.82% (Table 3.2). Through comparison of Figure 3.12(a), (c), (e) and Table 3.2, it can be seen that the particle size significantly decreases with the etching time. The particle size change can

also be seen from the SEM micrographs in Figure 3.13 and from the data present in Table 3.2. The weigh loss of BP1000-1 is 100%. Compared to XC72 carbon blacks, BP2000 carbon blacks show a larger weight loss under the same conditions. Therefore, it can be concluded that BP2000 is more easily corroded than XC72 under equivalent conditions. The lower corrosion resistance of BP2000 can be attributed to two factors: 1) the surface area of the BP2000, which is 1500 m^2/g, much larger than that of the XC72 254 m^2/g, and 2) the particle size of BP2000, which is smaller than that of the XC72 (see Figure 3.11(a) and 3.12(a)). In addition, the microstructure of BP2000 is less ordered and the carbon layer planes are less uniform in structure, unlike XC-72, which has a more dense carbon layer plane structure as suggested by the values of full width at half maximum in Table 3.2, and a more ordered structure in the particle center.

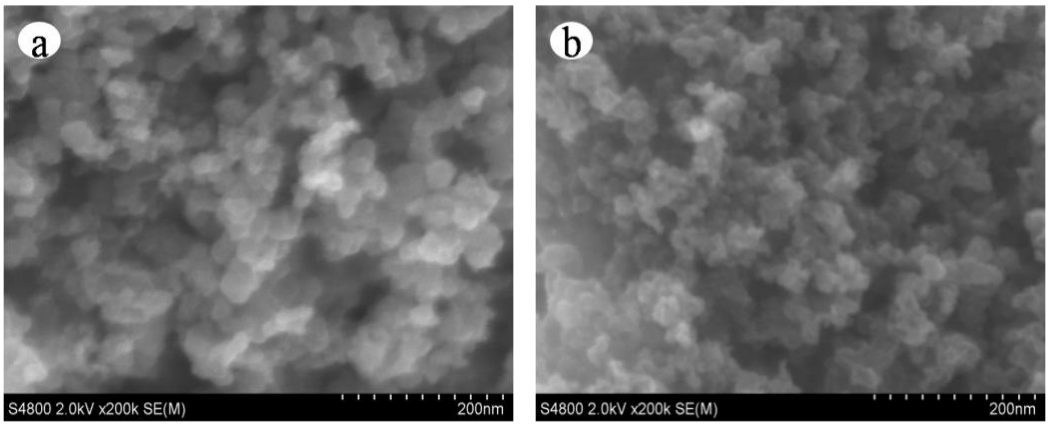

Figure 3.13 SEM micrographs of the samples. (a) BP2000, (b) BP800-3

The different corrosion processes of XC72 and BP2000 carbon blacks originate from their differences in the structure of the graphitic carbon layers. XC72 has a more dense graphitic structure at the surface (compare the $\beta_{002}$and β_{10} in Table 3.2 for XC72 and BP2000 and Figure 3.11(a) and (b) with Figure 3.12 (a) and (b)) and a more disordered structure in the particle center, thus the corrosion process begins from the center rather than from the surface. That the corrosion mainly occurs at the particle center is suggested by the fact that particle size remains almost the same, even after 3 hours of

etching. But for BP2000, the carbon layer planes structure is uniform and no significant difference appears between the surface graphitic layers and center graphitic layers. Therefore, the BP2000 corrosion begins on the surface, and particle size decreases with etching time.

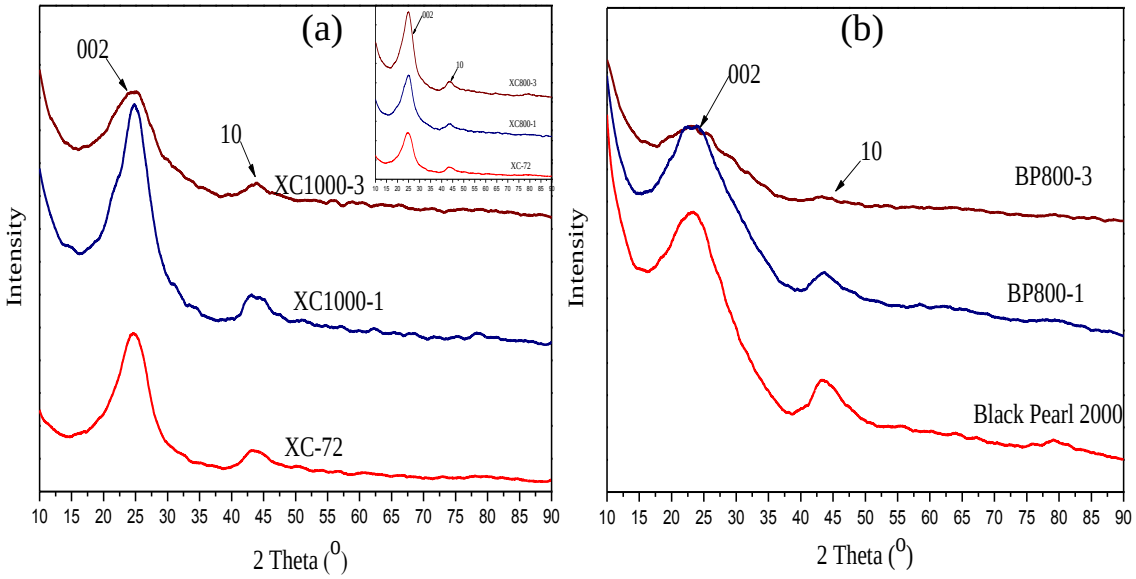

Figure 3.14 (a) XRD spectra of XC72 and XC72 derived samples,
(b) XRD spectra of BP2000 and BP2000 derived samples

The x-ray diffraction patterns for the XC72 and BP2000 carbon black samples are shown in Figure 3.14(a) and (b). For graphite, the 002 peak is expected at around 26.38°, the 100 peak at 42.22°, and the 101 peak at 44.39°. For the amorphous carbon black samples, a broad peak corresponding to the 002 reflection is shifted downwards and is seen around 22.5°. The shift of the 002 reflection to lower values leads to the larger d_{002} suggesting a more amorphous phase in the XC72 carbon blacks. Furthermore, for turbostratic two-dimensional ordering, the 100 and 101 peaks merge into a broad 10 peak around 43°. From Figure 3.14(a), it can be seen that the XC72 steam etched carbon blacks at 800 °C and the 002 and 10 peaks became sharper as the etching time increased. The crystallite size also increased because a broader peak is usually associated with a smaller crystallite size. When the etching temperature increased to 1000 °C, however, the

002 and 10 peaks of the samples initially became sharper and then became broad again. The crystallites size of these samples also increased initially and then deceased as the etching time increased. For the BP2000 samples, the 002 and 10 peaks became broader with the increase in etching time. The crystallites size of these samples also decreased.

Carbon black is one of the classes of carbon materials that have a form different from the forms of diamond, coke, charcoal and graphite. Carbon blacks consist mostly of spherical and ellipsoidal particles. These particles have both amorphous and crystalline substructures. They may be visualized as being composed of more or less oriented graphitic layer planes. They exhibit various extents of electrical conductance because of their predominant graphite-like structures. Then, the crystalline substructures were corroded in the steam etching process. This is probably the reason that the 002 and 10 peaks of the XC72 samples initially became sharper before becoming broad again. As for the BP2000 samples, the corrosion process begins on the particle surface because of its high surface area, small particle size, and more ordered carbon layer plane structure. This is probably the reason the 002 and 10 peaks became broader as the etching time increased.

3.4 Conclusion

An accelerated durability test utilizing an RDE system was used to study the corrosion of XC72 and BP2000 as catalyst carbon supports. The observed corrosion processes for the different catalysts started from the center of the particle for the Pt/XC72 and started on the surface of the particle for Pt/BP2000. The decay in performance of the catalysts can be explained by two key reasons: particle migration and carbon corrosion. The carbon corrosion affected the performance of the catalyst more before 900 cycles in the Pt/BP2000 than in the Pt/XC72. The results of the ECSA and ORR current measurement indicate higher corrosion of the Pt/BP2000 than the Pt/XC72 after 1800 ADT cycles. The steam etching experiment confirmed the corrosion process observed in the RDE testing for both catalysts.

4. ENHANCED CATALYTIC PERFORMANCE OF PLANTINUM /CARBON CATALYSTS USING STEAM ETCHING CARBON BLACKS AS SUPPORT

4.1 Introduction

One strategy to reduce the fuel cell performance degradation from carbon corrosion is to use the more stable carbons (than carbon blacks) as catalyst supports [76]. For example, it has been proposed that carbon materials with more graphite component are more stable, such materials are graphite carbon nanofibers [77], carbon nanotubes [78], ordered uniform porous carbon networks [79], graphenes [80] and so on. These carbon materials have been shown to be more corrosion resistant than carbon blacks, but the cost of manufacturing is still a significant concern.

Following the discovery of fullerenes and nanotubes, multiple new carbon structures have been reported by different research groups, including carbon onions [81], helical nanotubes [82], nanocones [83], carbon nanohorns, microtrees [84], nanotube caps [85], carbon nanorods [86], as well as others. However, the promising carbon support that can replace Vulcan XC72 is not discovered yet and the carbon blacks are still the best catalyst support so far in terms of the dispersion of Pt and Pt alloy catalyst nanoparticles, density, hydrophilicity, and electronic conductivity.

It reported that without surface modification, most of carbon nanomaterials lack sufficient binding sites for anchoring precursors metal ions or metal nanoparticles, which usually leads to poor dispersion and aggregation of metal nanoparticles, especially at high loading conditions. So there are a lot of work reported to introduce functional groups on the carbon surface and increase the catalyst nanoparticles dispersion [87 - 89]. In order to increase the performance of the PFFCs, the carbon blacks were heat treated under

increase the performance of the PFFCs, the carbon blacks were heat treated under high temperatures and used as the catalysts support were reported by several groups [90 - 91].

The promising carbon support that can replace Vulcan XC72 is not discovered yet and the carbon blacks are still the best catalyst support so far in terms of the dispersion of Pt and Pt alloy catalyst nanoparticles, density, hydrophilicity, and electronic conductivity. According to the carbon corrosion research in last chapter, a new approach of making high corrosion catalyst was developed. In this part, the XC72 carbon blacks were steam etched under different conditions and used as the catalyst supports for PEFCs. The goal is to utilize the steam etching technique to remove the amorphous components of carbon blacks to increase the degree of graphitization. With higher graphitization, the carbon black support will have stronger corrosion resistance. The steam etching can also create more functional groups on carbon surface which in turn, will help to improve the Pt nano particle dispersion. It is found that the carbon blacks morphologies and crystallite structures significantly changed as the etching time increased. The ECSA and ORR of the steam etched carbon blacks were better than that of the commercial catalysts with the same Pt loading.

4.2 Experimental Section

4.2.1 Preparation of the Steam Etched XC72 Catalyst

Carbon blacks Vulcan XC72 with a surface area 254 m^2/g from Cabot (Billerica, MA) were used as the precursors. A furnace with a gas inlet and an exit was used for the steam etching experiment. The aggregates of these carbon black powders were milled before etching experiments. The milled carbon black powders were placed into the tube furnace and then were purged with nitrogen while the temperature was increased through programmed heating at a heating rate 5 ^oC/min. The steam was introduced into the furnace when the furnace reached the desired temperatures and the steam continued flowing through the furnace for a certain length of time. The flow rate of steam is 0.5

cm^3/min (water) and the flow rate is the same in all experiments. The steam etched products were labeled as XC – x – y, where x represents the steam etched temperature and y is the steam etched time.

The catalyst was prepared by EG (Ethylene glycol) method [92]. For the catalyst preparation, 100 mg of the nanoscale graphite obtained by 2 hours etching were suspended in 20 ml of ethylene glycol solution and stirred with ultrasonic treatment for 20 mins, then 1.5 mL of hexachloroplatinic acid EG solution (15mg Pt/ml EG) was added to the solution dropwise also under mechanically stirred conditions for 4h. NaOH (0.01M in EG solution) was added to adjust the pH of the solution to above 13, then the solution was heated at 140 ^oC for 3 hours to ensure that Pt was completely reduced, the entire EG solution has a DI water content of less 5 vol %. Refluxing systems were used to keep water in the synthesis system. The process is to remove organic byproducts. The solid was separated from the solution by centrifugation and the products were washed by DI water for 5 times, dried at 70 ^oC for 8 hours. Catalyst with 20% Pt loading on nano-scale graphite was obtained.

4.2.2 Characterization of Steam Ething XC72 Based Catalyst

The mass of the carbon blacks was measured before and after the steam etching experiment to determine the weight loss of the carbon blacks in the steam etching process. The crystal structures of the fresh and etched carbon blacks were analyzed using powder X-ray (Rigaku Dmax-B, Japan) diffraction (XRD). The XRD diffractometer utilized Cu Kα radiation (40 kV and 30 mA) and the data were collected as continuous scans, with a step of 0.02° (2θ) and a scanning rate of 2° (2θ) / min between 10 - 90° (2θ).

The morphologies of the steam etched samples were examined using Philip Tecnai 20 transmission electron microscope (TEM). Also, the particle size distributions are obtained by analyzing the overview TEM images (at least 200 particles are involved) by Image J.

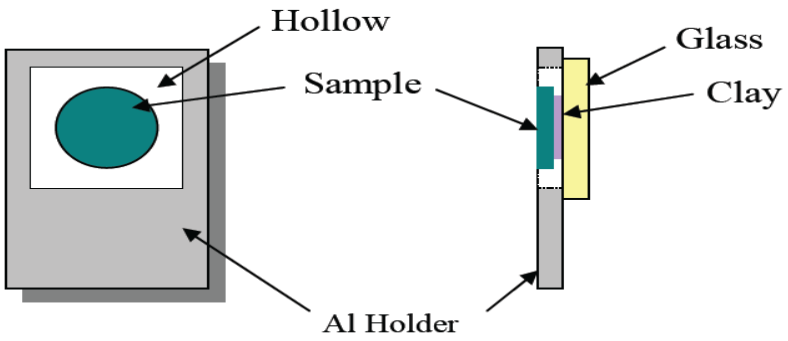

Figure 4.1 The XRD holder for catalyst

The surface chemistry of the raw carbon blacks and the steam etched carbon blacks samples were analyzed using a Kratos AXIS Ultra X-ray photoelectron spectrometer (XPS). The spectrometer is monochromatic Al Ka X-ray source. An electron flood gun for charge neutralization and hemispherical analyzer with 8 multichannel photomultiplier detectors was employed for analysis. Area of analysis is 700 x 300 microns in size.

4.2.3 MEA Preparation and Electrochemical Measurements

The LANL decal process was used to prepare all MEAs used in this study. Catalyst inks were prepared by mixing a carbon-supported catalyst (commercial Pt/XC72 and Pt/XC721000-1h) with glycerol, 5% Nafion® solution, and 1.0 M tetrabutylammonium hydroxide (TBAOH). The inks were stirred overnight to form a well-mixed dispersion, which was then painted onto a decal surface of fiberglass coated with Teflon® by Dr. Blade system. The decal was heated in an oven at 140 °C for 30 minutes. The catalyst loading was 0.20 mg Pt/cm^2 (nominal) for this study. Anode and cathode catalyst decals were then hot-pressed onto either side of a sodium-form Nafion® NR212 membrane at 454 kg/cm^2 and 200 °C for 5 minutes. After hot pressing, the decals were peeled off, forming a three-layer MEA (with 5 cm^2 geometric active area), which was boiled for two hours in 0.5 M sulfuric acid followed by two additional hours of boiling in DI water. Finally, the MEA was dried on a heated vacuum table at 60 °C for 30 minutes.

4.2.4 Electrochemical Measurements

The electrochemical measurements for the performance of steam etching XC72 based catalyst are the same as mentioned in last chapter.

4.2.5 Carbon Corrosion Testing

For 5 cm^2 MEA, the cathode side was fed with 559E-6 standard cubic meters per minute (scmm) of air (corresponding to an O_2 stoichiometric ratio of 6.74 at 1.0 A/cm^2), and the anode side was fed with 200E-6 scmm of pure hydrogen (corresponding to a H_2 stoichiometric ratio of 5.74 at 1.0 A/cm^2). Both air and hydrogen were pre-humidified at temperatures of 80 °C (water content of ~100% relative humidity) and 105 °C (water content >> 100% relative humidity), respectively. Gas pressures were set to 30 psig (2.07E05 Pa, atmospheric pressure 77.3 kPa) using backpressure regulation and the cell operating temperature was set to 80 °C.

The corrosion protocol is showed below:

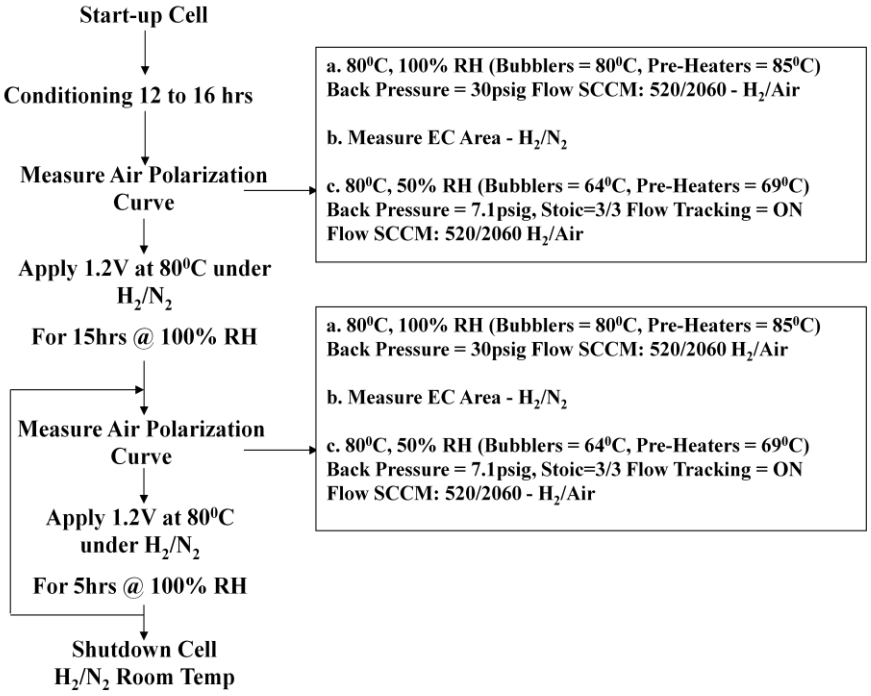

Figure 4.2 The corrosion Protocol for MEA

4.3 Result and Discussion

4.3.1 XRD and High Resolution TEM Images of Steam Etching Pt/XC72 Catalyst

TEM micrographs and XRD patterns of Pt/C catalysts were reported in Figure 4.3 and Figure 4.4. It was clearly observed that the fine particles prepared by EG method were distributed on the surface of the carbon blacks. A homogeneous distribution of platinum particles is important for the preparing a highly catalytic electrocatalyst [93]. It can be seen from Figure 4.3(a) that the distribution of ultrafine Pt particles on the XC72 based catalyst is not uniform compared with the steam etched carbon samples, some Pt particles more densely distributed on specific areas. However after steam etching, the Pt particles distributed more uniformly on the surface of carbon blacks as can be seen from Figure 4.3(b) and (c). In addition to these ultrafine particles, there are still some much larger Pt particles appeared y in Figure 4.3(a) and (d). The Pt nanoscale particles distribution is closely related to the carbon supports, in order to get the more catalytic catalysts the carbon supports should have uniformly dispersed active sites for Pt precursor. For steam etched samples there will be more active sites for Pt precursor. This will be discussed in detail in the XPS data.

Power XRD analysis has been carried out in the fresh catalysts in order to evaluate the average particles size of the Pt nanoparticles s formed on the carbon blacks. Figure 4.4 presents XRD curves of catalysts Pt/XC72, Pt/XC721000-1h, Pt/XC721000-3h. The diffraction peaks at 2θ values of about 39.8, 46.2 and 81.4 are ascribed to the facets (111), (200), (220), and (311) characteristic of face centered cubic crystalline Pt. The average size of Pt nanoparticles was calculated from the Pt(220) peak using the Debye-Scherrer equation to be 3.9, 3.2 and 3.0 nm for Pt/XC72, Pt/XC721000-1h, Pt/XC721000-3h, respectively. The average Pt nanopartices size on the steam etched carbon blacks was reduced compared with that of pristine carbon blacks. For Pt/XC72, Pt/XC721000-1h, Pt/XC721000-3h, respectively, the average Pt nanopartices size on the steam etched carbon blacks was related to their carbon blacks.

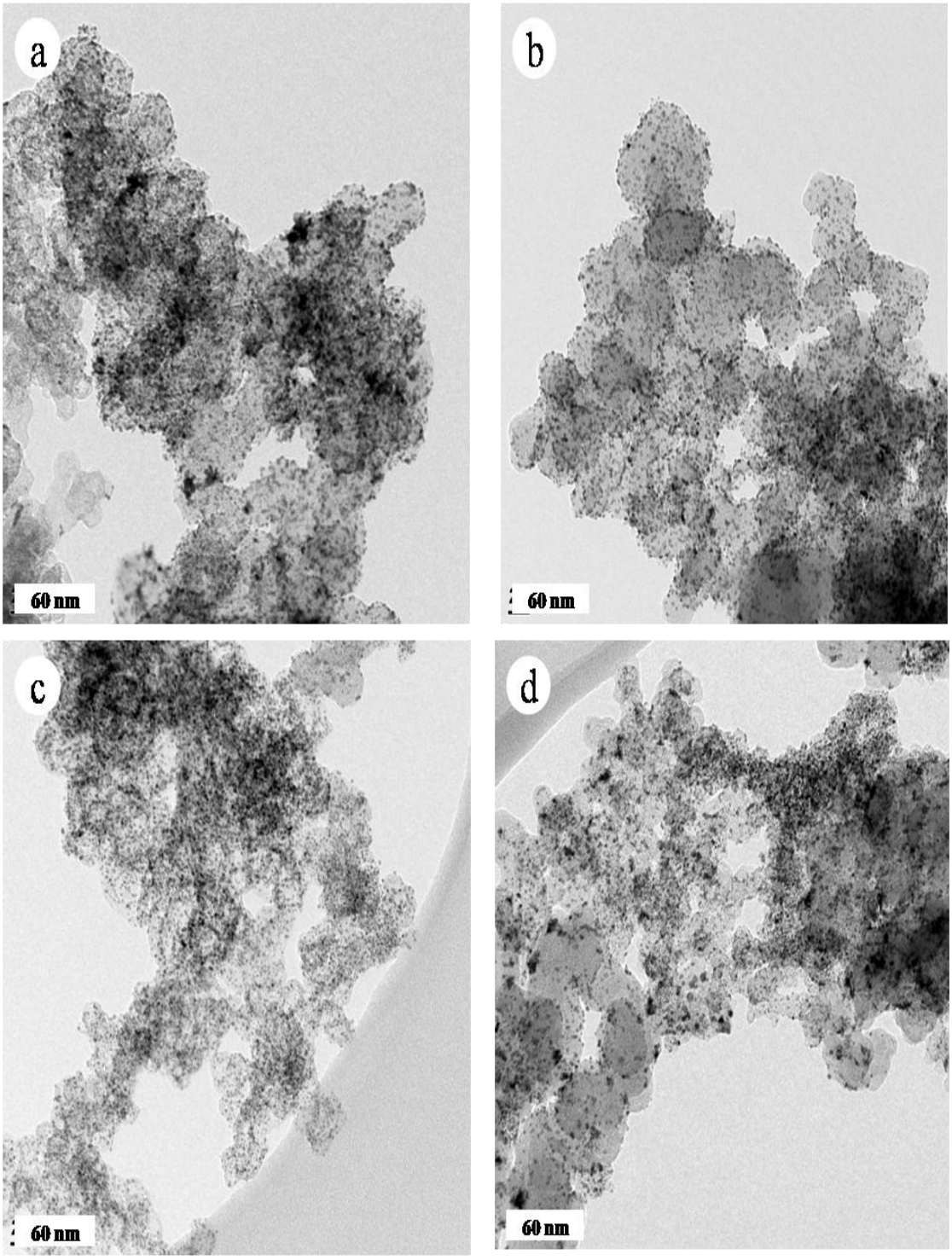

Figure 4.3 TEM micrographs of the steam etched carbon blacks based catalysts.
(a) Pt/XC72, (b)Pt/XC721000-1, (c) Pt/XC721000-3, (d) commercial Pt/XC72

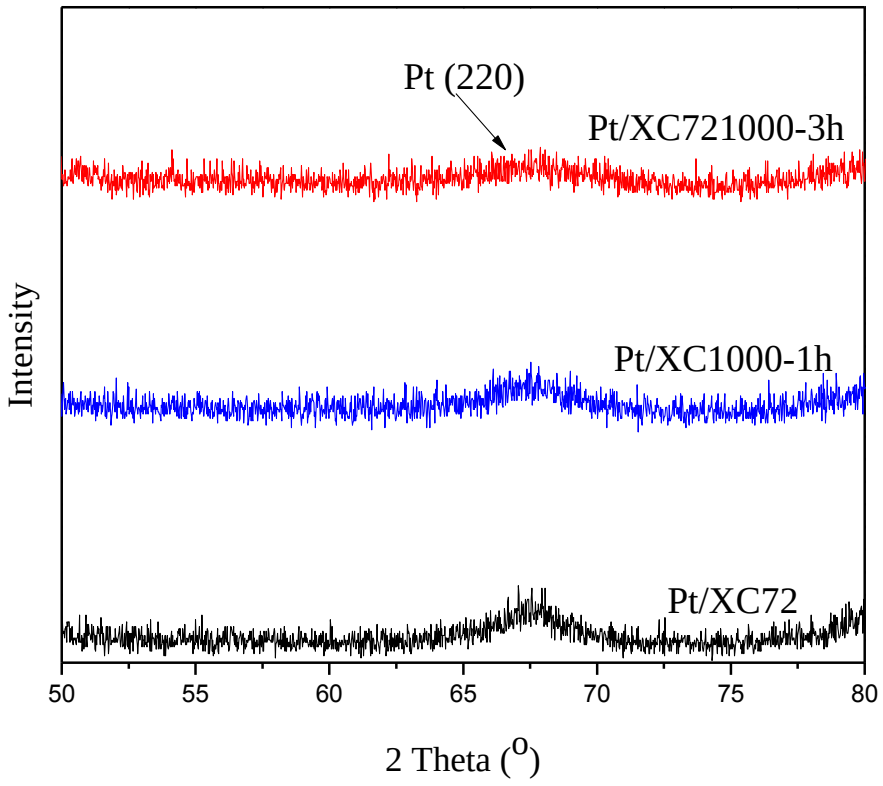

Figure 4.4 XRD spectra for Pt steam etched carbon blacks composite

4.3.2 XPS Results and Discussion of Steam Etching Pt/XC72 Catalyst

XPS results confirm the existence of hydroxyl C-OH (286.8 ± 0.2 ev), carbonyl C=O (287.5 ± 0.1 ev), and carboxyl O=C-OH (288.9 ± 0.2 ev) groups on the surface of both pristine and steam etched carbon blacks. The XPS results for pristine and steam etched carbon blacks are summarized in Table 5.1 obtained from Figure 4.5. Clearly, the percentage of C-C carbons in the carbon blacks was firstly decreased and then increased. The percentage of C=C carbons in pristine XC72 was 35.5%, after steam etching for 1h the percentage increased to be 48.3% and for XC721000-3h the percentage decreased to be 27%. As the etching time increase the crystallite structure of carbon blacks was firstly became better and then became worse. The percentage of C-O carbons after steam etching was increased for both XC721000-1h and XC721000-3h, and this may be responsible for the improved uniformity of Pt nano-particles on the carbon blacks surface.

.

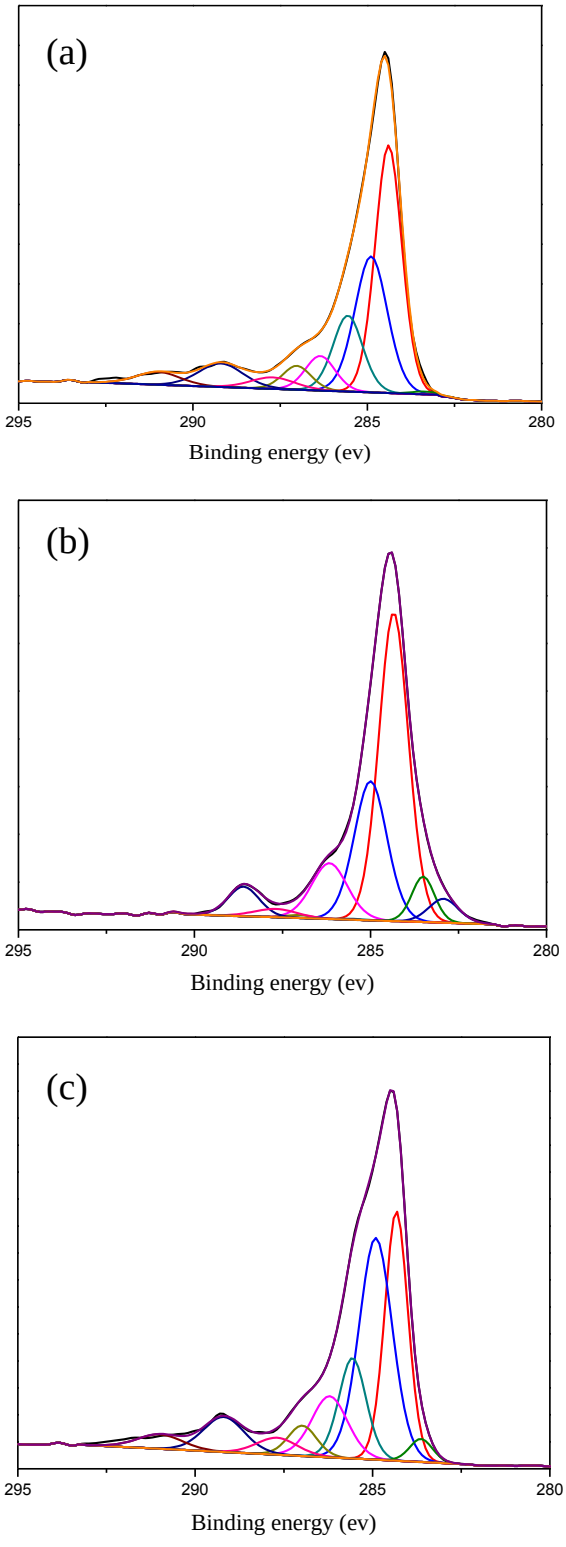

Figure 4.5 XPS spectra of the steam etched carbon black

Table 4.1 Comparison of XPS spectral components for pristine and steam etched carbon black

Sample	C=C	C-C	C-O	C-OH	C=O	COOH	Shake-up
XC72	35.3	26.9	7.3	4.3	2.0	6.3	2.5
XC721000-1h	48.3	24.3	10.6	0.4	1.9	4.9	0.1
XC721000-3h	27.0	36.1	10.2	3.3	3.2	5.7	2.6

4.3.3 Electrochemical Performance of Steam Etching Pt/XC72 Catalyst

A Rotating Disk Electrode (RDE) approach under simulated PEFC conditions was employed to characterize the electrochemical performance of the steam etching catalysts (by ethylene glycol method).

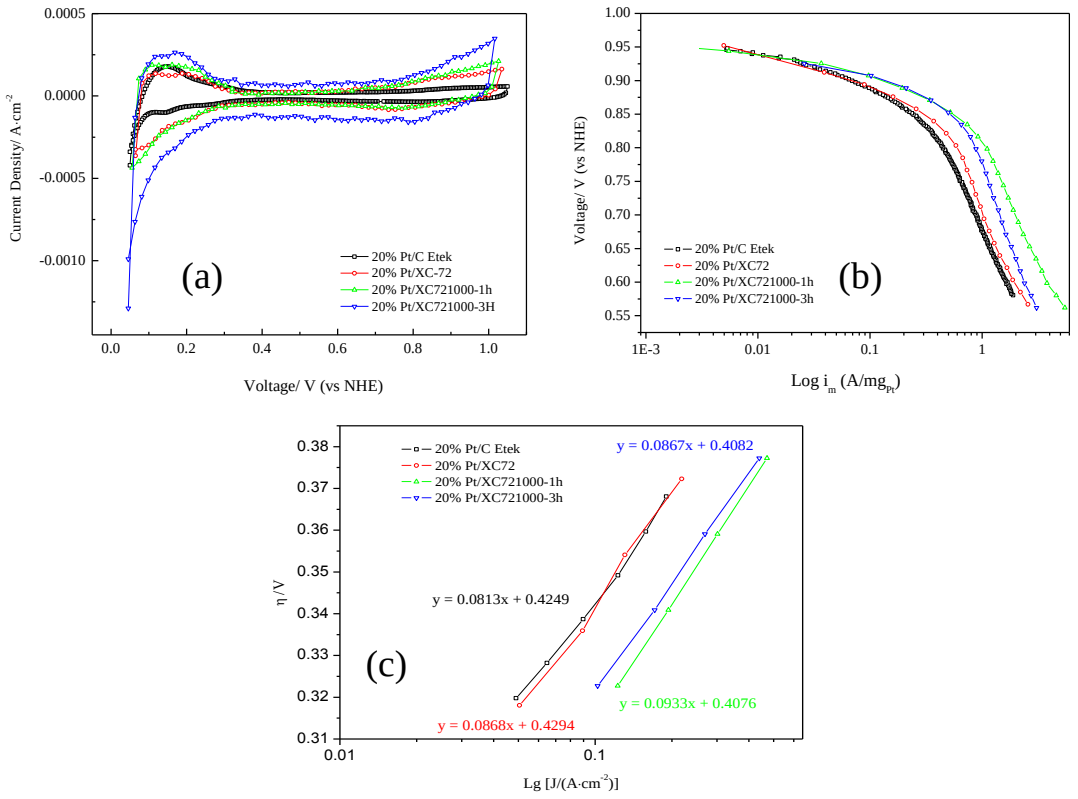

Figure 4.6 Cyclic voltammograms (a) Oxygen Reduction Reaction (b) and Tafel (c) curves for the prepared catalysts and the commercial catalysts

Figure 4.6 is the typical polarization curves, CV and Tafel curves for the 20% commercial catalysts and home-made steam etched carbon black supported catalysts. As could be seen in Figure 4.6(a), the electrochemical active surface areas (ECSA) of the home-made catalysts and the commercial catalyst were determined by CV measurements performed in 0.5 M H_2SO_4 solution. The ECSA was determined by integrating the H_{up} peak. The pair of peaks observed between 0.05 V and 0.30 V (*vs.* NHE) corresponded to the desorption–adsorption of hydrogen on the Pt surface after double-layer correction. The ECSA results are listed in Table 4.2. The catalysts with the carbon blacks after 1 hour and 3 hours steam etching have much bigger ECSA, which increased 26% and 21% more than that of without etching, which agrees with the Pt particle size in TEM and XRD results. As for the particle size of Pt, from TEM and XRD, it could be obtained that Pt/XC721000-3h < Pt/XC721000-1h < home-made Pt/XC72 < commercial Pt/XC72. It has been found that with the decrease of Pt size, the ECSA increases [29].

It is also noticed that, in Figure 4.6(a), the Double Layer Charging increased with steam etching time, suggesting a larger carbon support surface could be obtained by the steam etching process, which is also shown in BET results. The increase of carbon support surface might be one of the main reasons why Pt particle size decreased with the steam etching time.

Table 4.2 Electrochemical properties of the catalysts

	ORR (1600rpm, O_2, from -0.2V to 0.8V vs (Ag/AgCl))			
	i_m^* at 0.9V(A/mg)	i_m^* at 0.85V(A/mg)	i_m^* at 0.75V(A/mg)	Tafel (mV/dec)
Pt/XC72	1.13	2.06	5.74	86.6
Pt/XC721000-1h	1.30	3.85	30.25	93.3
Pt/XC721000-3h	1.30	3.45	12.45	86.7
Commercial	1.13	1.77	4.08	81.3

As shown in Figure 4.6(b), at high potentials (between 0.96 and 0.85 V versus NHE), the ORR is under the pure kinetically controlled region. The Tafel slopes, shown in Figure 4.6(c) and Table 4.2, are 81.3 mV/dec, 86.6 mV/dec, 93.3 and 86.7 mV/dec for commercial Pt/XC72, home-made Pt/XC72, Pt/XC721000-1h and Pt/XC721000-3h respectively. The differences suggested steam etching process could greatly affect the catalyst activity. The results showed that firstly, the catalyst activities for home-made catalyst were better than commercial catalyst. Secondly, the catalyst activity increased with the steam etching process time (the best catalytic activity was obtained by Pt/XC721000-1h), then decrease after steam etching 3 hours, which may be caused by change of carbon support (surface functional group) after longer steam etching process.

At media potentials, it is the mixing controlled region of diffusion and charge transfer. Again, the same trend was showed in this region. The mass activity of Pt/XC721000-1h and 3h increased 6.4 (4.3) times and 2.1 (1.2) times than the commercial Pt/XC72 (home-made Pt/XC72) at 0.75 V respectively, suggesting better catalyst structure was obtained after steam etching process. It can be clearly found that after steam etching, both the Pt/XC721000-1h and Pt/XC721000-3h have better Pt nano-particles dispersion and relatively smaller Pt particles size than commercial catalyst. This is the reason why steam etching catalysts have better ECSA and ORR than that of home-made (EG) and commercial Pt/XC72 samples. However, it was found that the ORR performance for Pt/XC721000-1h is better than that of Pt/XC1000-3h, which is different from the ECSA results. That might be caused by two main reasons. Firstly, in ORR process, which is different from HOR process (ECSA), there is an optimal Pt particle size for ORR, which is around 3 nm. It was shown in TEM and XRD results that the mean sizes of Pt on XC721000-1h and 3h were nm and nm. Therefore, the performance for Pt/XC721000-1h is better than that of Pt/XC721000-3h. Secondly, after 1h steam etching process, the best crystallite structure of carbon black support was obtained (from XPS results) after 1h steam etching process, while after 3h steam etching, this structure began to ruin, 67.12% carbon was lost. In other words, the conductivity of the Pt/XC721000-1h is higher than that of Pt/XC721000-3h, which might contribute to the better ORR

Pt/XC721000-3h, which might contribute to the better ORR performance by Pt/XC721000-1h than that of Pt/XC721000-3h.

From the XPS results, it can be seen that for the samples steam etched for 1h have better crystallite structure that other samples and this probably responsible for the 1h has the biggest the ORR. The XPS results show that the samples XC721000-3h has the worst crystallite structure and the carbon blacks were completely corroded and the samples XC721000-3h has the worst crystallite structure and the carbon blacks were completely corroded, after the 3 hours reaction with steam 67.12% of the carbon was lost. So this may probably be responsible for the worse electrochemical performance for Pt/XC721000-3h samples even with the biggest ECSA. For the electrocatalysis, not only facile mass transport of molecules within the carbon support but also its surface reactivity, electronic conductivity, ionic conductivity, and separation of electron-hole pairs are critical to enhance the fuel molecular conversion. Although our present investigation is still insufficient to identify the exact role of the of carbon supports on the formation of Pt nanoparticles and their electrochemical performance for ORR, the work may generate some fundamental insights into the understanding of electrocatalyst architectures for fuel cell electrodes.

4.3.4 Carbon Corrosion Test

As can be seen from Figure 4.7, the performance of MEA with commercial Pt/XC72 decreased a lot after 45 hours corrosion test. The current density decreasing rate at 0.8 V, 0.7 V and 0.6 V reaches 2.2 $mA/cm^2/h$, 7 $mA/cm^2/h$ and 16 $mA/cm^2/h$. Compared with the commercial catalyst, the performance of MEA with home-made Pt/XC721000-1h did not decrease much less than commercial catalyst in Figure 4.8. From 0h to 40h, the performance of MEA with home-made Pt/XC721000-1h stayed all most the same. The current density decreasing rate at 0.8 V, 0.7 V and 0.6 V reaches 0.9 $mA/cm^2/h$, 2.8 $mA/cm^2/h$ and 2.7 $mA/cm^2/h$. It could be concluded that the Pt/XC721000-1h has a much higher carbon corrosion resistance than commercial catalyst.

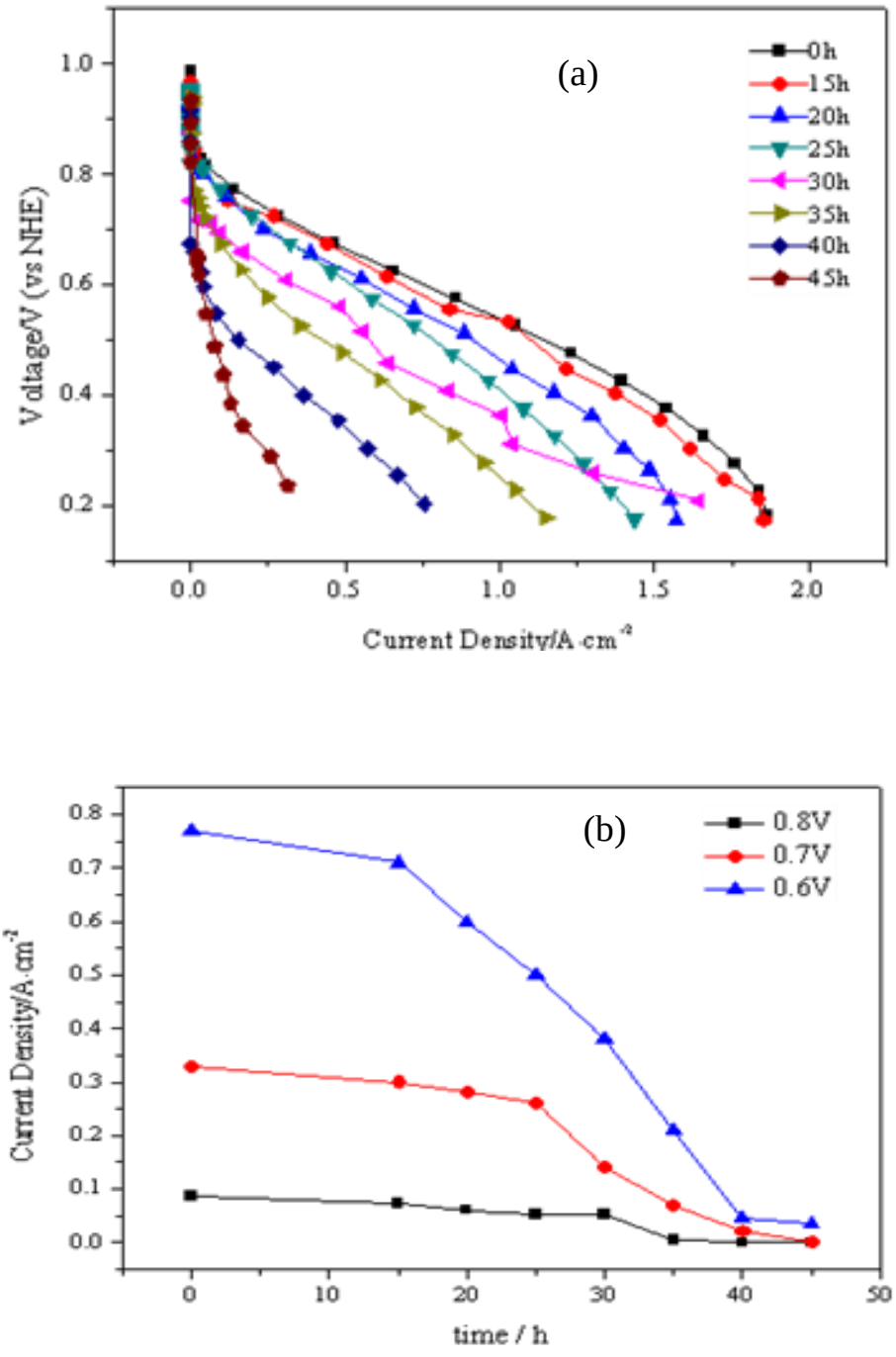

Figure 4.7 (a) Polarization curves of the MEA with commercial Pt/XC72 in different corrosion time; (b) Current density at 0.8, 0.7 and 0.6 V change at different corrosion time

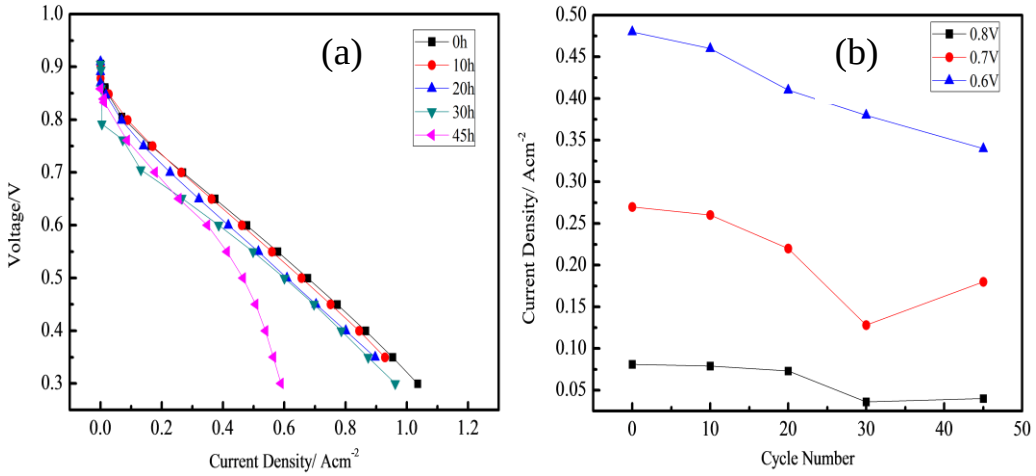

Figure 4.8 (a) Polarization curves of the MEA with home-made Pt/XC72-1000-1h in different corrosion time; (b) Current density at 0.8, 0.7 and 0.6 V change at different corrosion time

4.4 Conclusion

XC72 carbon blacks were steam etched under different conditions and used as catalyst support for oxygen reduction reactions. The XC72 structure changes with the increase of the etching time were clearly observed. The 002 and 10 peaks of the etched samples first became sharper and then became broad again during steam etching, which corresponds with the idea that the defects and the amorphous phase are corroded away from the carbon blacks, and then the micro-crystallites are further corroded. Pt nano-particles have better dispersion on the steam etched samples and as the increase of etching time the Pt particles size decreased. For the sample with better crystallite structure have better ORR. The ORR and ECSA for the catalysts supported on the steam etched XC72 samples are much better than that of the non-etching samples and the commercial catalysts. The MEA corrosion test showed the home made Pt/XC721000-1h has a much higher corrosion resistance than commercial Pt/XC72. Steam etching is a simple and efficient method to increase the performance and durability of the fuel cells catalysts.

5. CONCLUSIONS AND FUTURE WORK

5.1 Conclusions

Fuel cells are an alternative energy source to traditional energy sources. They create energy through the electrochemical reaction between hydrogen and oxygen, leaving water as a byproduct. The three different researches described above are part of manufacture of best MEA.

In the first study, micro-structural organization of ionomer particles and Pt/C aggregates dispersed in liquid media was studied by USAXS and Cryo-TEM technologies in order to fill the gap of the detail particle dispersion information in catalyst ink, which was employed to make MEA. The USAXS and TEM image shows that the 28% catalyst ink, which gives the best PEFC performance, was composed by Nafion® ionomer with rod-like particles (d = 3 nm, L = 20 nm), single sphere carbon black particle (d = 30 ~ 70 nm), and rod-like aggregated carbon black particles (d = 30 ~ 70 nm, L = 150 nm) and some much bigger aggregated particles (R > 200 nm).

In the second study, the corrosion of XC72 and BP2000 as catalyst carbon supports was studied by an accelerated durability test utilizing an RDE system. This innovated RDE ADT approach would be employed to investigate the carbon support corrosion process without The observed corrosion processes for Pt/XC72 started from the center of the particle because there is more graphitization structure on the surface and more disorder structure in the center, as for Pt/BP2000, the corrosion started on the surface of the particle because of its high surface area and more ordered carbon layer plane structure. The steam etching experiment confirmed the corrosion process observed in the RDE testing for both catalysts.

Based on the second research, a new approach to make a high corrosion resistance catalyst was suggested, using steam etching method to make XC72 carbon blacks under different etching times. The XC72 structure changes with the increase of the etching time were clearly observed. Amorphous phase are corroded away from the carbon blacks after 1 hour steam etching, and then, after 3 hours, the micro-crystallites are further corroded. Pt particle size was greatly affected by the structure of carbon support. It was obtained that the optimal Pt size and carbon crystallite structure are obtained after 1 hour steam etching. Pt/XC721000-1h has the best performance. The MEA corrosion test showed the home-made Pt/XC721000-1h has a much higher corrosion resistance than commercial Pt/XC72. Steam etching is a simple and efficient method to increase the performance and durability of the fuel cells catalysts.

5.2 Recommendations for Future Research

Further work could be done to expand upon the research covered in this thesis as described as follows:

1) Interaction of carbon and Nafion ionomer: the interaction of carbon and Nafion® ionomer should be investigated further. The key point of this research would be how to see the Nafion® ionomer in the catalyst ink. I have developed an approach to make Ce^{3+} form Nafion®. The cryo TEM would be employed to investigate the geometry of Ce^{3+} form Nafion® ionomer.

2) Carbon support corrosion process: corrosion process of carbon support should be further investigated using MEA configuration

3) High corrosion resistance catalyst development: functional Carbon Black has a higher corrosion resistance than that of carbon black. The corrosion process of FCB should be further investigated by RDE and MEA single cell.

LIST OF REFERENCES

LIST OF REFERENCES

[1] X. Z. Yuan and H. Wang, *Proton Exchange Membrane fuel cell electrocatalysts and catalyst layers: fundamentals and applications*, Springer: Verlag London lstd, pp. 103 - 145, 2008.

[2] B. C. H. Steele and A. Heinzel, "Materials for proton exchange membrane fuel cell technologies," *Nature*, pp. 345 - 352, 2001.

[3] Z. Chen, M. Wa, W. Li and Y. Yan, "Supportless Pt and PtPd Nanotubes as Electrocatalysts for Oxygen-Reduction Reactions," *Angewandte Chemie International Edition*, pp. 4060 - 4063, 2007.

[4] S. M. Haile and D. Boysen, "Solid acids as fuel cell electrolytes" *Nature*, pp. 910 - 913, 2001.

[5] M. Z. Jacobson, W. Colella and D. G. Golden, "Cleaning the air and improving health with hydrogen proton exchange membrane fuel-cell vehicles," *Science*, pp. 1901 - 1903, 2005.

[6] H. Ohtsuka and J. Yamaki, "A Solid Sulfur Cathode for Aqueous Batteries," *Solid State Ionics*, pp. 3 - 9, 1989.

[7] E. J. Taylor, E. B. Anderson and N. R. K. Vilambi, "Preparation of highplatinum-utilization gas diffusion electrodes for proton-exchange membrane fuel cells," *The Journal of Electrochem Society*, pp. 145 - 156, 1992.

[8] S. Hirano, J. Kim and S. Srinivasan, "High performance of Proton Exchange Membrane Fuel Cells (PEMFCs) with sputter-deposited Platium layer electrodes under harsh simulated fuel cell conditions," *Electrochemical Acta*, pp. 1587 - 1593, 1997.

[9] K. Amine, K. Yasuda and H. Takenaka, "New process for loading highly active platinum on carbon black surface for application in polymer electrolyte fuel cell," *Annales De Chimie-Science Des Materiaux*, pp. 331 - 335, 1998.

[10] M. Wilson and S. Gottesfeld, "High Performance Direct Methanol Polymer Electrolyte Fuel Cell," *The Journal of Electrochemical Society*, pp. 128 - 131, 1992.

[11] M. Wilson and S. Gottesfeld, "High Performance Direct Methanol Polymer Electrolyte Fuel Cell," *The Journal of Applied Electrochemistry*, pp. 22 - 30, 1992.

[12] J. J. Zhang, *PEM fuel cell electrocatalysts and catalyst layers: fundamentals and applications*, Springer: Verlag London lstd, pp. 163 - 165, 2008.

[13] J. J. Zhang, *PEM fuel cell electrocatalysts and catalyst layers: fundamentals and applications*, Springer: Verlag London lstd, pp. 374 - 375, 2008.

[14] M. Chisaka and H. Dai, "National heat transfer symposium of Japan," *44th National heat transfer symposium of Japan*, pp. 44 - 49, 2007.

[15] B. Peng, D. Johannsmann and J. Rühe, "Homogeneously aligned liquid crystal polymer brushes," *Macromolecules*, pp. 6759 - 6766, 1999.

[16] S. Jiang, K. Q. Xia and G. Xu, "Effect of Additives on Self-Assembling Behavior of Nafion in Aqueous Media," *Macromolecules*, pp. 7783 - 7787, 2001.

[17] E. Szajdzinska Pietek, S. Schlick and A. Plonka, "Self-Assembling of Perfluorinated Polymeric Surfactants," *Langmuir*, pp. 2188 - 2193, 1994.

[18] P. Aldebert, B. Dreyfus and M. Pineri, "Self-assembling of ion-containing polymers," *Macromolecules*, pp. 2651 - 2659, 1986.

[19] H. Li and S. Schlick, "Effect of solvents on phase separation in spin resonance of VO^{2+} in swollen membranes and solutions," *Polymer*, pp. 1141 - 1148, 1995.

[20] G. Gebel, "Mechanical endurance of polymer electrolyte membrane and PEM fuel cell durability," *Polymer*, pp. 5829 - 5837, 2000.

[21] B. Loppinet, G. Gebel and C. E. Williams, "Small-angle scattering study of perfluorosulfonated ionomer solutions," *The Journal of Physical Chemistry B*, pp. 1884 - 1892, 1997.

[22] R. Borup, J. Meyers and B. Pivovar, "Scientific Aspects of Polymer Electrolyte Fuel Cell Durability and Degradation," *Chemical Rev*iews, pp. 3904 - 3951, 2007 .

[23] B. Wahdame, D. Candusso, X. Francois, F. Harel, M. C. Pera, D. Hissel and J. M. Kaufmann, "Comparison between two PEM fuel cell durability tests," *The Journal of Hydrogen Energy*, pp. 5493 - 5499, 2007.

[24] F. A. De Bruijn, V. A. T. Dam and G. J. M. Janssen, "Durability and degradation issues of PEM fuel cell components," *Fuel cell*, pp. 3 - 17, 2008.

[25] J. Xie, D. Wood, D. Wayne, T. Zawodzinski, P. Atanassov and R. Borup, "Durability of PEFCs at High Humidity Conditions," *The Journal of Electrochemical Society*, pp. 47 - 52, 2005.

[26] J. Xie, D. Wood, K. More, P. Atanassov and R. Borup, "Micro-Structural Changes of Membrane Electrode Assembly During PEFC Durability Testing at High Humidity Conditions," *The Journal of Electrochemical Society*, pp. 1011 - 1019, 2005.

[27] K. Miyatake, H. Zhou, T. Matsuo, H. Uchida and M. Watanabe, "Proton Conductive Polyimide Electrolytes Containing Trifluoromethyl Groups," *Macromolecules*, pp. 4961 - 4967, 2004.

[28] J. Maekawa, Z. Siroma, K. Tanaka, M. Kohyama and K. Yasuda, "Analytical TEM study of Pt particle deposition in the proton-exchange membrane of a membrane-electrode-assembly," *The Journal of Power Sources*, pp. 461 - 468, 2006.

[29] M. Fowler, R. F. Mann, C. Amphlett, B. A. Peppley and P. R. Roberge, "Handbook of fuel cells, fundamentals, technology and applications," *Springer*, pp. 398 - 399, 2003.

[30] R. M. Darling and J. P. Meyers, "Kinetic Model of Platinum Dissolution in PEMFCs," *The Journal of Electrochemical Society*, pp. 1523 - 1529, 2003.

[31] P. J. Ferreira, Y. Shaohorn, D. Morgan, R. Makharia, S. Kocha and A. Gasteiger, "Pt/C Electrocatalysts in Proton Exchange Membrane Fuel Cells: A Mechanistic Investigation," *The Journal of Electrochemical Society*, pp. 2256 - 2262, 2005.

[32] J. Xie, D. Wood, K. More, P. Atanassov and R. Borup, "Micro-Structural Changes of Membrane Electrode Assembly During PEFC Durability Testing at High Humidity Conditions," *The Journal of Electrochemical Society*, pp. 1011 - 1019, 2005.

[33] R. Borup, L. J. R. Davey, F. H. Garzon, D. L. Wood and M. A. Inbody, "PEM fuel cell electrocatalyst durability measurements," *The Journal of Power Sources*, pp. 76-97, 2006.

[34] M. Cai, M. S.Ruthkosky, B. Merzougui, S. Swathirajan and M. P. Balogh, "Investigation of thermal and electrochemical degradation of fuel cell catalysts," *The Journal of Power Sources*, pp. 977 - 1002, 2006.

[35] Z. Siroma, K. Ishii, K. Yasuda, Y. Miyazaki, M. Inaba and A. Tasaka, "Sub-Stoichiometric Titanium Oxides as Platinum Support for PEM Fuel Cells," *Electrochemiscal Communication*, pp. 1153 - 1162, 2005.

[36] S. J. C. Cleghorn, D. K. Mayfield, D. A. Moore, G. Rusch, T. W. Sherman, N. T. Sisofo, and U. Beuscher, "A polymer electrolyte fuel cell life test," *The Journal of Power Sources*, pp. 446 - 452, 2006.

[37] J. St-pierre, D. P. Wilkinson, S. D. Knights, M. Bos and J. N. Mater, "Relationships between Water Management, Contamination and Lifetime Degradation in PEFC, "*The Journal of New Matterial Electrochemiscal Systems*, pp. 99-106, 2000.

[38] D. Liu and S. Case, "Durability study of proton exchange membrane fuel cells under dynamic testing conditions with cyclic current profile," *The Journal of Power Sources*, pp. 521 - 531, 2006.

[39] M. Dowlapalli, J. P. Atanassov and G. Rice, "Electrochemical Oxidation Resistance of Carbonaceous Materials," *ECS Transactions*, pp. 41 - 48, 2006.

[40] K. H. Kangasniemi, D. A. Condit, and T. D. Jarvi, "Characterization of Vulcan electrochemically oxidized under simulated PEM fuel cell," *The Journal of Electrochemical Society*, pp. 125 - 137, 2004.

[41] M. F. Mathias, R. Makharia, H. A. Gasteiger, J. J. Conley, T. J. Fuller, C. J. Gittleman, S. S. Kocha, D. P. Miller, C. K. Mittelsteadt, T. Xie, S. G. Yan, and P. T. Yu, "Fuel Cell Review," *The Journal of Electrochemical Society Interface*, pp. 24 - 36, 2005.

[42] J. P. Meyers and R. M. Darling, "Model of carbon corrosion in PEM fuel cells," *The Journal of Electrochemical Society*, pp. 1432 - 1438, 2006.

[43] H. Tang, Z. Qi, M. Ramani and J. F. Elter, "PEM fuel cell cathode carbon corrosion due to the formation of air/fuel boundary at the anode," *The Journal of Power Sources*, pp. 1306 - 1312, 2006.

[44] Carl. A. Reiser and D. Jarvi, "A reversecurrent decay mechanism for fuel cells," *Electrochem Solid State Letters*, pp. 273 - 281, 2005.

[45] S. Yoshioka, A. Yoshimura, H. Fukumoto, O. Hiroi and H. Yoshiyasu, "Development of a PEFC under low humidified conditions," *The Journal of Power Sources*, pp. 146 - 153, 2005.

[46] J. Zhang, J. Owejan, M. Fay, B. A. Litteer, P. T. Yu, W. Gu and H. A. Gasteiger, "Oxygenate Activity," *American Chemical Society*, pp. 388 - 395, 2007.

[47] L. M. Roen, C. H. Paik, T. D. Jarvi, "Electrocatalytic corrosion of carbon support in PEMFC cathodes," *Electrochemica Solid State Letter*, pp. 19 - 23, 2004.

[48] J. Wang, G. Yin, Y. Shao, S. Zhang, Z. Wang and Y. Gao, "Effect of carbon support for oxygen reduction reaction," *The Journal of Power Sources*, pp. 331 - 338, 2007.

[49] A. S. Arico, A. Stassi, E. Modica, R. Ornelas and I. Gatto, "Investigation of high temperature polymer electrolyte fuel cell catalysts," *The Journal of Power Sources*, pp. 525 - 532, 2008.

[50] Y. Shao, G. Yin, Y. Gao and P. Shi, "Durability Study of Pt/C and Pt/CNTs Catalysts under PEM Fuel Cell Conditions," *The Journal of Electrochemical Society*, pp. 1093 - 1098, 2006.

[51] W. Bi and T. F. Fuller, "Temperature Effects on PEM Fuel Cells Pt/C Catalyst Degradation," *The Journal of Electrochemical Society*, pp. 215 - 221, 2008.

[52] E. L. Thompson, T. W. Capehart, T. J. Fuller, and J. Jorne, "Investigation of Low-Temperature Catalyst Layer: Carbon Corrosion," *The Journal of Electrochemical Society*, pp. 913 - 921, 2009.

[53] M. F. Mathias, "Outstanding Achievement in R&D of PEMFC Durability," *ECS Interface*, pp. 24 - 32, 2005.

[54] H. Chizawa, "Study of accelerated test protocol for PEFC focusing on carbon corrosion," *ECS Transactions*, pp. 645 - 651, 2006.

[55] Y. Z. Fan, H. Q. Hu and H. Liu, "Enhanced coulombic efficiency and power density of air- H_2 cell configuration," *The Journal of Power Sources*, pp. 18 - 24, 2007.

[56] J. Li, P. He, K. Wang and M. David, "Characterization of catalyst layer structural changes in PEMFC as a function of durability testing," *ECS transactions*, pp. 31743 - 31749, 2006.

[57] J. K. Hyun, Z. Y. Liu and D. A. Muller, "3D Three-Dimensional Imaging of Corrosion Mechanisms in Polymer Electrolyte Fuel Cells by Scanning Transmission Electron Tomography," *Microsc microanal*, pp. 15 - 21, 2009.

[58] J. Xie, D. Wood, K. More, P. Atanassov and R. Borup, "Micro-Structural Changes of Membrane Electrode Assembly During PEFC Durability Testing at High Humidity Conditions," *The Journal of Electrochemical Society*, pp. 1011 - 1019, 2005.

[59] J. Xie, K. More, T. Zawodzinski and W. Smith, "Porosimetry of MEAs Made by "Thin Film Decal" Method and Its Effect on Performance of PEFCs," *The Journal of Electrochemical Society*, pp. 1841 - 1852, 2004.

[60] Y. Shi, A. Horky, O. Polevaya and J. Cross, *Fuel Cell review report in courtesy associates*, Palm Springs, 2005.

[61] H. R. Colonmercado, H. Kim and B. N. Popov, "Electrochemical Intercalation of Lithium into cathode in PEMFC," *Electrochemical Communication*, pp. 795 - 799, 2004.

[62] A. Kabbabi, F. Gloaguen and F. Andoofatto, "Particle size effect for oxygen reduction and methanol oxidation on Pt/C inside a proton exchange membrane," *The Journal of Electroanalysis Chemistry*, pp. 251 - 259, 1994.

[63] A. Gamez, D. Richard, P. Gallezot, F. Gloaguen, R. Faure and R. Durand, "Oxygen reduction on well-defined platinum nanoparticles inside recast ionomer," *Electrochimical Acta*, pp. 307 - 317, 1996.

[64] F. M. Maillard, F. Gloaguen and J. M. Leger, "Analysis of performance losses of direct ethanol fuel cells with the aid of a reference electrode," *Electrochimical Acta*, pp. 3431 - 3439, 2002.

[65] L. Q. Wang, L. F. Jiao and H. T. Yuan, "Corrosion test in Fuel cell system by Pt/XC72," *The Journal of Power Sources*, pp. 151 - 162, 2006.

[66] A. V. Tripkovic, K. D. Popovic, B. N. Grgur, B. Blizanac, P. N. Ross and N. M. Markovic, "Methanol electrooxidation on supported Pt and PtRu catalysts in acid and alkaline solutions," *Electrochimical Acta*, pp. 3707 - 3714, 2002.

[67] T. J. Gasteiger and H. A. Behm, "Rotating disk electrode measurements on the CO tolerance of a high-surface area Pt/Vulcan carbon fuel cell catalyst," *The Journal of Electrochemical Society*, pp. 1296 - 1302, 1999.

[68] U. A. Paulus, T. J. Schmidt, and H. A. Gasteiger, "Oxygen reduction on a high-surface area Pt/Vulcan carbon catalyst: a thin-film rotating ring-disk electrode study," *The Journal of Electroanalysis Chemistry*, pp. 134 - 136, 2001.

[69] J. J. Zhang, *PEM fuel cell electrocatalysts and catalyst layers: fundamentals and applications*, Springer: Verlag London lstd, pp. 433 - 435, 2008.

[70] M. Inaba, "Corrosion Report" *210th ECS meeting in Cancun, Mexico*, 2006.

[71] K. Kinoshita, *Carbon: electrochemical and physiochemical properties*, John Wiley & Sons: New York, pp. 876 - 877, 1998.

[72] X. Wang, R. Kumar, and D. Myers, "Effect of Voltage on Platinum Dissolution Relevance to Polymer Electrolyte Fuel Cells," *The Journal of Electrochemical and Solid State Letters*, pp. 225 - 231, 2006.

[73] M. Watanabe, K. Tsurumi, T. Mizukami, T. Nakamura and P. Stonehart, "Activity and Stability of Ordered and Disordered Co-Pt Alloys for Phosphoric Acid Fuel Cell," *The Journal of Electrochemical Society*, pp. 2659 - 2664, 1994.

[74] J. A. Bett, K. Kinoshita and P. Stonehart, "Crystallite growth of platinum dispersed on graphitized carbon black," *The Journal of Catalysis*, pp. 307 - 311, 1974.

[75] H. R. Colon-mercado and B. N. Popov, "Stability of platinum based alloy cathode catalysts in PEM fuel cells," *The Journal of Power Sources*, pp. 253 - 260, 2006.

[76] P. F. Aparicio and M. A. folyado, "Investigation of Fuel Cell cathode catalyst degradation" *The Journal of Power Sources*, pp. 57 - 64, 2009.

[77] D. Strmcnik, N. Hodnik and S. B. Hocevar, "Novel Method for Fast Characterization of High-Surface-Area Electrocatalytic Materials Using a Carbon Fiber Microelectrode," *The Journal of Physical Chemistry C*, pp. 2640 - 2648, 2010.

[78] S. Z. Yang, G. L. Zhao and E. Khosravi, "First Principles Studies of Nitrogen Doped Carbon Nanotubes for Dioxygen Reduction," *The Journal of Physical Chemistry C*, pp. 3371 - 3379, 2010.

[79] R. V. Shanahan, L. Xu, C. Liang, M. Waje, S. Dai and S. Y. Yan, "Graphitic mesoporous carbon as a durable fuel cell catalyst support," *The Journal of Power Sources*, pp. 423 - 426, 2008.

[80] C. Xu, X. Wang and J. Zhu, "Graphene Metal Particle Nanocomp," *The Journal of Physical Chemistry C*, pp. 19841 - 19849, 2008.

[81] D. Ugarte, "Curling and closure of graphitic networks under electron-beam irradiation," *Nature*, pp. 707 - 712, 1992.

[82] K. Agaki, R. Tamura, M. Tsukada and S. Itoh, "Electronic Structure of Helically Coiled Cage of Graphitic Carbon," *Physical Review Letters*, pp. 2307 - 2313, 1995.

[83] K. Sattler, "Scanning Tunneling Microscopy of Carbon Nanotubes and Nanocones," *Carbon*, pp. 915 - 923, 1995.

[84] P. Ajayan, J. Nugent, R. Siegel, B. Wei and P. H. Kohler Redlich, "Growth of carbon microtrees," *Nature*, pp. 243 - 253, 2000.

[85] T. Astakhova, G. Vinogradov and E. Osawa, “Numerical generation of nanotube caps II,” *Materials Science and Technology*, pp. 769 - 773, 1999.

[86] Y. Gogotsi, J. Libera, N. Kalashnikov and M. Yoshimura, “Graphite Polyhedral Crystals,” *Science*, pp. 317 - 321, 2000.

[87] Z. Q. Jiang, X. Y. Yu, Z. J. Jiang, Y. D. Meng and Y. C. Shi, “Synthesis of monodispersed Pt nanoparticles on plasma processed carbon nanotubes for methanol electro-oxidation reaction,” *Journal of Materials Chemistry*, pp. 6720 - 6726, 2009.

[88] Z. P. Shan, X. G. Zhang, X. Y. Lin and H. L. Lin, “A facile approach towards sulfonate functionalization of multi-walled carbon nanotubes as Pd catalyst support for ethylene glycol electro-oxidation,” *The Journal of Power Sources*, pp. 366 - 346, 2009.

[89] R. V. Hull, L. Li, Y. Xing and C. Chu, “Sonochemical oxidation of multiwalled carbon nanotubes,” *Langmuir*, pp. 4185 - 4192, 2005.

[90] C. D. Hong, Z. T. Xiang, J. Y. Lin and K. L. Tang, “Study of Pt/Graphene in PEFC,” *Surface Review and Letters*, pp. 1443 - 1451, 2002.

[91] P. Gallezot, D. Richard and G. Bergert, “Heat-treated carbon-blacks as supports for platinum catalysts,” *Journal of Catalysis*, pp. 299 - 302, 1995.

[92] S. Zhang, Y. Shao, X. Li, Z. Nie, Y. Wang and Y. Lin, “Low-Cost and Durable Catalyst Support for Fuel Cells: Graphite Submicronparticles,” *The Journal of Power Sources*, pp. 457 - 464, 2010.

[93] R. B. Peter, E. Emmanuel and R. O. John, “Investigation of platinum utilization and morphology in catalyst layer of polymer electrolyte fuel cells,” *The Journal of Power Sources*, pp. 75 - 82, 1999.